Spring 2015

Surface modification of traditional and bioresorbable metallic implant materials for improved biocompatibility

Emily Kristine Walker
Purdue University

Recommended Citation

Walker, Emily Kristine, "Surface modification of traditional and bioresorbable metallic implant materials for improved biocompatibility" (2015). *Open Access Dissertations*. 582.
https://docs.lib.purdue.edu/open_access_dissertations/582

Graduate School Form 30
(Revised 08/14)

PURDUE UNIVERSITY
GRADUATE SCHOOL
Thesis/Dissertation Acceptance

This is to certify that the thesis/dissertation prepared

By Emily Kristine Walker

Entitled
SURFACE MODIFICATION OF TRADITIONAL AND BIORESORBABLE METALLIC IMPLANT MATERIALS FOR IMPROVED BIOCOMPATIBILITY

For the degree of Doctor of Philosophy

Is approved by the final examining committee:

Lia Stanciu

Jean Paul Allain

Eric Nauman

Jeffrey Youngblood

To the best of my knowledge and as understood by the student in the Thesis/Dissertation Agreement, Publication Delay, and Certification/Disclaimer (Graduate School Form 32), this thesis/dissertation adheres to the provisions of Purdue University's "Policy on Integrity in Research" and the use of copyrighted material.

Approved by Major Professor(s): Lia Stanciu

Approved by: David Bahr 04/08/2015

Head of the Department Graduate Program Date

SURFACE MODIFICATION OF TRADITIONAL AND BIORESORBABLE METALLIC IMPLANT MATERIALS FOR IMPROVED BIOCOMPATIBILITY

A Dissertation
Submitted to the Faculty
of
Purdue University
by
Emily K. Walker

In Partial Fulfillment of the
Requirements for the Degree
of
Doctor of Philosophy

May 2015
Purdue University
West Lafayette, Ind

For my sister, Karen Kosowski.

ACKNOWLEDGMENTS

Funding for the research described in this dissertation was provided by the U.S. Army Medical Research and Materiel Command grant number DM090909 (W81XWH-11-2-0067) and by Fort Wayne Metals. I am also grateful for support provided by the Purdue Summer Undergraduate Research Fellowship (SURF) Program and Los Alamos National Laboratory.

I am grateful to the advisors and mentors who have guided me through graduate research: Jean Paul Allain, Lia Stanciu, and Eric Nauman. Thank you to Lisa Dougherty, Dan Kathios, and Doug Kautz at Los Alamos for providing support throughout my dissertation writing process and helping me transition into work at the Laboratory, and thank you to Ben Morrow for invaluable advice on etching. I would also like to sincerely thank my undergraduate advisor, Richard Lepkowicz, for preparing me for graduate research.

I am also grateful to Professor Eric Kvam for teaching me everything about nothing, and Professor Mysore Dayananda for teaching me so much about microstructural characterization.

I must thank all the other graduate students who helped me in and out of the lab. Julia Alspaugh, Brandon Holybee, Eric Yang, Sergey Suslov, Anastassia Suslova, Alexandra Snyder, Lisa Reece, and Dan Rokusek, thank you for always being willing to help and provide advice. Kevin Chaput, thank you for your expertise and assistance with casting. Thank you to Jeremy Schaffer of Fort Wayne Metals for materials and advice. Michael Heiden, thank you for always being enthusiastic about Team Iron Manganese and keeping the project moving forward. I know the project is in good hands with you.

Thank you to the undergraduates who assisted me with my experiments: Emily Gordon, Elgin Leow, and Joshua McCarley.

And last but certainly not least, thank you to my family for always being proud of me and having faith in me.

TABLE OF CONTENTS

Page

LIST OF TABLES

Table Page

Table Page

LIST OF FIGURES

Figure Page

Figure Page

Figure Page

NOMENCLATURE

α-hematite	α–Fe_2O_3, iron(III) oxide
β-TG	beta thromboglobulin
316L	surgical stainless steel, comprised of 16-18.5% Cr, 10-14% Ni, 2-3% Mo, <2% Mn, <1% Si, <0.045% P, <0.03% S, and <0.03% C, balance Fe
AFM	atomic force microscopy
AMS	absorbable metal stent
Bcc	body-centered cubic crystal structure
BMS	bare metal stent
BX	balloon expandable stent
CW	cold-work
DES	drug-eluting stent
DFT	drawn-filled-tube
EDS	energy dispersive x-ray spectroscopy
ELISA	enzyme-linked immunosorbent assay
FDA	United States Food & Drug Administration
Fe35Mn	alloy of iron -35 wt. % manganese
Fe30Mn	alloy of iron -30 wt% manganese

Fe20Mn	alloy of iron -20 wt% manganese
GPa	gigapascal (10^9 N/m^2)
Hcp	hexagonal close-packed crystal structure
IBS	ion beam sputtering
ISR	in-stent restenosis
IVUS	intravascular ultrasound
LST	late stent thrombosis
Magnetite	Fe_3O_4 or $FeO.Fe_2O_3$, iron (II,III) oxide
mmpy	millimeters per year (unit of corrosion rate)
MPa	megapascal (10^6 N/m^2)
MRI	magnetic resonance imaging
NiTi	nickel-titanium shape memory alloy (Nitinol)
OEF	Operation Enduring Freedom, US War in Afghanistan, 2001-present
OIF	Operation Iraqi Freedom, US War in Iraq, 2003-2011
PBI	penetrating brain injury
PBS	phosphate-buffered saline
pH	(p[H]) negative logarithm of the hydronium ion activity compared to hydroxide activity
PLLA	poly-L lactic acid
PMN	polymorphonuclear elastase
PTCA	percutaneous transluminal coronary angioplasty
SCC	stress corrosion cracking

SEM	scanning electron microscopy
SRIM	Stopping Range of Ions in Matter software
SX	self-expanding stent
TAT	thrombin-antithrombin complex
TEM	transmission electron microscopy
Ti6Al4V	medical grade titanium alloy comprised of 6 wt. % aluminum and 4 wt. % vanadium, balance titanium
UTS	ultimate tensile strength (MPa)
Wüstite	FeO, iron(II) oxide
XPS	x-ray photoelectron spectroscopy
XRD	x-ray diffraction
ZM21	alloy comprised of 2 wt. % zinc, 1 wt. % manganese, balance magnesium

ABSTRACT

Walker, Emily K., Ph.D., Purdue University, May 2015. Surface Modification of Traditional and Bioresorbable Metallic Implant Materials for Improved Biocompatibility. Major Professor: Lia A. Stanciu.

Due to their strength, elasticity, and durability, a variety of metal alloys are commonly used in medical implants. Traditionally, corrosion-resistant metals have been preferred. These permanent materials can cause negative systemic and local tissue effects in the long-term. Permanent stenting can lead to late-stent thrombosis and in-stent restenosis. Metallic pins and screws for fracture fixation can corrode and fail, cause loss of bone mass, and contribute to inflammation and pain at the implant site, requiring reintervention. Corrodible metallic implants have the potential to prevent many of these complications by providing transient support to the affected tissue, dissolving at a rate congruent with the healing of the tissue. Alloys of iron and manganese (FeMn) exhibit similar fatigue strength, toughness, and elasticity compared with 316L stainless steel, making them very attractive candidates for bioresorbable stents and temporary fracture fixation devices. Much attention in recent years has been given to creating alloys with ideal mechanical properties for various applications. Little work has been done on determining the

blood compatibility of these materials or on examining how their surfaces can be improved to improve cell adhesion, however. We examined thethrombogenic response of blood exposed to various resorbable ferrous stent materials through contact with porcine blood. The resorbable materials induced comparable or lower levels of several coagulation factors compared with 316L stainless steel. Little platelet adhesion was observed on any of the tested materials.

Endothelialization is an important process after the implantation of a vascular stent, as it prevents damage to the vessel wall that can accelerate neointimal hyperplasia. Micromotion can lead to the formation of fibrous tissue surrounding an orthopedic implant, loosening, and ultimately failure of the implant. Nanoscale features were created on the surfaces of noble metal coatings, silicon, and bioabsorbable materials through ion beam irradiation in order to improve endothelialzation and bone cell adhesion. Gold, palladium, silicon, and iron manganese surfaces were patterned through ion beam irradiation using argon ions. The surface morphology of the samples was examined using atomic force microscopy (AFM) and scanning electron microscopy (SEM), while surface chemistry was examined through x-ray photoelectron spectroscopy (XPS) and contact angle goniometry measurements. It was not possible to create nanoscale surface features on the surfaces of the gold and palladium films. At near normal incidence, irradiation produced ripples on the surfaces of Si(100), while oblique incidence irradiation produced nanoislands in the presence of impurities on the surface. Iron manganese irradiation resulted in the formation of blade-shaped structures for ion energies between 500eV and 1000eV, and significant iron enrichment at the surface.

Chemical treatment can also be used to create surface features that will enhance cell adhesion. Ti6Al4V is one of the most commonly used alloys for permanent orthopedic devices. The creation of a porous surface in order to improve osteoblast adhesion was achieved through chemical etching using acid-peroxide solutions. While phosphoric acid etched the grain boundaries, sulfuric and nitric acid preferentially etched grains of particular orientations, creating a spongy, porous morphology that has the potential to aid in osseointegration.

CHAPTER 1 INTRODUCTION

1.1 An Overview of Biomaterials

A biomaterial is any material used to replace a tissue or function *in vivo* [1]. A biomaterial must be mechanically reliable, non-inflammatory, non-toxic, and non-carcinogenic. Traditionally, biomaterials have also been required to be inert in the physiological environment. Metals have been used as biomaterials for centuries, but their efficacy was limited prior to the adoption of aseptic surgical technique, due to the prevalence of infection [2]. While corrosion resistant metals such as gold, silver, and platinum were used with some success, early steels corroded rapidly in vivo and caused inflammation [2]. Noble metals are not suitable for most load-bearing applications due to their relatively low strengths and high malleability, as well as their considerable expense. Noble metals are therefore generally only seen today in dental applications such as fillings, or for flexible non-load-bearing applications, such as platinum coils for cerebral aneurysm occlusion.

Today, biomaterials can be divided into three main classes. First generation biomaterials, which were used heavily in the 1950s and 1960s, took advantage of existing engineering alloys [1]. These materials were meant to be bioinert and were borrowed from the aerospace and construction industries; the materials used were not designed purposely for use in biomedical implants. By the 1980s, between 2 and 3 million prostheses had been implanted into Americans, made from about 40 different materials [3].

Second generation biomaterials, on the other hand, were designed to induce a particular tissue reaction and were introduced in the 1980s [1, 3]. These include bioactive glasses, biodegradable materials, and many other "active" materials [1]. Bioactive glasses are designed to create a strong bond with the surrounding bone tissue and induce osteoblast proliferation, thus preventing implant loosening, which is a persistent problem in many orthopedic applications [4]. Finally, third generation biomaterials have been introduced in order to stimulate and accelerate healing in damaged tissues by influencing cell behavior at the molecular level [1, 3, 5]. These materials include, but are not limited to, nanostructured surfaces to influence cell differentiation in certain tissues, porous foams, and polymers that release ions and growth factors [3]. These three classes of biomaterials should be considered conceptual generations, rather than chronological. The development of first and second generation biomaterials continues to this day, as 3rd generation biomaterials are not intended to entirely replace them, but to provide treatments otherwise impossible with first and second generation biomaterials [5].

For a biomaterial to be considered viable, it must elicit "appropriate host responses" such as resistance to bacteria, resistance to abnormal blood clot formation, and normal tissue healing [1]. This biocompatibility must extend to the entire lifetime of the device; some devices have temporary contact with the biological environment, such as a dialysis membrane or a urinary catheter, while others are permanent and must function appropriately for the remainder of the patient's life, such as a joint replacement or a heart valve. As life expectancies increase, the viable lifetime of these permanent devices must increase with them. Biocompatibility originally referred only to the material serving its function in the body without causing damage to the surrounding tissue, but as 3rd generation biomaterials emerge, biocompatibility must now encompass specific interactions between the biomaterial and its host tissue [6].

1.2 Applications of Metallic Biomaterials

While a large variety of materials is used in medical devices, metals provide the greatest mechanical strength and are preferred for structural applications. They also have excellent thermal and electrical conductivity. Metals are most commonly used in orthopedic and dental implants, but also have important applications for cardiovascular devices [1].

The following section describes the state of the art in metallic vascular implants and describes some of the issues associated with current designs. This section is followed by a section describing metallic orthopedic implants used in traditional load-bearing applications.

1.2.1 Vascular Implants

Due to the frequency of vessel recoil following percutaneous transluminal coronary angioplasty (PTCA), it has become common practice for the surgeon to insert a stent in order to maintain vessel patency following the procedure. The stents currently used in clinical applications are composed of corrosion-resistant metals, with a few polymers used for specific applications [7].

Bare metal stents (BMS) traditionally remain in the patient for the remainder of his or her life following PTCA. Because of this permanence, metallic stents can induce negative effects in the long-term, including late-stent thrombosis and in-stent restenosis [7]. Late-stent thrombosis occurs months or even years after implantation of the stent. Prolonged anti-platelet therapy is generally administered in the form of drugs such as warfarin or other coumarins to prevent late-stent thrombosis. These medications can induce other negative side effects in many patients, however, and can react with other medications and the patient's diet, particularly foods that contain high levels of vitamin K [8]. Long-term warfarin use is also associated with low bone density [8], and antithrombotic drugs increase the risk of bleeding [9]. In addition to the problem of thrombosis, in-stent restenosis is another major concern. The opposing force of the stent stimulates accelerated growth of the neointima, causing hyperplasia that results in narrowing and ultimately reocclusion of the vessel [7]. This problem can be combatted with special stents that are coated in an antiproliferative drug, known as drug-eluting stents

(DES). While DES have reduced neointimal hyperplasia in the long-term, the drugs used have been shown to increase the probability of late-stent thrombosis [7].

In addition to these issues, the presence of a permanent stent may cause long-term occlusion or vessel injury in infants and children, as the vessel continues growing but the stent cannot continue to expand beyond its maximum diameter. Further, a permanent stent may jail side branches, preventing intervention at nearby lesion sites.

The most common alloys used in permanent stenting applications are 316L stainless steel, nitinol (NiTi), and cobalt chromium molybdenum (Co-Cr-Mo) alloys. Nitinol is a particularly attractive alloy for stenting applications due to its shape memory properties. Stents are traditionally expanded through balloon angioplasty (balloon expandable, BX). Nitinol stents, however, are self-expanding (SX), exploiting their shape memory properties [10]. The stent is fully expanded when the metal is in its austenite phase, and deformed and collapsed when it is at its lower temperature martensite phase [11]. During deployment, the SX stents are attached to the end of a catheter and are kept in the martensitic phase by flowing cold saline through the catheter as it is guided to the affected site [11]. Once the stent is in the correct position, it is removed from the catheter. As the stent reaches body temperature, the SX stent transitions to its austenite phase, returning to its original expanded shape [11].

1.2.2 Orthopedic Implants

Traditionally, orthopedic implants are also composed of corrosion resistant metals and alloys due to their strength and fatigue durability compared with polymers and ceramics. In addition to structural integrity, an important factor in the long-term viability of an orthopedic implant is its elastic modulus. The elastic modulus of a load-bearing implant must be relatively low in order to prevent stress-shielding and subsequent resorption of bone tissue. For this reason, titanium alloys are the most commonly used materials for joint replacements. The elastic modulus of Ti6Al4V is typically around 114 GPa [12], while stainless steel alloys typically feature moduli of over 200 GPa [12]. The modulus of bone varies from about 1-27 GPa, so a lower modulus is ideal for orthopedic applications.

Metallic implants in skeletal repair date back to the ancient Egyptians and Etruscans [13]. Evidence of gold skeletal implants dating back to 2000 BC has been discovered in Peru [13]. The first structural metal used in orthopedic implants was vanadium steel, used in bone plates and screws [14]. Later, what is now known as 316L stainless steel was developed, exhibiting superior corrosion resistance to “vanadium steel” [14]. Stainless steel today is only suitable for temporary fracture fixation devices, as the combination of oxygen depletion and high stresses in certain regions of the implant accelerates the corrosion of these alloys [14], and the relatively high modulus can contribute to bone mass loss in the long term.

1.3 Corrodible Implants

When implanted in the physiological environment, all metals undergo some degree of chemical dissolution. Traditional metal implants are designed to minimize this dissolution. While there are several applications where a permanent device is required and thus a corrosion resistant metal is a necessity, there are other applications where the implant serves a transient function. Notable examples are cardiovascular stents and surgical pins and screws. Recently, researchers have sought to exploit the dissolution of metals in the physiological environment in order to create materials that will serve this transient function and degrade after the affected tissue has sufficiently healed. While several different corrodible metals and alloys have been considered, not all are suitable. A resorbable metal must not only degrade in an appropriate time frame, but also induce minimal inflammatory and thrombotic responses in the host. The following sections discuss various candidate materials for bioresorbable metallic bioimplants.

1.3.1 Magnesium Implants

Magnesium has shown considerable promise for use as an absorbable metal stent (AMS) material. Preliminary human trials for the treatment of critical limb ischemia with magnesium (>90%, alloyed with rare-earth elements) stents showed success in all 20 patients, with a 3-month clinical patency rate of 89.5% and a 12 month patency rate of 72.4% [15, 16]. No toxicity was observed in any of the patients, and the limb salvage rate was 94.7% after one year [15]. Schranz et al.

implanted a magnesium alloy stent (AMS, Biotronik) into the aorta of a 3-week old male patient to treat recoarctation of the aorta [17]. Follow-up angiography revealed that the vessel had begun to return to its original damaged state upon degradation of the magnesium stent, requiring implantation of a second stent [17]. This suggests that the absorption rate of the magnesium alloy is too rapid to support the vessel for the duration of the healing process. In spite of the insertion of the second stent, the levels of magnesium in the patient's blood were not elevated [17]. The Biotronik magnesium alloy stent was also tested in the Clinical Performance and Angiographic Results of Coronary Stenting with Absorbable Metal Stents trial [18]. The stent was completely absorbed within 2 months, with radial support lost possibly within days of implantation [18]. No deaths, thrombosis, or heart attacks were reported as a result of the stenting, but these stents were associated with a high restenosis rate [18]. This is likely due to their low radial strength and rapid degradation rate. Based on this information, it is clear that magnesium stents are relatively biocompatible, but their strength is too low and their resorption rate too rapid to prevent vessel recoil for the duration of the healing process.

Heublein et al. implanted six magnesium alloy discs, 200 μm thick and 3 mm in diameter, subcutaneously into rats to assess the corrosion effects and inflammation due to these materials *in vivo* [19]. The material that produced the least detrimental effects, composed of 2% aluminum and 1% rare earth elements (Ce, Pr, Nd), was then implanted as a coronary stent into pigs [19]. No in-stent thrombosis was detected in any of the pigs, while one pig died shortly after implantation due to unknown causes[19].

Waksman et al. reported on the implantation of the PROGRESS-AMS magnesium stent from BIOTRONIK into 63 patients for the treatment of coronary lesions [20]. Ultrasound imaging showed that the stents degraded in about four months, with no adverse effects to the vessel wall, nor calcification observed [20]. Early recoil causes restenosis, therefore improving degradation profiles is necessary in order to make magnesium stents viable candidates for clinical intervention [20].

In 2005, Zartner et al. implanted a resorbable magnesium stent, consisting of less than 10% rare earth elements, into a 6-week old preterm baby, born at 26 weeks gestation [21]. In an attempt to ligate the arterial duct, the left pulmonary artery was unintentionally ligated, resulting in respiratory failure and occlusion of the left pulmonary artery [21]. The left pulmonary artery was sharply bent, preventing angiography past the stenosis, so a resorbable magnesium stent was introduced to re-establish perfusion to the lung 15 days after the initial ligation [21]. Re-perfusion was established in the lung, and no toxicity due to the magnesium was observed [21]. In a follow-up paper, Zartner reported that the baby had contracted pneumonia and died 5 months later [22]. However, autopsy showed that the stent had completely resorbed with no traces and no necrosis had occurred [22]. The inner lumen diameter of the left pulmonary artery was 3.7 mm, indicating slight growth after implantation (from 3 mm), while the healthy right pulmonary artery had a diameter of 7 mm [22]. Additional *in vivo* studies are necessary in order to determine whether this intervention is viable for clinical use.

Even in vascular environments, magnesium forms hydrogen bubbles during the rapid degradation process and has a very short lifetime *in vivo* [23]. Because of this fast corrosion rate, the radial support may be lost too early, which can result in recoil and restenosis [20]. For these reasons, much work must yet be done on magnesium stents to determine the ideal alloy composition and stent geometry to ensure the degradation time is sufficient to support the vessel during healing, but rapid enough to prevent late-stent thrombosis and restenosis.

1.3.2 Iron Implants

Iron is an intriguing candidate for a resorbable metal stent as it is a corrodible material that is necessary in trace concentrations in the blood for proper oxygen transport, and is the fourth most abundant element in the earth's crust. Peuster et al. first reported on the *in vitro* and *in vivo* degradation of pure iron stents in 2001 [24].

The NOR-I stent, which is composed of pure iron, was implanted into 16 rabbit aortas [24]. Despite the slow degradation rate (struts were still detected 18 months past implantation), there were no cases of thrombosis or death [24, 25]. However, the stents caused considerable damage to the tunica media [24, 25]. Another disadvantage of a pure iron stent is that its ferromagnetic nature hinders magnetic resonance MRI compatibility [26].

1.3.3 Zinc Implants

Zinc has come to the attention of researchers in the last few years as a possible stent material due to its anti-inflammatory and anti-proliferative properties [27]. Zinc may be effective in reducing the risk of atherosclerosis, as it influences apoptosis of vascular endothelial cells [28]. Ren et al. found that the administration of zinc supplements to New Zealand White rabbits on a high cholesterol diet significantly reduced the size of atherosclerotic lesions compared with rabbits on a high cholesterol diet without zinc, and reduced the levels of Fe detected in the lesions [29]. This could potentially reduce the major problem of in-stent restenosis, which is one of the most common causes of stent failure [30]. It is believed that the zinc stabilizes the membrane of endothelial cells, preventing apoptosis [27]. In a recent study, Bowen et al. found that the cross-sectional area of pure zinc stent struts was reduced by >35% after 6 months of implantation in rat aortas [27]. Mechanical integrity of the stents must be maintained for approximately 4 months in order to facilitate vessel healing, and the zinc stent retained about 70% of its cross section at 4 months post-implantation [27]. While zinc has advantages in terms of antiatherogenic properties and degradation rate, it suffers from very low radial strength compared with other alloys [27]. The tensile strength of pure zinc is approximately 120 MPa, while a minimum of 300 MPa is desired to provide adequate support in a blood vessel [27]. In order to make zinc a viable stent material, its strength must be improved, possibly through alloying or processing.

1.3.4 Iron Manganese Implants

Due to its mechanical properties and its function in oxygen transport in blood, iron was chosen for the studies in this thesis as a base metal. Iron-manganese alloys have the potential to bridge the gap between pure iron's slow degradation rates and pure magnesium's rapid degradation, allowing for tailoring to the ideal degradation rate for a variety of implant applications [31]. Iron-manganese alloys containing more than 29 wt% Mn are completely austenitic and anti-ferromagnetic, which makes them more MRI compatible than 316L stainless steel [26, 31]. An alloy composed of Fe35Mn shows good ductility and a yield strength of up to 200 MPa [26]. Compared with pure iron, the Fe-35Mn alloy has a lower corrosion potential and a corrosion rate of almost three times that of pure iron [32]. Compared with 316L, Fe35Mn alloy shows similar toughness and significantly greater tensile strength, suggesting these alloys would provide adequate radial support to the vessel [32]. Recent studies have shown that compositions even as low as 0.5 wt% Mn exhibit good mechanical properties and low toxicity [33]. *In vivo* results from subcutaneous FeMn implants in mice with alloy compositions between 0.5-6.9 wt% Mn showed little to no degradation after 9 months, however, which is believed to be caused by the formation of a passive phospate layer on the surface of these implants [33]. Preliminary *in vitro* studies on the endothelial attachment on Fe35Mn showed a 200% increase in attachment compared with that on 316L [34]. The degradation rate, biocompatibility, and mechanical properties of iron manganese alloys make them an intriguing candidate for resorbable metal stents, but more research is still necessary to determine the utility of these materials for vascular interventions.

1.4 Effects of Surface Features on Bioimplant Compatibility

An important aspect of the performance of a biomedical implant is its surface. The surface interfaces with the biological environment and can influence the tissue response as well as the implant's useful lifetime. An ideal biomaterial surface will cause minimal tissue inflammation and toxicity, and exhibit ideal corrosion and wear behavior for the function it serves. For permanent implants, this means the implant must be non-toxic and non-inflammatory for the entire life of the patient and must not corrode or wear significantly. For resorbable implants, this means the surface must be uniform in order to facilitate uniform corrosion behavior and prevent localized corrosion, which can lead to stress-corrosion cracking, and the degradation products must be non-toxic and non-inflammatory.

Another important factor in the biocompatibility of a bioimplant is its surface wettability. The hydrophilicity of the surface of a biomaterial has been shown to play an important role in initial protein and cell adhesion. The proteins that bind to the surface influence the type of cells that are able to adhere, which ultimately determines the type of tissue that forms surrounding the implant [35].

The surface topography of a biomedical implant can greatly influence cell adhesion and behavior, with the potential to even influence the differentiation of stem cells in order to stimulate the formation of a particular tissue from multipotent or pluripotent progenitors [36]. Cell behavior in vivo is controlled by chemical and topographical cues. These topographical cues are provided by the extracellular matrix, which features structures from 6 to 200 nm in size [37]. The extracellular matrix surrounding different types of tissue exhibits disparate structures that influence the differentiation of primitive cells into specific tissues. It has long been known that microscale features influence cell behavior, since Harrison showed in 1911 that embryonic cells grown on spider webs orient themselves along the web, whereas cells suspended in a liquid drop were unable to move [38]. Recent research suggests that nanoscale features have equally profound effects on the behavior of cells. One possible explanation for the influence of nanoscale features on cell behavior is that the cells react to these morphologies by expressing various extracellular macromolecules, which in turn control their adhesion to the surface [39].

A variety of surface treatments have been used on biomedical implant surfaces, varying from chemical treatment to physical abrasion and deformation, to ion and plasma surface modification in order to alter their surface chemistry and morphology. Nanoscale features have been produced through photolithography, electron beam lithography, polymer phase separation, injection molding, and hot embossing [40].

1.5 Proposed Research

The main goal of this research was to improve the surface characteristics of both traditional metallic bioimplants and novel resorbable metallic implants. Traditional implants, such as titanium alloys, must integrate well with the surrounding tissue in order to prevent implant loosening and tissue damage. Other traditional metals can be exploited for previously unseen uses, such as bioactive coatings for tissue repair. Noble metals, such as gold and palladium, are attractive candidates for these coatings and were examined in this research.

1.5.1 Objective 1: Determine the Hemocompatibility of Resorbable Metal Stents

While the degradation behavior and cytocompatibilty of resorbable iron manganese implants have been given much attention in recent years, no information on their effects on blood clot formation has yet been available. In order for these materials to be viable in vascular applications, they must not induce significant clot formation or immune response. The first objective addressed in this dissertation is to determine how these resorbable iron manganese alloys will behave in terms of thrombogenesis by comparing the levels of various blood coagulation factors they induce compared with traditional stainless steel stents. Currently, the commonly accepted method of determining in vitro blood compatibility is through exposure of the candidate materials to human or other mammalian blood, and testing for blood clotting lymphokine factors such as thrombin-antithrombin and β-thromboglobulin [41-44]. This is usually done in a pulsatile environment, with the stent inserted into flexible polymer tubing at human body temperature (37°C) in order to mimic physiological conditions [41]. To address the blood compatibility of the novel resorbable stent materials, we examine the induced levels of thrombin-antithrombin, β-thromboglobulin, and polymorphonuclear elastase in blood after exposure to these materials compared with 316L stainless steel, as a standard. The adhesion of thrombocytes, leukocytes, erythrocytes, and the formation of fibrin networks is examined through biological scanning electron microscopy (bioSEM). Porcine blood is used as a well-accepted model for human blood chemistry, in a peristaltic pump using silicone tubing as a surrogate for blood vessels.

1.5.2 Objective 2: Alter the Surface Morphology of Metallic Biomaterials in Order to Accelerate Endothelialization

Surface chemistry, morphology, and substrate stiffness have all been shown to influence the behavior of cells on the surface of an implant. The surface morphology in particular influences cell adhesion, by providing a scaffold for growth and proliferation. In order to accelerate cell adhesion, nanoscale features can be induced on the surface of a biomaterial through a variety of methods. Here, the use of ion beam irradiation is examined. The simultaneous implantation of ions and sputtering of surface atoms results in self-organized features on the surface [45], whose geometry and size can be controlled by ion energy, ion mass, angle of incidence, temperature, and ion beam fluence (the total number of ions to interact with the surface per square centimeter) [46]. Ion beam modification can influence a variety of surfaces, from polymers, to ceramics and metals [46]. Here, ion beam irradiation is applied to metal surfaces, ranging from noble metal thin films to silicon wafers, to bulk resorbable ferrous alloys. A wide variety of different morphologies can be generated on ion-beam irradiated surfaces, ranging from nanoclusters or dots to ripples, and various patterns in between, depending on the angle of incidence [47-50]. The structures can be apparently random, or they can exhibit a high degree of organization.

Ion beam irradiation is examined as a method to alter the surface chemistry and morphology of both non-corrodible and corrodible bioimplant materials. Silicon is examined as a model material for ion beam irradiation, while noble metal thin films on these silicon surfaces are examined due to their inertness in vivo. Ion beam irradiation is also extended to bulk metal specimens of iron manganese alloy. The surface composition, topography, and wettability of these surfaces are examined through x-ray photoelectron spectroscopy, scanning electron microscopy, atomic force microscopy, and contact angle goniometry.

1.5.3 Objective 3: Create Uniform Oxides on the Surfaces of Bioresorbable Iron Manganese in Order to Tailor the Early Degradation Rate and to Facilitate Uniform Corrosion

One of the major causes of the mechanical failure of medical implants is stress corrosion cracking. Stress corrosion cracking is very commonly found in conjunction with corrosion pitting on the surface of an implant. These pits generally form at defects and inhomogeneities in a surface, and can penetrate deeply into the surface of the metal. This raises the local stress, which can cause cracks to form in the surface, especially when the pitting is found in a region with a large applied mechanical load. While resorbable implants are designed to degrade over time, this degradation must be uniform in order to prevent catastrophic failure of the implant, and must be carefully controlled in order to match the healing rate of the tissue. Initial immersion of FeMn samples in simulated body fluids resulted in negligible early degradation due to the formation of a passivating iron oxide layer [51]. The goal of Objective 3 is to replace the native oxide that forms on the FeMn surface with one that is more uniform in order to control the early degradation of FeMn implants and prevent undesirable modes of degradation, such as corrosion pitting. This is expected to reduce the likelihood of stress corrosion cracking, and allow for further tailoring of the degradation rate to match the healing rate of the tissue. This will be done through chemical treatment of the iron manganese surfaces, through simultaneous etching with acid and oxidation with hydrogen peroxide.

These solutions also have the potential to alter the surface morphology of traditional metals, and so their effect on Ti6Al4V is also examined. Previous studies have shown treatment of Ti6Al4V with sulfuric acid-peroxide solutions result in the formation of “spongy,” porous surfaces that have the potential to improve osteoblast growth [52]. A rough, porous surface can provide a means to create an “interlock” between the bone and the implant, which may eliminate the need for bone cements

[53]. Here, we examine the effect of acid-peroxide solutions on Ti6Al4V surfaces, comparing the effects of phosphoric acid and nitric acid with sulfuric acid, which is readily found in the literature.

CHAPTER 2 AN EVALUATION OF IN VITRO HEMOCOMPATIBILITY

The following chapter has been published previously. An in vitro model for preclinical testing of thrombogenicity of resorbable metallic stents,Walker, E. K., Nauman, E. A., Allain, J. P., & Stanciu, L. A. Journal of Biomedical Materials Research A. Copyright ©. 2014, John Wiley & Sons, Inc.

2.1 Introduction

While the cardiovascular tissue engineering field has been dominated by polymers and stainless steels, the use of bioresorbable nutrient metals is a novel, less explored idea that brings together the advantages of combining the mechanical strength necessary for initial support with the capacity of resorption after tissue remodeling. Bioresorbable metals have the potential to yield implants for clinical applications requiring only transient structure, ideally resulting in well-healed native tissues. postoperative mechanical support is only necessary for approximately 3-6 months before tissue remodeling is complete [54]. Designing metallic stents that provide such initial postoperative mechanical support, but are later resorbed to leave behind a prosthetic-free vessel and avoid the potential long-term effects of a permanent prosthetic device would therefore be the next step up in the field. Nutrient metals, such as iron, manganese, magnesium and zinc, have the potential to provide high strength and become building blocks for bioresorbable, transient, medical implants. In the context of the complex biomaterials-tissue interface phenomena in the vascular field, blood compatibility will have a crucial effect on these biomaterials' successful implementation.

In many of these applications, a permanent stent is not necessary and may cause negative effects in the long term, including late-stent thrombosis and in-stent restenosis [18, 54-56]. In-stent restenosis (ISR), occurs in about 25% of patients and is mainly caused by the mechanical irritation of the vessel by the permanent device and by the interaction between the blood and the stent [55]. Drug eluting stents reduce endothelial cell proliferation, but increase thrombogenicity [57], necessitating antiplatelet therapy for a prolonged period post-implantation [15]. Thrombosis is increased when the stent is malapposed to the vessel wall [58]. Recently, temporary endovascular bypass for cerebral occluded artery recanalization was implemented addressing some of the issues mentioned above applying a permanent endovascular device [59]. However, this approach in the context of cerebrovascular reconstruction near brain aneurysm defects remains unclear and in particular, the need for a stent scaffold material that is removed with a time constant correlated to the patency of the vessel, which in some cases could be several weeks [60].

In order to address these issues, interest in degradable stents has recently increased [61, 62]. Both polymer and metallic degradable stents have been explored. Polymer stents, typically composed of poly-L lactic acid (PLLA), suffer from lower radial strength compared with metals, which may be insufficient to prevent early recoil after implantation [15, 61]. This lower strength also requires much larger struts compared with traditional metal stents, which increases the hemodynamic impact of the stent and may contribute to thrombus formation [32, 63]. Polymeric stents also result in tissue inflammation and degrade relatively slowly [7]. Furthermore, they have a short shelf life and require specialized storage [7].

Resorbable metal stents of pure iron (Fe) and magnesium (Mg) alloys have been examined, due to their low toxicity and iron's role in oxygen transport. In clinical trials, Fe and Mg stents have shown good biocompatibility [61], but suffer from relatively low strength and stiffness compared with traditional permanent stents [32]. Pure iron stents degrade slowly, which may limit their ability to prevent late-stent thrombosis [18, 64]. Magnesium, on the other hand, degrades rapidly, which may not allow for sufficient vessel remodeling prior to resorption. Complete absorption of Mg alloy stents has been observed after 2 months [64]. Pure Fe is also incompatible with magnetic resonance imaging (MRI) due to its ferromagnetic behavior [32]. Here, we are reporting on the potential of iron-manganese alloys to address these issues.

Iron manganese alloys (FeMn) have advantages over pure iron and magnesium alloys in terms of mechanical properties and degradation rate. Cold drawn iron 35 wt % manganese (Fe35Mn) provided similar toughness and greater tensile strength than 316L stainless steel [32]. Further, alloys of Fe and Mn are MRI compatible at compositions above 29% Mn, with a purely austenitic structure [26]. Manganese is an essential trace element in mammalian function and development

[64]. Due to plasma protein binding, excess manganese has been shown to be non-toxic in the cardiovascular system [26, 65]. Preliminary testing has shown an increase in endothelial cell attachment on these resorbable FeMn alloys compared with 316L stainless steel [34], but further testing is yet necessary. The blood compatibility of a new material is an essential consideration in its viability as a stent material [66]. Thrombus formation and neointimal narrowing depend upon the triggering of inflammatory cells and platelets by the material [42].

The focus of this study is to determine the relative blood compatibility of resorbable stents composed of iron and iron-based alloys and drawn-filled tube (DFT) composites compared to traditional stainless steel. This was accomplished by the use of an *in vitro* porcine blood model and quantifying various coagulation factors in the blood, as well as imaging the stents after the blood contact to determine cell adhesion.

2.2 Experimental Methods

2.2.1 Stent Materials

Five different test materials and one control were assessed in this experiment. Surgical grade stainless steel (316L) was used as a control. The test materials consisted of composites of iron (Fe), magnesium (Mg), manganese (Mn), and zinc (Zn). Three of these wires feature a drawn-filled tube (DFT) geometry, where the core is composed of a different metal than the outer shell. The wire geometries can be seen in Figure 2.1. Additional detail on the processing and mechanical properties of these materials has been published previously [16]. The sample stents included 99.95% pure Fe (50% cold worked), Fe35Mn alloy, Fe35Mn-DFT-25% ZM21 (ZM21 is 2% Zn, 0.5% Mn, balance Mg), Fe-DFT-25% Mg, and Fe-DFT-57% Mg. All stents had identical geometry, formed by braiding 127 μm diameter wires into stents with an outer diameter of 6.35 mm. Six stents of each material were tested.

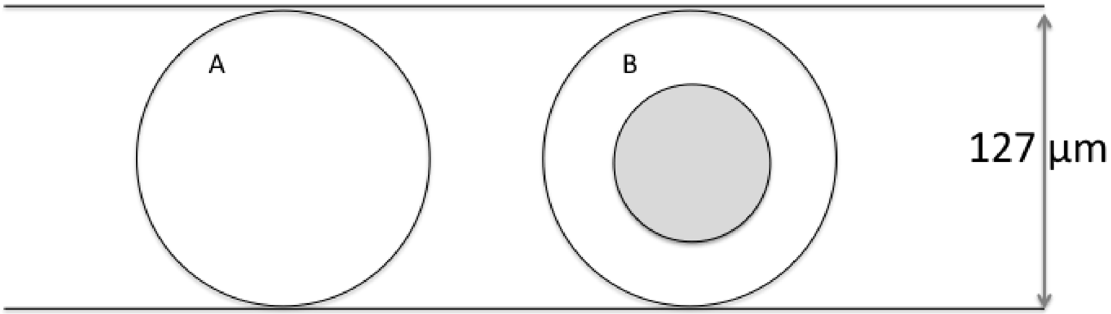

Figure 2.1 Wire geometries. (A) Monolithic wire comprised of Fe, 316L, or Fe35Mn, and (B) DFT wire comprised of an outer shell (white) of Fe or Fe35Mn, and a core of Mg or ZM21 (gray). The diameter of each wire is 127 um.

2.2.2 Experimental Set-up

The experiments were performed using closed loops of silicone tubing attached to a peristaltic pump. The tubing was immersed in a water bath at 37°C. The test stents were each inserted into a 30cm long portion of tubing with an inner diameter of ¼ in (Masterflex L/S, Cole Parmer, Vernon Hills, IL) that had been previously coated with heparin sodium salt to prevent tubing-related thrombogenicity. The stents were inflated with a balloon catheter (Balt Extrusion, Montmorency, France). The stented tubes were then each filled with 10ml blood and sealed. After 75 minutes of circulation at 33ml/min, the blood was collected and centrifuged to separate the plasma.

2.2.3 Blood Sampling

Porcine blood was obtained from the Purdue University School of Veterinary Medicine. Venous blood was collected from a single pig and doped with 1000IU/ml heparin. The blood was refrigerated overnight and brought to 37°C prior to insertion in the stented silicone tubes. Each stented tube was filled with 10ml of blood and sealed. Three ELISA assays were performed on each plasma sample in duplicate: porcine thrombin-anti thrombin complex (TAT), porcine beta-thromboglobulin (Beta-TG), and porcine polymorphonuclear (PMN) elastase. Red blood cells were counted in the whole blood samples before and after the blood was exposed to the test stents.

2.2.4 SEM Preparation

After blood contact, the stents were rinsed in phosphate buffered saline (PBS) and incubated in 2% glutaraldehyde in PBS. The stents were then rinsed in PBS and dehydrated in increasing concentrations of ethanol, followed by hexamethyldisilazane (HMDS). After dehydration, the stents were sputter coated with platinum for scanning electron microscopy (SEM). One stent of each metal composition was also imaged prior to blood contact for comparison. A third set of stents was exposed to the same fixation and dehydration chemicals to examine how these chemicals affect oxide formation on the degradable metals.

2.3 Results

2.3.1 Cell Counting

The red blood cell viability was assessed after contact with the sample stents and compared with blood that was not exposed to any stents. This was done visually with a hemacytometer for each stent. The viability of the red blood cells did not change significantly between samples (data not shown), and exceeded 90% viability in each case.

2.3.2 Blood Assays

Each plasma sample was assayed in duplicate for each of the sample stents, providing a total 4 specimens for each material in each assay. The assays were repeated 3 times, giving a total of n=12. The levels of TAT due to all of the resorbable metal samples were reduced compared to 316L, as shown in Figure 2.2a. Compared to the 316L control sample, the β-TG levels due to the cold-worked Fe and the Fe35MN-DFT-25% ZM21 were elevated, as shown in Fig. 2.2b. The Fe35Mn and Fe-DFT-Mg stents, however, showed a reduction in concentration of β-TG compared to 316L, as shown in Figure 2.2b. The Fe35Mn-DFT-25% ZM21 and Fe-DFT-25% Mg were comparable to 316L in terms of PMN elastase, while the Fe35Mn and Fe-DFT-57%Mg showed very low levels of PMN elastase, as shown in Figure 2.2c.

The statistical significance of the variations between the data sets was examined through unpaired t-tests for each resorbable stent type compared to 316L for each ELISA assay. The t-tests were performed in Microsoft Excel using the two-tailed assumption. The results of the t-tests are shown in Tables 2.1-2.3. Probabilities (P values) less than 0.05 are considered statistically significant.

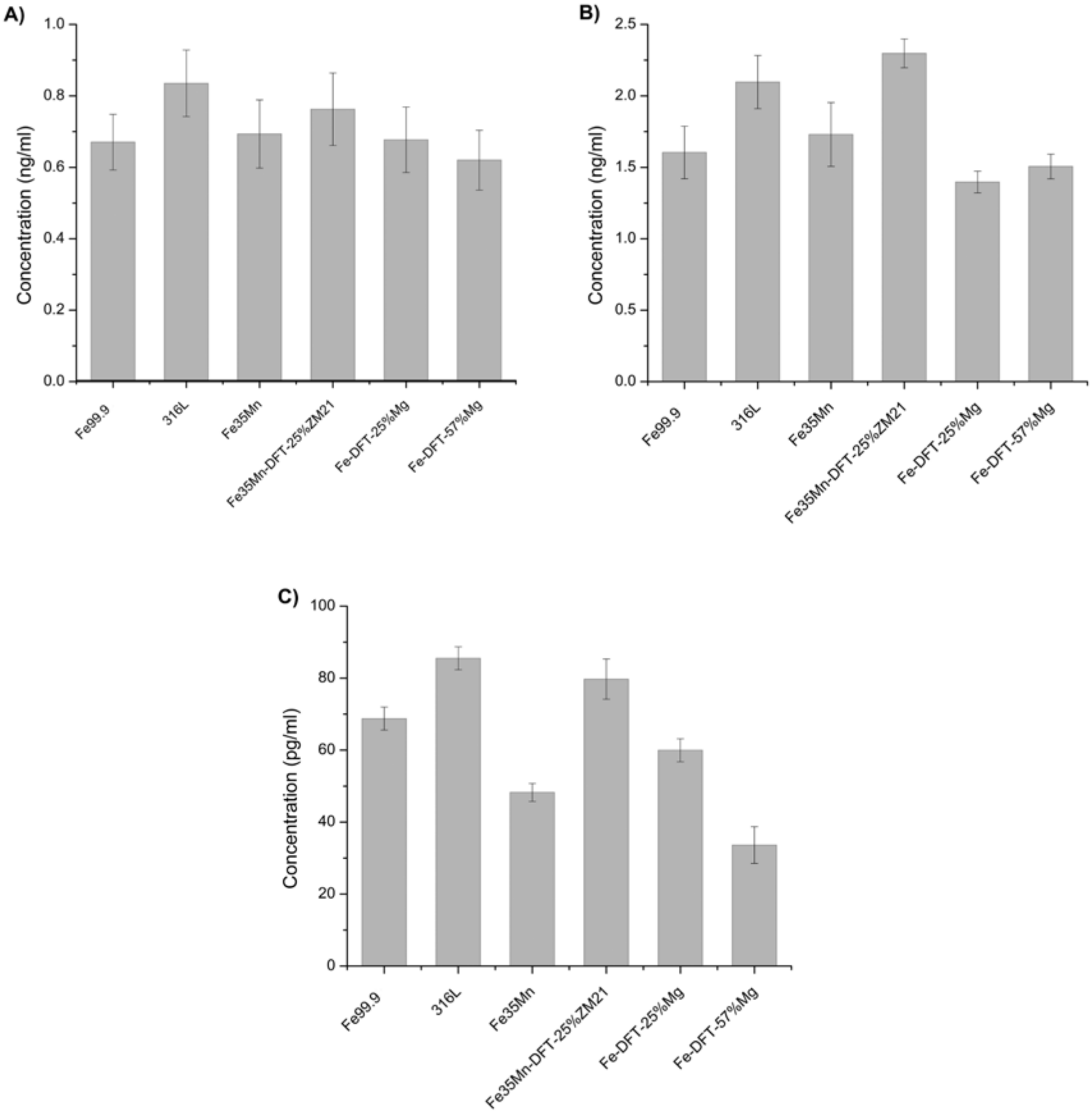

Figure 2.2 Concentrations of blood factors after contact with porcine blood from ELISA assays. (a) TAT, (b) Beta-TG, and (c) PMN elastase

Table 2.1 Statistical results for TAT ELISA (unpaired t-test for each resorbable material as compared to 316L). $P< 0.05$ is considered statistically significant.

Material	Mean Concentration (ng/ml)	P
316L	0.83	____
Fe 99.95	0.67	0.84
Fe35Mn	0.69	0.29
Fe35Mn-DFT-25%ZM21	0.76	0.63
Fe-DFT-25%Mg	0.68	0.34
Fe-DFT-57%Mg	0.62	0.11

Table 2.2 Statistical results for Beta TG ELISA (unpaired t-test for each resorbable material as compared to 316L). $P< 0.05$ is considered statistically significant.

Material	Mean Concentration (ng/ml)	P
316L	2.10	____
Fe 99.95	1.60	0.003
Fe35Mn	1.73	0.01
Fe35Mn-DFT-25%ZM21	2.30	0.29
Fe-DFT-25%Mg	1.40	0.005
Fe-DFT-57%Mg	1.51	0.0008

Table 2.3 Statistical results for PMN Elastase ELISA (unpaired t-test for each resorbable material as compared to 316L). $P< 0.05$ is considered statistically significant.

Material	Mean Concentration (pg/ml)	P
316L	85.50	____
Fe 99.95	68.75	0.27
Fe35Mn	48.25	0.004
Fe35Mn-DFT-25%ZM21	79.70	0.40
Fe-DFT-25%Mg	59.96	0.08
Fe-DFT-57%Mg	33.63	0.0009

2.3.3 SEM Imaging

In order to compare the effects of the blood cells with those caused by the fixation and dehydration process for imaging, a second set of stents was exposed to phosphate buffered saline (PBS) with a pH of 7.4, the same as the porcine blood, for 75 minutes and fixated and dehydrated using the same process described for the blood contact (chemically treated stents). After blood contact, the stents were imaged using backscattered electron imaging to examine both topographical features and phase contrast, in order to distinguish between metallic and biological particulates. The Fe35-Mn-DFT-25% ZM21 stent was damaged during this process and was not imaged using backscattered electrons. The unmodified and chemically treated stents were imaged with secondary electron imaging, as there were no significant changes in composition in these samples without the existence of biological specimens on the surface. These images are shown in Figs. 2.3-2.8.

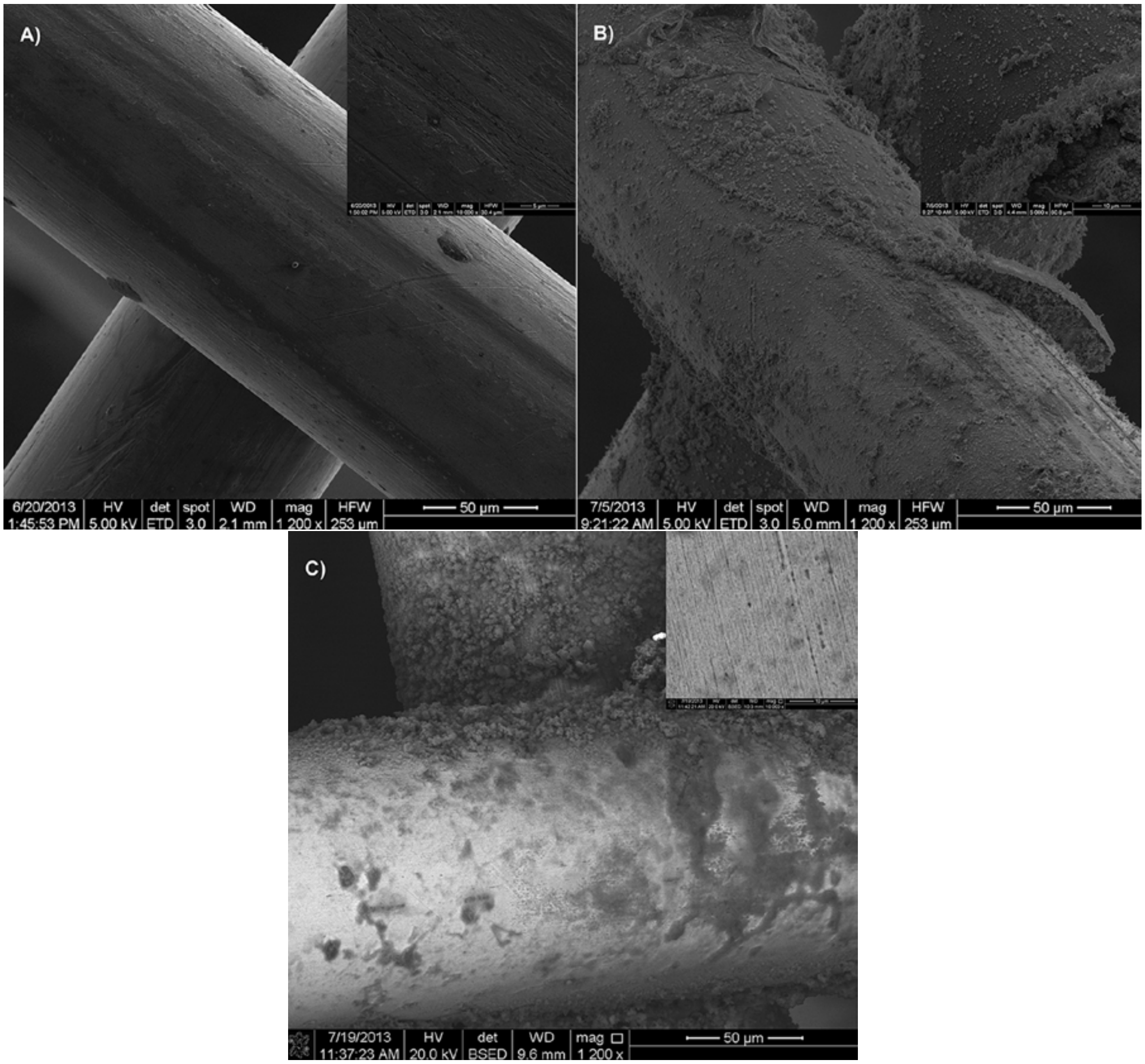

Figure 2.3 Secondary electron images of Fe 99.9% stent before (a) and after chemical treatment (b), and backscattered electron images after exposure to porcine blood (c).

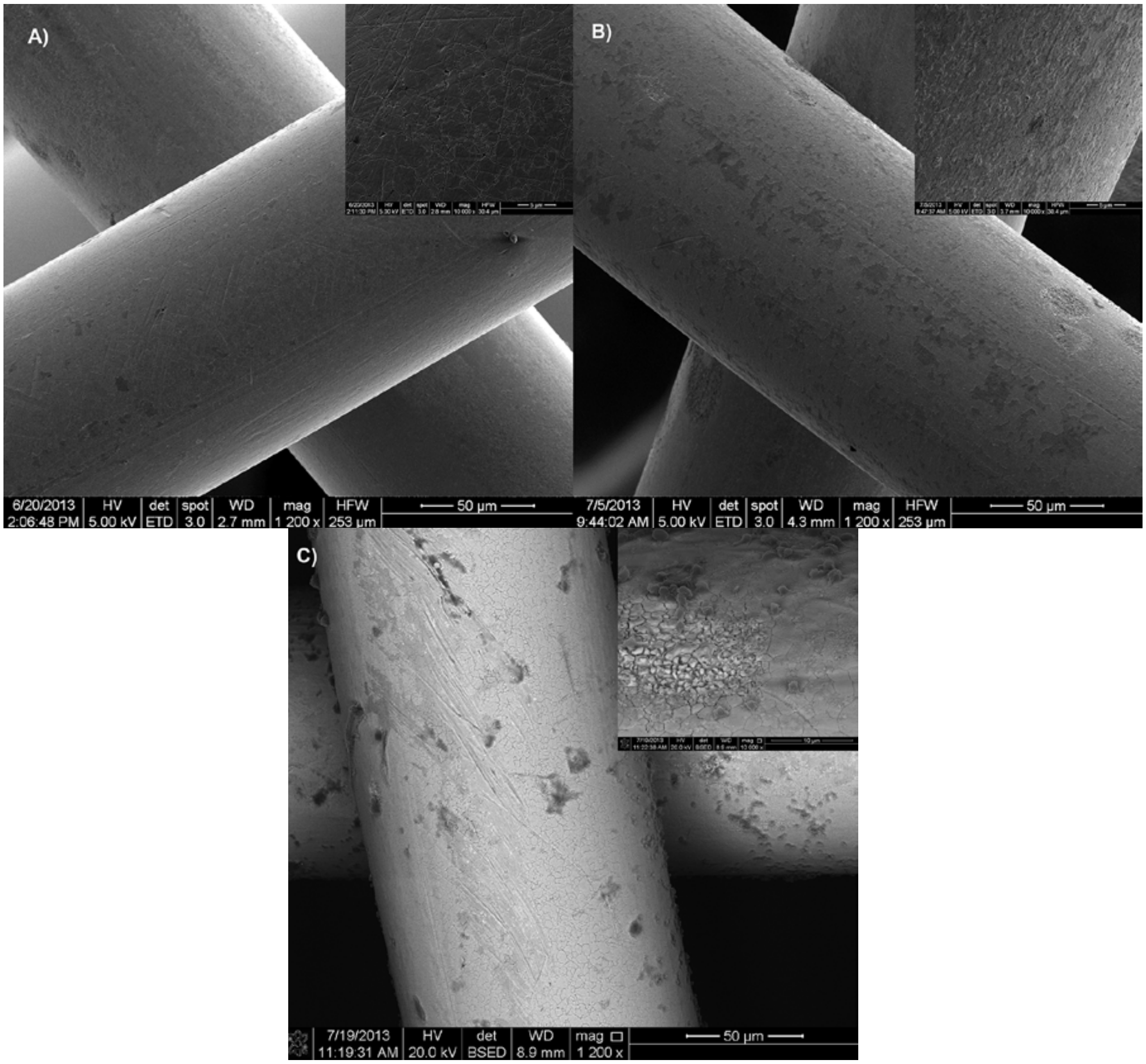

Figure 2.4 Secondary electron images of 316L stainless steel stent before (a) and after chemical treatment (b) and backscattered electron images after exposure to porcine blood (c).

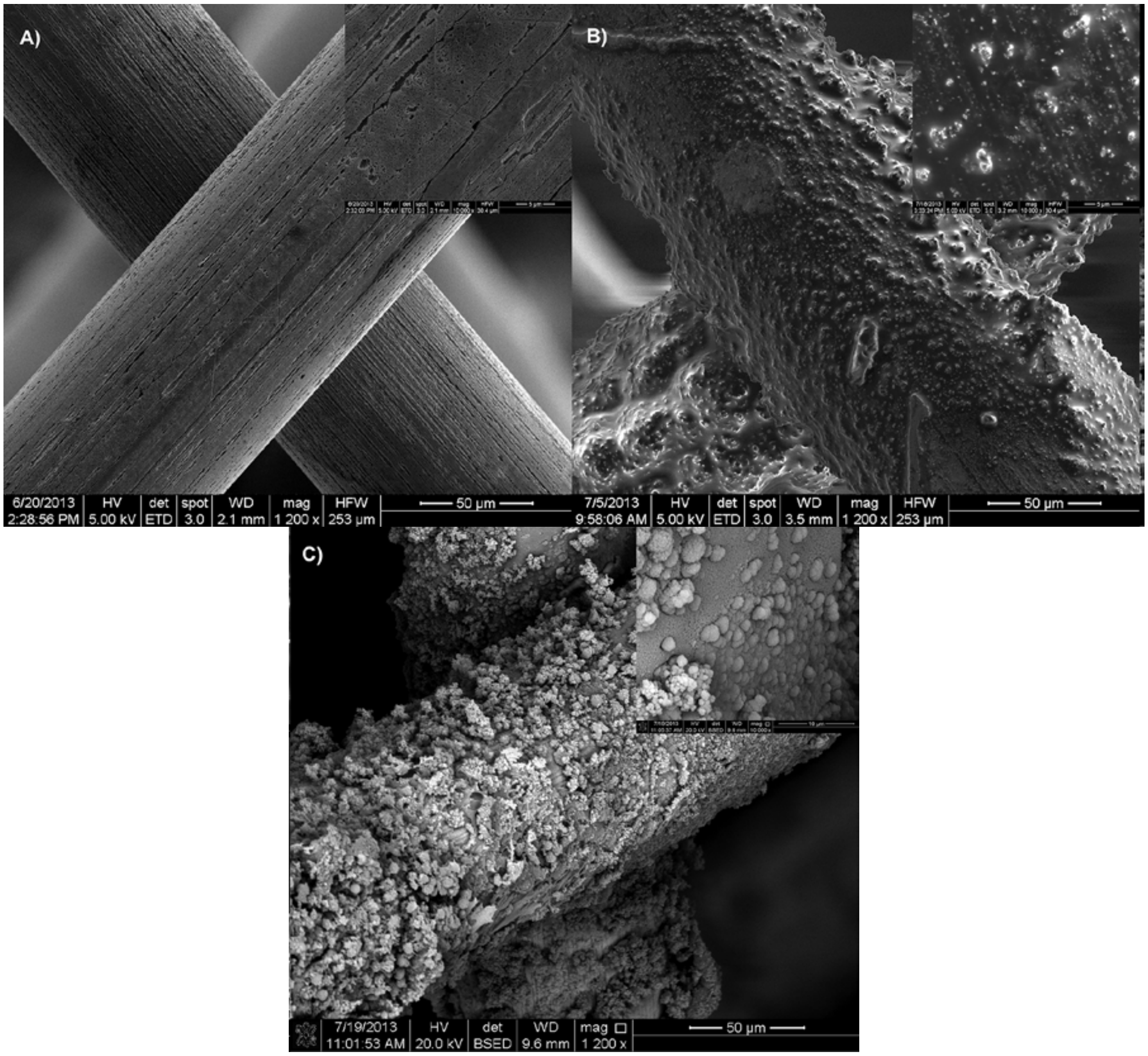

Figure 2.5 Secondary electron images of Fe35Mn stent before (a) and after chemical treatment (b) and backscattered electron images after exposure to porcine blood (c).

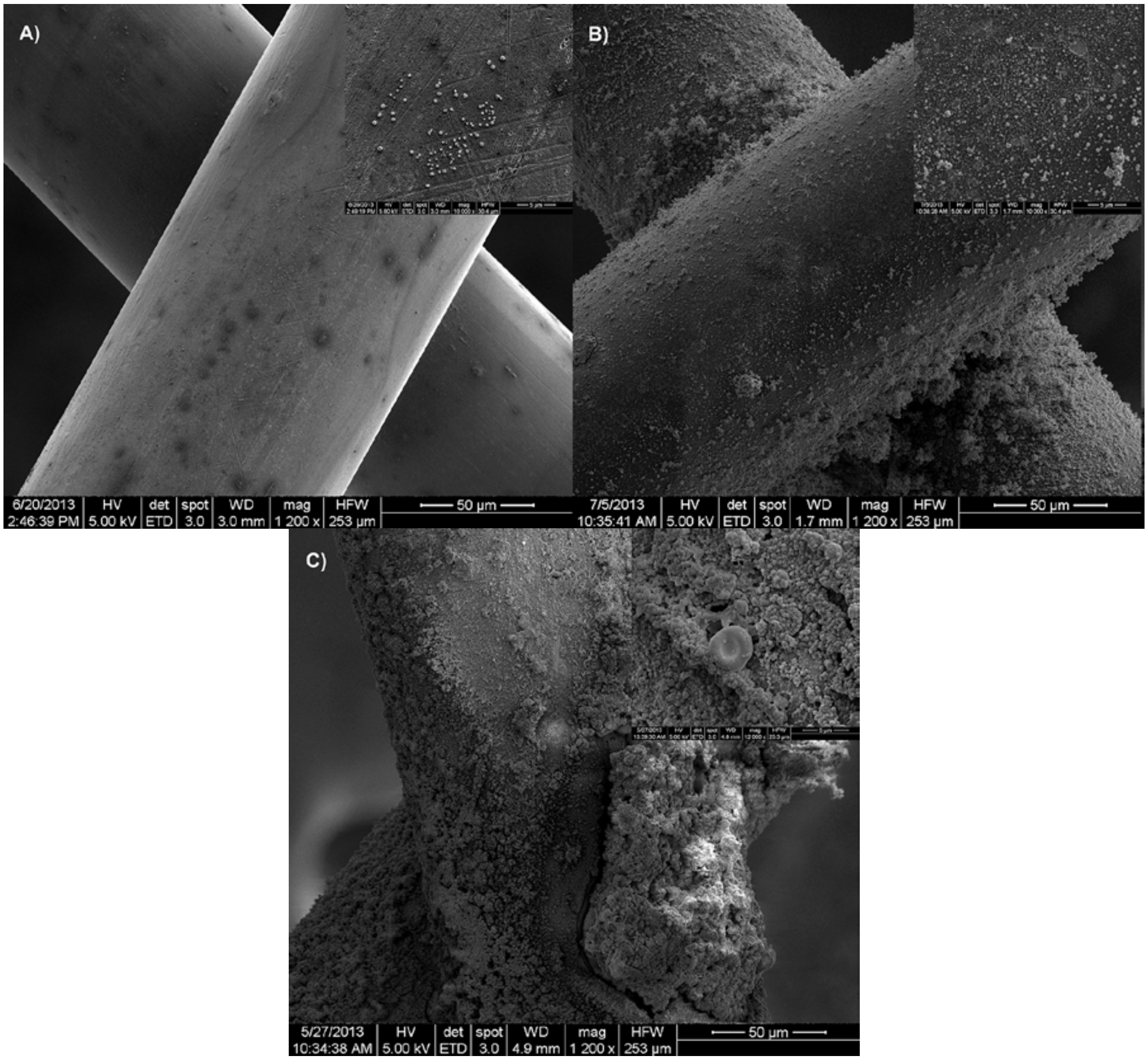

Figure 2.6 Secondary electron images of Fe35MN-DFT-25 % ZM21 before (a) and after chemical treatment (b) and after exposure to porcine blood (c).

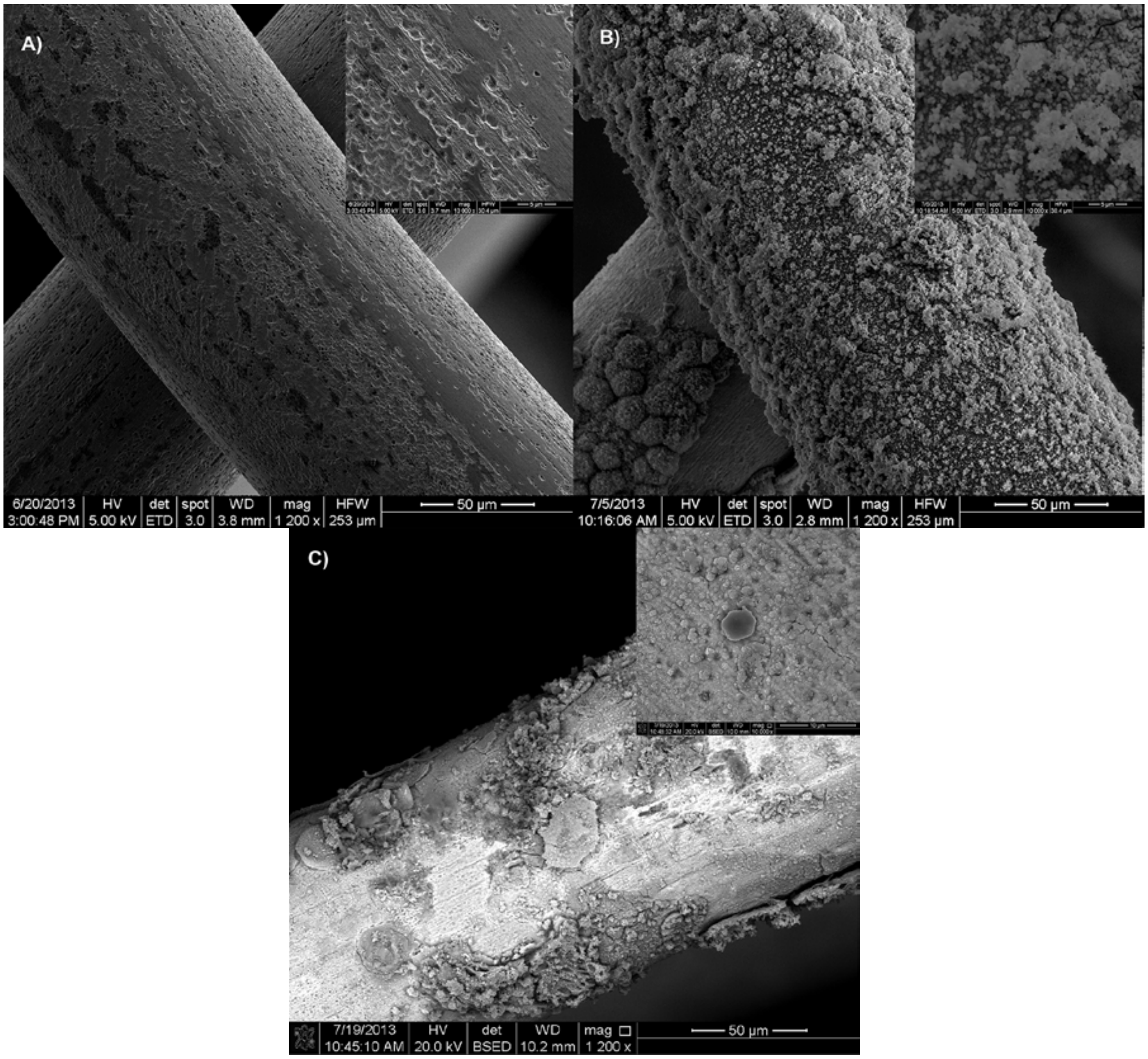

Figure 2.7 Secondary electron images of Fe-DFT—25% Mg before (a) and after chemical treatment (b) and backscattered electron images after contact with porcine blood (c).

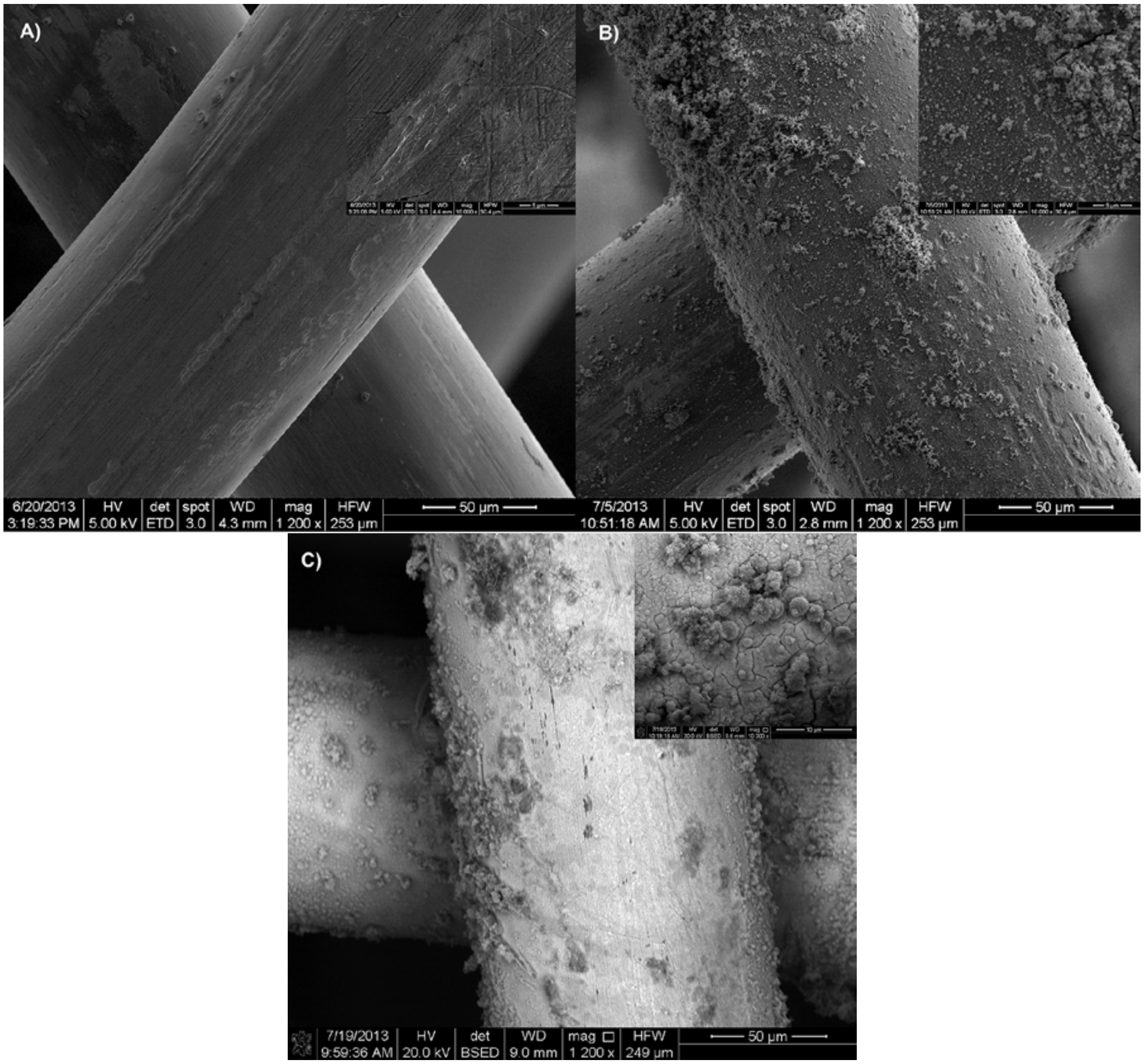

Figure 2.8 Secondary electron images of Fe-DFT—57% Mg before (a) and after chemical treatment (b) and backscattered electron images after contact with porcine blood (c

After immersion in the saline, fixation and dehydration chemicals, the iron stent showed significant surface oxide formation. This was especially apparent at the weld sites. SEM imaging of the iron stent in after blood contact showed significant rust formation as well as adhesion of few cells. The backscattered electron images in particular make the cells easier to distinguish from the degradation products. The lower atomic mass of the biological material results in a darker area on the backscattered image.

As expected, the stainless steel stent did not visibly degrade after chemical treatment. Several adhered cells are visible after blood contact. The size and morphology of these cells suggest that they are primarily thrombocytes, with several erythrocytes dispersed across the surface.

In the images of the as-received Fe35Mn stents, artifacts from the wire processing are evident on the surface. These became largely obscured by the formation of the surface oxide after chemical treatment, but the formation of the oxide layer was even more pronounced after blood contact. Very few cells were seen to adhere to the Fe35Mn surface compared with the stainless steel stent.

In contrast to the Fe35Mn stents, more erythrocytes and leukocytes were observed on the surfaces of the Fe-DFT stents after blood contact. Fewer thrombocytes, however, were visible on the Fe-DFT stents compared with the 316L stent.

2.4. Discussion

As the blood compatibility of FeMn alloys and Fe-Mg composites was assessed, an *in vitro* porcine blood model was selected as a widely accepted procedure [9]. The standards in this case were 316L stainless steel stents, with identical geometry to the test stents in order to eliminate the factor of geometry on thrombus formation.

Antithrombin III inactivates thrombin, which is produced during coagulation and binds to foreign contaminants. Thus a lower concentration of the thrombin-antithrombin complex indicates a reduction in fibrinogen activation [41]. PMN elastase is produced when an inflammatory response takes place due to the foreign material in the blood [41]. Finally, β-TG is excreted by platelets during activation [66]. Thus, these assays can be used to measure coagulation and inflammatory responses in the intrinsic pathway and detect the responses induced by the material being exposed to a blood environment.

Pure iron, which is one of the few clinically tested resorbable stent materials, induced lower levels of beta-thromboglobulin after 75 minutes in contact with whole porcine blood compared with 316L stainless steel, and similar, but slightly lower levels of PMN elastase and thrombin-antithrombin complex (Figures 2.2a and 2.2c). The difference between the beta-TG results for Fe99.95 versus 316L was statistically significant ($P<0.05$). The reduced levels of PMN elastase due to the iron stent suggest a decreased inflammatory response compared with stainless steel. The difference between the PMN and TAT results for pure iron versus stainless steel, however, was not statistically significant, as shown in tables 2.1 and 2.2.

Platelet activation and adhesion are well-accepted causes of thrombosis [67]. Placing a biomaterial in contact with blood leads to plasma proteins immediately adsorbing to the surface, a process that is followed by platelet adhesion and activation, activation of the complement and coagulation cascades, among other cellular responses. Consequently, if the platelets attached to the surface of a biomaterial are present in large number, and are at the same time modified in shape or tend to aggregate, this indicates they are highly activated, and the biomaterial shows reduced levels of anti-coagulation. In contrast, the presence of a small number of platelets on the surface and an intact shape suggest the platelets are not activated, and consequently demonstrates higher blood compatibility. A small number of platelets and red blood cells were observed on the surface of the Fe stent after blood contact, as shown in Fig. 2.3c, however a significant oxide layer formed. The morphology of this oxide layer was similar to that observed on the surface of the stent that was exposed to the same fixation and dehydration chemicals as the stent prepared for SEM after blood contact. These results suggest that the pure Fe stent will not increase thrombus formation compared with 316L.

Similar blood compatibility assays (beta-thromboglobulin, PMN elastase, and thrombin-antithrombin complex) as in the case of pure Fe and 316L were performed on the Fe35Mn stents. The results of the assays indicate improved behavior to 316L stainless steel stents in terms of acute thrombogenicity. After 75 minutes in contact with porcine blood, the measured levels of β-thromboglobulin, thrombin-antithrombin complex, and polymorphonuclear elastase were lower due to the Fe35Mn stent than the 316L stent, and lower than for pure iron. In this case, the difference between the Fe35Mn and 316L results were statistically significant for the PMN elastase and the Beta TG, but not for the TAT. This indicates that the Fe35Mn is comparable in terms of induced levels of thrombin-antithrombin complex**.** In addition, very few cells were observed to adhere to the Fe35Mn sample compared to the 316L stent through SEM imaging, as shown in Fig. 2.4c. The adhesion of the platelets depends on a number of factors, including surface roughness, surface energy, and surface chemistry. The host response to a biomaterial in the vascular system includes adsorption of proteins and activation of coagulation and inflammation [68]. This response is minimized by smooth surfaces [56]. During blood contact, however, a very rough oxide layer formed on the surfaces of the resorbable Fe35Mn, as shown in Fig. 2.5c. This suggests that the lack of platelet adhesion is likely due to the surface chemistry of the stent. Not only were very few platelets observed on the Fe35Mn surface, but very few leukocytes were visible as well, suggesting little inflammatory response due to the presence of this material. The oxide layer formed during chemical treatment differs from that of the oxide formed during blood contact, however. Prior to exposure to the blood and chemical treatments, marks from the wire processing were clearly visible, as shown in Fig. 2.5a. The surface oxide forms so rapidly that it is unlikely that these defects will have a significant influence on cell adhesion. Indeed, fewer cells adhered to the Fe35Mn surface, which initially had a rougher surface, than the 316L.

The drawn-filled tube stents likewise did not show an appreciable increase in thrombocyte adhesion or an increase in most of the coagulation factors, relative to 316L. The Fe-DFT-Mg stents had more adherent leukocytes on their surfaces, however. This was not observed on the pure iron stent, suggesting that the inflammatory response may not have been caused by the presence of the iron, but rather by the magnesium or the processing conditions of the DFT wires. Some flaking of the outer shell was observed through SEM on the surfaces of the DFT wires. This is an undesirable mode of degradation, as this debris could travel downstream from the stent and cause tissue damage in the blood vessel. This effect was not observed on the monolithic wires, however.

The absence of adhered platelets on the surfaces of the iron alloys and composites, while encouraging, does not prove conclusively that the materials are non-thrombogenic. The lack of platelets on the surfaces in the SEM images may simply be due to the surfaces being non-adherent, while the platelets may still have been activated and could ultimately form thrombi downstream from the stent [57]. The relatively low levels of the blood coagulation factors due to the resorbable metals, however, suggest that these metals will perform at least as well, or better than bare 316L stents. Among the tested metallic stents, the Fe35Mn composition showed the highest strength and longest lifetime and fatigue durability in previous testing [32], and has now proven to be the least thrombogenic in this *in vitro* study.

Previous studies have also shown greater endothelial cell attachment on the resorbable metal wires as compared to 316L stainless steel [34]. In fact, the Fe35Mn wires showed 200% greater cell coverage compared with 316L [34]. The combination of the improved endothelialization, excellent mechanical properties and degradation behavior, and comparable thrombogenic behavior to 316L suggest great potential for Fe35Mn as a resorbable stent scaffold material.

2.5. Conclusions

This study shows that the levels of beta thromboglobulin, and polymorphonuclear elastase, were reduced in the porcine blood exposed to Fe35Mn stents compared with blood exposed to 316L stainless steel stents, and the levels of thrombin-antithrombin complex were comparable. This suggests that the Fe35Mn stents will behave at least as well as 316L, or better when placed in contact with blood in clinical applications. The Fe35Mn-DFT-25% ZM21 stents induced comparable levels of TAT complex to 316L, but increased concentration of beta TG. Very little cell adhesion was observed on the resorbable metal stents compared with 316L stainless steel, but this does not conclusively disprove the possibility of thrombus formation due to the presence of these materials in the blood. No significant hemolysis was observed due to any of the samples tested in this study. The results of this study suggest the relative hemocompatibility of these resorbable metals compared to traditional stent materials.

CHAPTER 3 SURFACE NANOPATTERNING THROUGH ION BEAM IRRADIATION OF NOBLE METALS AND SILICON FOR IMPROVED BIOCOMPATIBILITY

3.1 Introduction

3.1.1 Penetrating Brain Pseudoaneurysms

Post-traumatic blast-induced penetrating brain pseudo-aneurysms have been a major concern for military personnel since World War I, and the prevalence of these injuries increased dramatically during Operation Iraqi Freedom (OIF) and Operation Enduring Freedom (OEF) [69]. Between April 2003 and April 2008, 408 military patients with severe head trauma returned to the United States from OIF/OEF and were treated at the National Naval Medical Center and Walter Reed Army Military Medical center [69]. More than one in three of these patients suffered cerebrovascular injury [69]. Penetrating Brain Injury (PBI) aneurysms are traditionally treated through surgical clipping, which requires open-head surgery, or through endovascular coiling, using platinum wires, often in conjunction with stent buttressing to hold the coils in place. Coating a stent in a material that would induce tissue growth and ultimately healing of the neck orifice of the pseudo-aneurysm could potentially provide a minimally invasive solution which could replace clipping and endovascular coiling, reducing the morbidity and mortality of these cases.

3.1.2 Control of Surface Morphology Through Ion Beam Irradiation

It has long been known that ion beam irradiation can influence the topography of a surface. Navez first showed topographical changes on glass due to air ion irradiation in the early 1960s, with the production of periodic nanoripples [70]. A wide variety of structures can be formed on surfaces in this manner [71]. By altering the parameters of the incident ion beam, a wide array of features of various sizes can be created on the surfaces of many materials, including metals and semiconductors. The factors that influence surface morphology induced by ion beam irradiation include ion species, ion energy, angle of incidence, target material, and film thickness. In addition to changes in the surface morphology, ion beam irradiation also induces changes in surface chemistry. Nanotopographical cues influence cell behavior [36, 39, 40], which can be exploited for a variety of medical applications, and the changes in surface chemistry can be used to create surfaces of various degrees of hydrophilicity.

Ion beam irradiation has been used extensively in order to create nanoscale features on the surfaces of semiconductors, as it provides a means to pattern areas up to several square millimeters in a manner of minutes [46]. Ion beam irradiation induced pattern formation can be achieved on a wide variety of materials, including metals and semiconductors, single crystal, polycrystals, or even amorphous materials [72]. Under certain conditions, low energy ion beam irradiation can be used to smooth surfaces, while other parameters can produce highly ordered patterns on a surface, with a variety of geometries possible. These patterns include, but are not limited to, dots and ripples. Pattern self-organization depends on target mass and crystal structure, ion species, ion energy, ion flux and fluence, and angle of incidence. According to Sigmund's theory, the local curvature has a profound effect on the erosion rate; erosion is accelerated at local minima, which leads to surface structuring [73]. For most metals and semiconductors at low energy with relatively lightweight ion bombardment, the collision cascade can be approximated to be linear [74]. Bradley and Harper extend Sigmund's theory in order to describe the formation of ripples on an irradiated surface, where the formation of ripples on a surface irradiated at oblique angles is analogous to ripples formed through sandblasting [75].

The sputter yield increases until about 60-70° from normal and drops sharply, as shallower angles result in energy deposition closer to the surface until glancing incidence results in more reflected ions [46]. The sputtering yield is also highly dependent on the crystallinity of a material, varying significantly for single crystal, polycrystalline, and amorphous targets and even varying significantly for different crystal orientations [46].

Argon ions were chosen due to their low cost and inertness; noble gases do not interact chemically with the target, leading to a simpler sputtering model.

Silicon is bioinert, but suffers from poor hemocompatibility [76]. Several studies have shown, however, that Si surfaces can be biofunctionalized to induce hydroxyapatite deposition [76], making it an interesting material for possible orthopedic applications. Under ion beam irradiation, Si surfaces become amorphized [46, 77].

Gold is an attractive candidate for biomedical implants due to its high corrosion resistance and inertness *in vivo*. Gold is one of the first biomaterials ever used in humans, used to treat cranial defects by the Egyptians and Romans [78]. Since then, it has become an important material for dental implants. Gold is radiopaque, and is commonly used as a marker on catheters for angiography to aid in visibility under x-ray fluorescence. Due to its ductility, it is an intriguing candidate for vascular applications. A nanostructured gold coating on the surface of a cerebrovascular stent could potentially serve as a scaffold material for endothelial and smooth muscle cells, inducing healing of aneurysm neck defects. The attraction of cells to the stent surface can be accelerated using a magnetic field, by depositing a magnetic film (i.e. nickel or cobalt metal) on the surface and then coating this magnetic film in bioinert nanostructured gold.

This chapter will discuss nanostructure formation on metal thin films, including gold (Au), palladium (Pd), and cobalt (Co) deposited onto silicon (100) wafers, as well as nanostructure formation on bare silicon (100) formed by inert argon ions with energies between 100eV and 500eV.

3.2 Materials and Methods

A Si (100) wafer was coated with a 1μm thick film of Ni, which was then coated in a 200nm thick film of Au for biocompatibility. Irradiation was performed using a broad-beam ion source in ultra-high vacuum at energies between 150eV and 1keV. Ex situ atomic force microscopy (AFM) and scanning electron microscopy (SEM) were employed to characterize the surface morphology of the irradiated materials.

Like gold, palladium is a popular choice for dental implants due to its inertness and good corrosion resistance. The application of a thin layer of palladium (~20nm) on the gold surfaces was added to aid pattern formation. Ion bombardment induces mixing irradiated layers. The mixed layer then undergoes preferential sputtering during ion bombardment. This was done on gold and palladium in order to induce preferential sputtering, as gold and palladium have different surface binding energies.

3.3 Results

3.3.1 Silicon Irradiation

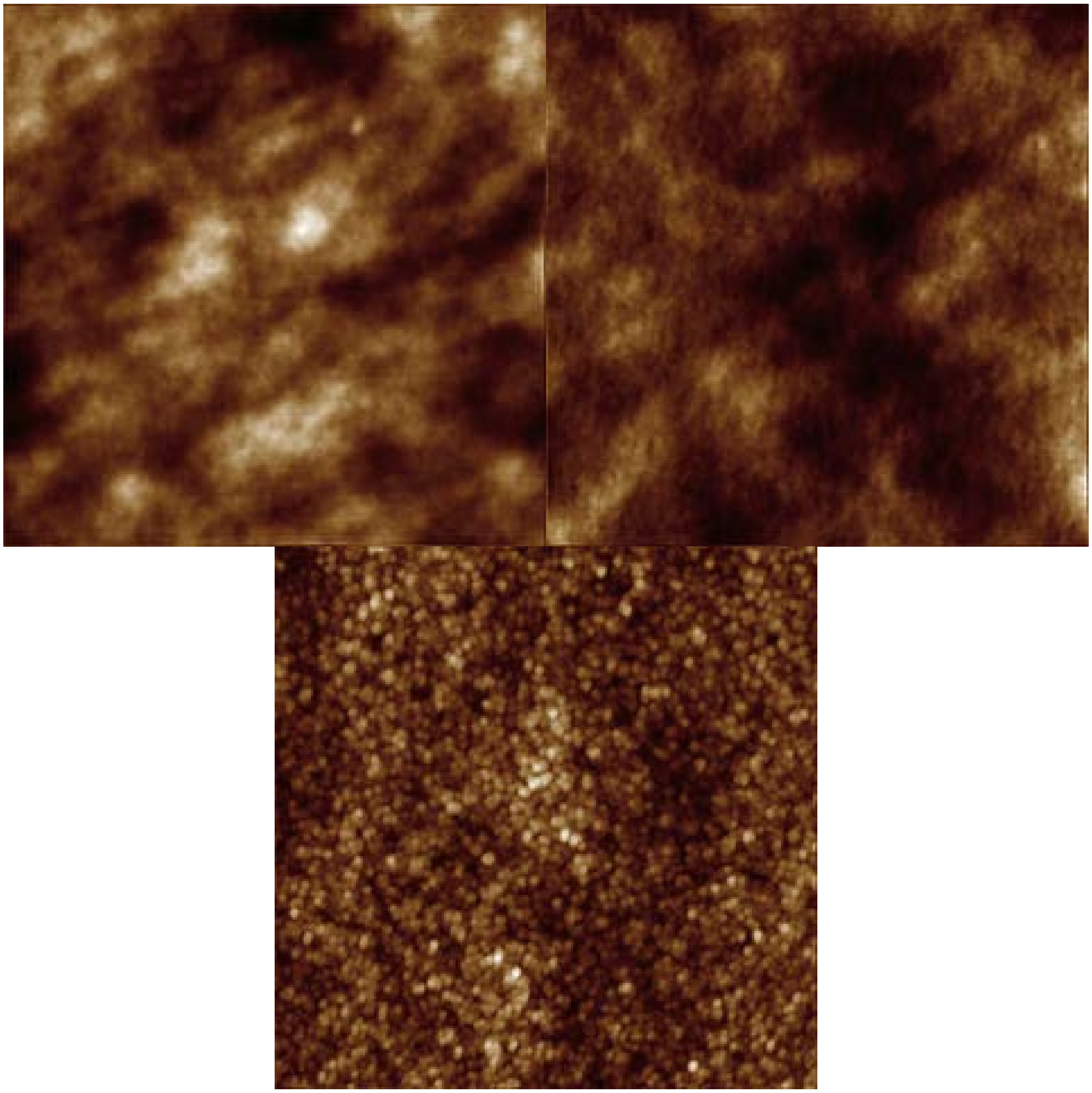

Figure 3.1 AFM images of silicon wafers irradiated with 150eV Ar$^+$ ions at 15° (a, b) and 70° (c) to fluences of 5E17 cm^{-2} (a, c) and 1E18 cm^{-2} (b). Each scan is 2.5 x 2.5 µm.

At the shallower incidence angle of 70°, shown in Figure 3.1c, patterning is visible on the surface of the wafer compared to the wafers with near-normal incidence (15°), as seen in Figures 3.1a and 3.1b at either fluence. From this, it is found that the near-normal angle of incidence creates a much smoother surface, while the oblique angle of incidence creates structures that are approximately 45 nm in diameter. When this experiment was repeated with 200eV Ar^+ ions at 10°, however, the irradiation resulted in nanoisland formation on the Si(100) surface, as shown in Figure 3.2.

Table 3.1 AFM analysis of Si wafers after 150eV Ar+ irradiation

Angle (degrees)	Fluence (cm^{-2})	Roughness RMS (nm)	Average Height (nm)	Maximum Height (nm)
15	5E17	0.44	1.64	3.13
15	1E18	0.49	1.66	3.80
70	5E17	1.29	5.19	10.62

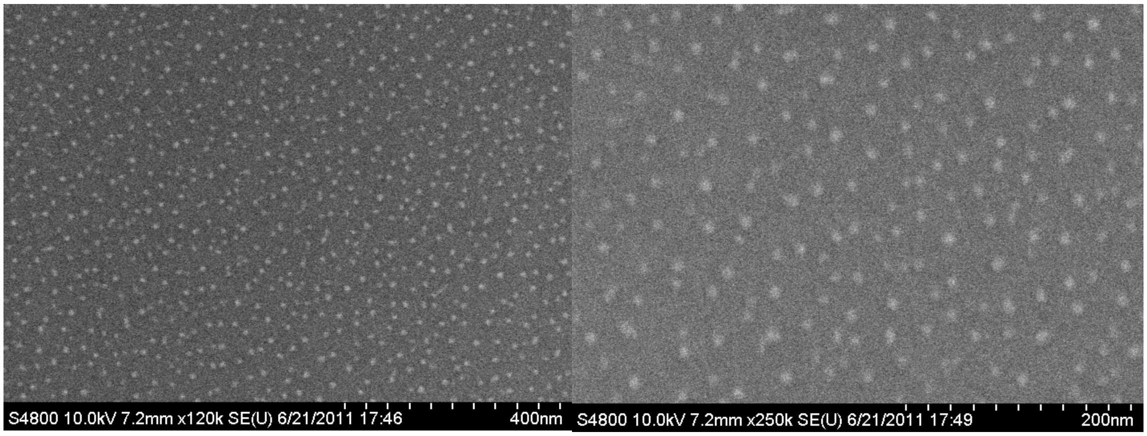

Figure 3.2 Silicon surfaces after irradiation with 200eV Ar^+ ions at 60° to a fluence of 6E17 cm^{-2} at 120,000x (a) and 250,000x (b).

Figure 3.3 : Silicon surface after irradiation with 200 eV Ar^+ ions at 10° to a fluence of 6E17 cm^{-2}

Irradiation of Si(100) at 10° resulted in ripple formation, but only in the near proximity of contaminants on the surface. A distinct shadowing effect is seen in Figure 3.3, where structures form to the left of a particle on the surface, but no features are visible to the right of the same particle. This is likely because the particle blocked the ion beam on one side, while the impurities from the particle contributed to atomic mixing and subsequent nanopatterning of the surface in this area.

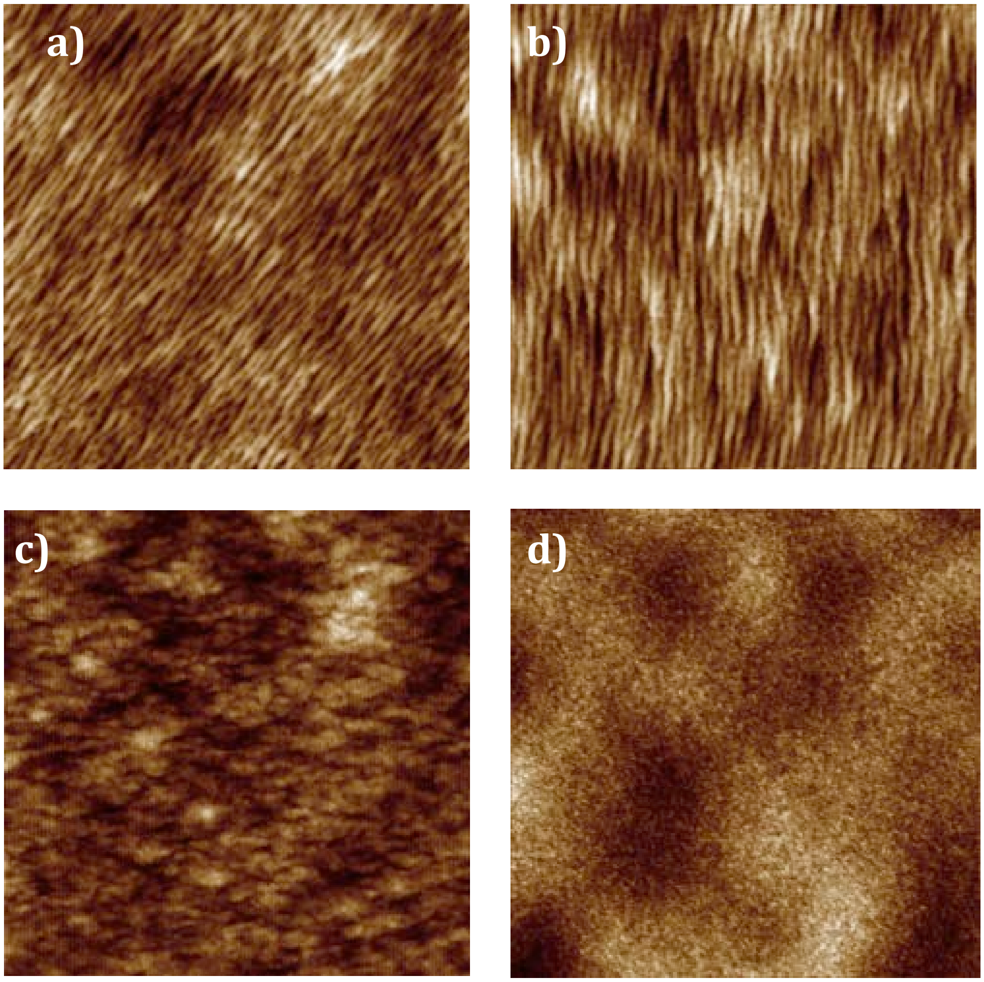

Figure 3.4 AFM scans of silicon samples irradiated with 200 eV Ar$^+$ irradiation with a broad beam ion source: (a) at 10° from normal to a fluence of 2E18cm^{-2}, 2.5 x 2.5 μm scan. (b) at 25° from normal to a fluence of 2E18cm^{-2}, 2 x 2 μm scan. (c) at 60° from normal.

At near-normal incidence, the ion beam induces the formation of ripples on the Si(100) surface, as shown in Fig. 3.3a-b. The ripples formed at 25° are wider than those created at 10°, however both are relatively uniform, as both were irradiated to the same fluence of 2E18cm^{-2}. At 60 °, by contrast, surface roughening is evident, but well-defined features are absent, as shown in Fig. 3.3c. Carter and Vishnyakov found that low-energy ion bombardment of Si at room temperature produced smoothing at near-normal incidence, and ripples at 45 °[79]. Ziberi et al, on the other hand, found 3 distinct regions of surface evolution on Si due to Ar+ ion irradiation: between 0° and 40°, ripples formed; between 40° and 60°, smoothing occurred; and at angles greater than 60, dots and columnar structures formed [80].

3.3.2 Gold Irradiation

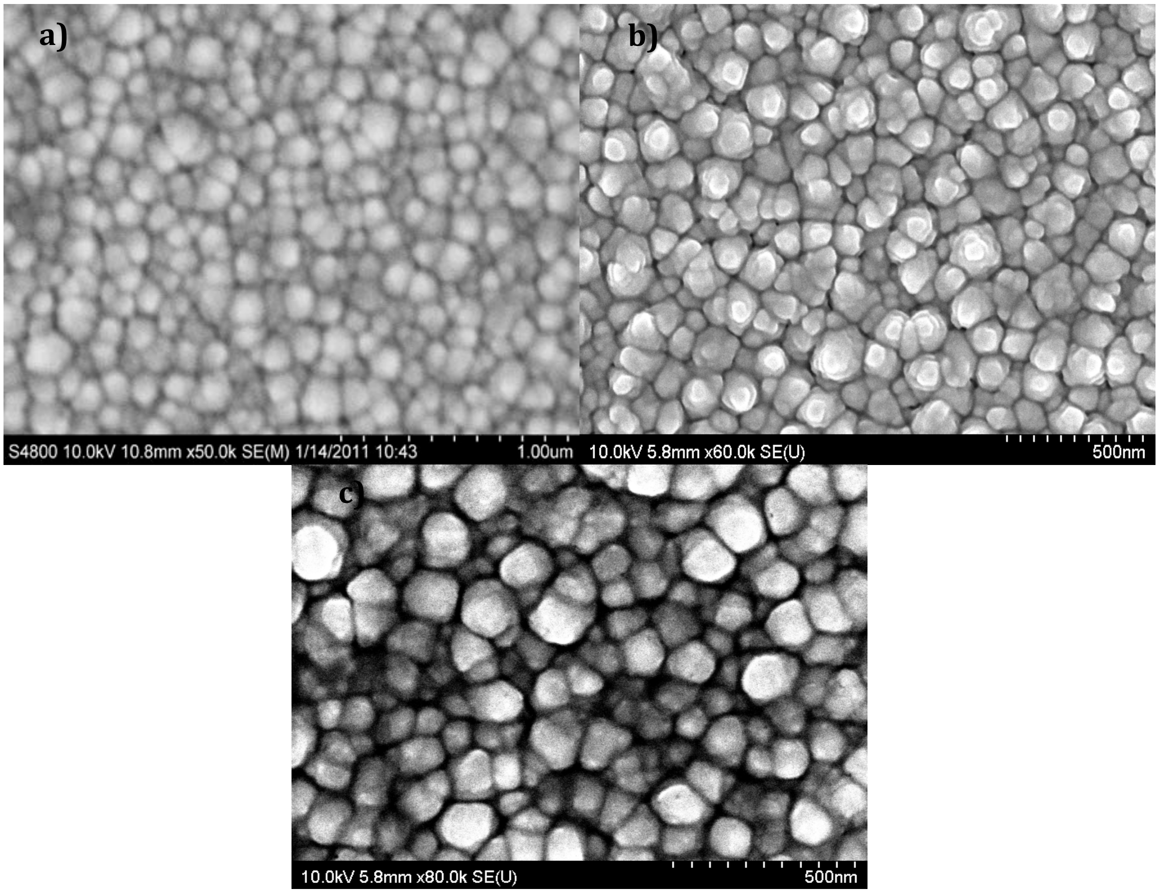

Figure 3.5 Figure 3.4: SEM images of 200nm gold films on 1μm nickel films before irradiation (a), after a fluence of 1E16 cm-2 (b), and after a fluence of 1E17 cm-2(c) irradiated with 500eV Ar+ ions at normal incidence (0°). (a) is at 50,000x while (b) is at 60,000x and (c) is at 80,000x.

Prior to irradiation, the gold surfaces were relatively rough. During film deposition, the gold particles agglomerated on the surface. No significant difference in the surface morphology was observed following irradiation.

3.3.3 Gold-Palladium Irradiation

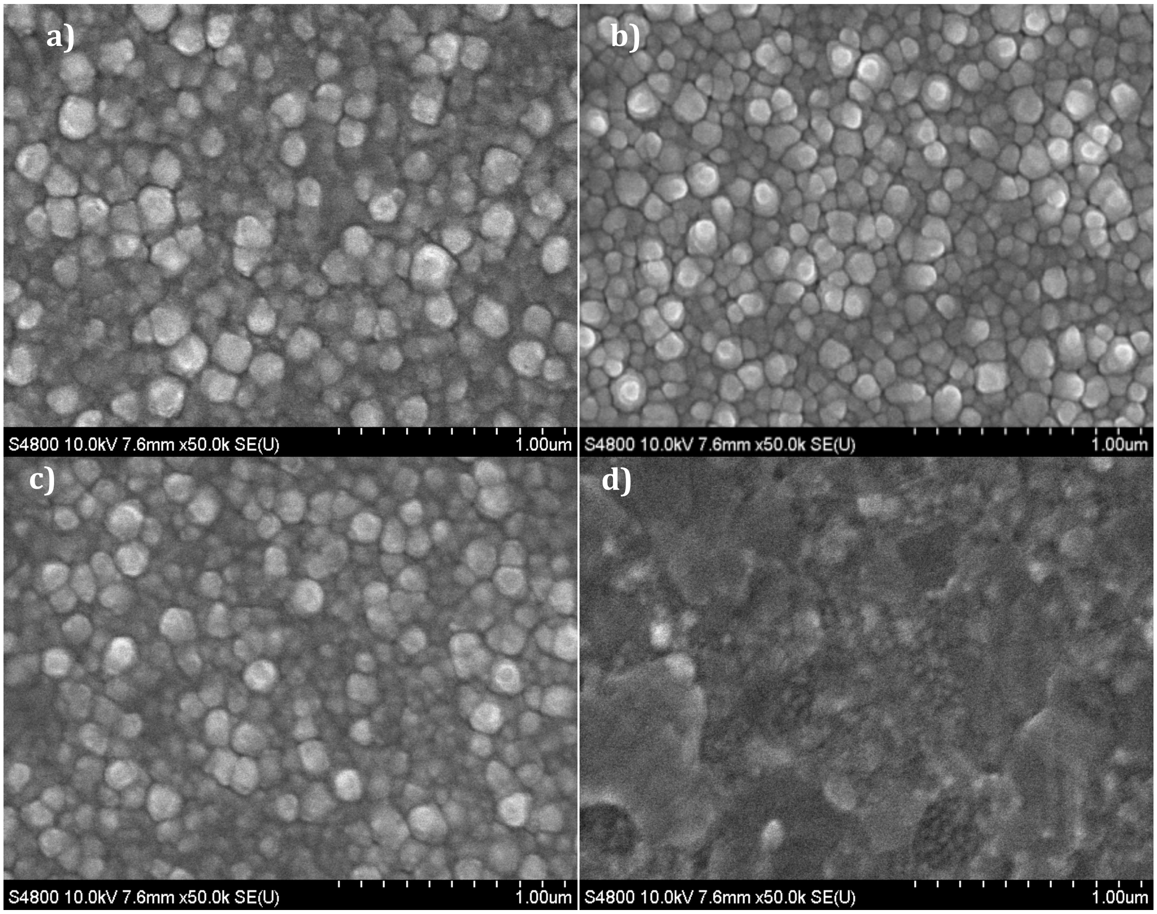

Figure 3.6 SEM images of Pd film on Au with Ni/Si substrates before irradiation (a), and samples irradiated with 500eV Ar^+ ions to fluences of (b) 5E16 cm^{-2}, (c) 8E16 cm^{-2}, and (d) 2E17 cm^{-2}.

Compared with the unirradiated surface, the two lower-fluence samples showed little change in surface morphology. After a fluence of 2E17 cm^{-2}, however, it appears that localized melting has taken place on the surface. The melting is not apparent in the AFM image in Figure 3.6d; it is likely that a different area of the surface was imaged in SEM versus AFM, and melting only occurred in specific regions, likely those that were bombarded with the highest intensity across the beam profile.

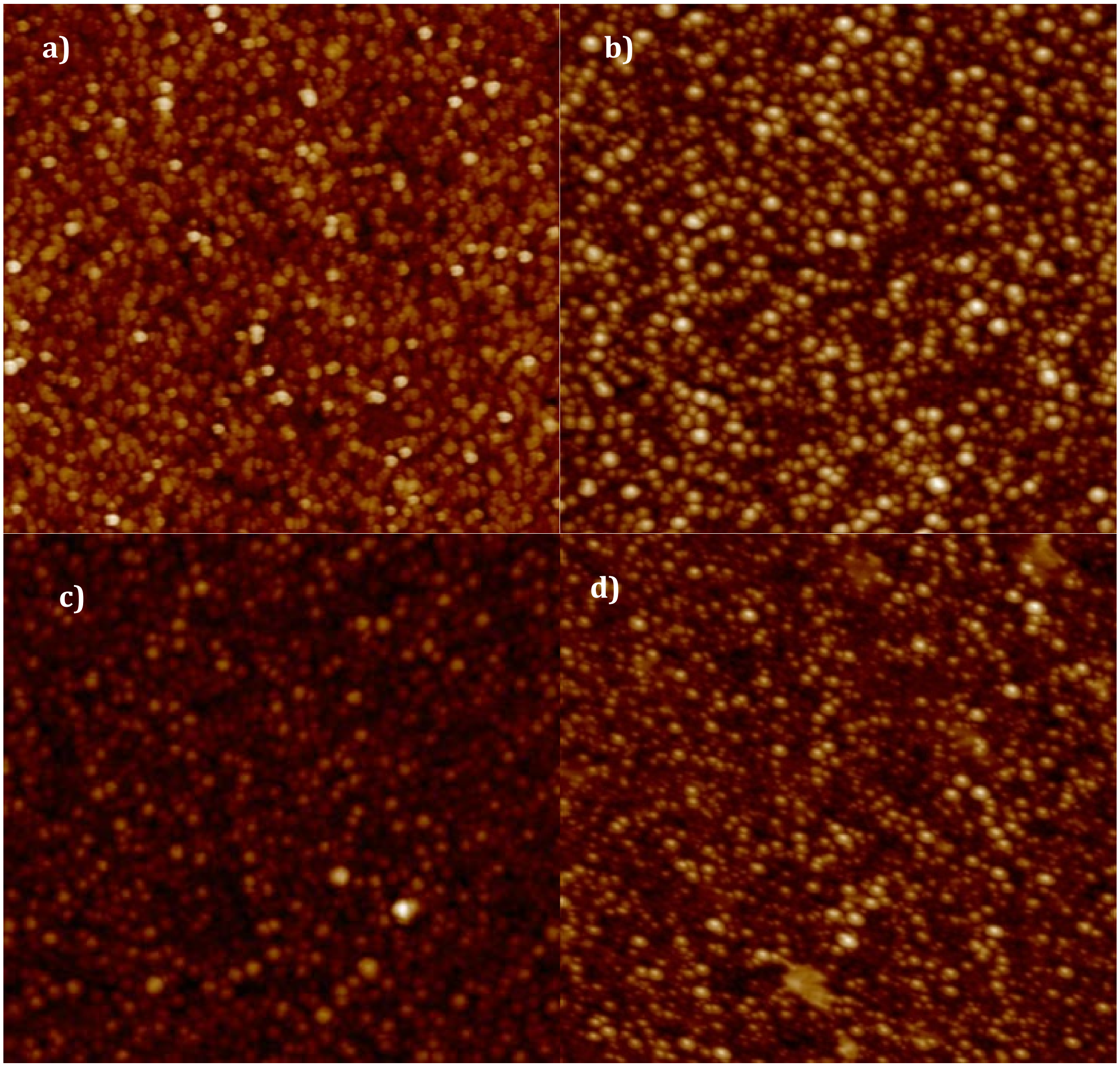

Figure 3.7 AFM scans of the Pd film on Au with a Ni/Si substrate before irradiation (a), and after irradiation with 500eV Ar$^+$ ions to fluences of 5E16 cm^{-2}(b), 8E16 cm^{-2} (c), and 2E17 cm^{-2}(d). Scans were all 5 x 5 μm.

The irradiated AuPd surfaces did not exhibit any significant changes in surface morphology, as shown in the AFM scans in Figure 3.6. Table 3.2 shows the quantitative results from the AFM analysis, where feature height, RMS roughness, and feature diameter were characterized. Only the sample irradiated to 8E16cm^{-2} showed variation in feature size, with slightly smaller features. The other samples varied insignificantly from the virgin surface.

Table 3.2 : AFM analysis of AuPd samples irradiated with 500 eV Ar+ ions.

Fluence (cm^{-2})	Roughness RMS (nm)	Average Height (nm)	Maximum Height (nm)	Feature Diameter (nm)
Virgin	17.0	44.7	123.4	~150
5E16	18.9	48.3	125.1	~150
8E16	13.9	38.7	111.8	~110
2E17	16.6	46.9	115.3	~160

3.4 Discussion

Irradiation of silicon (100) wafers with 200eV Ar^{+} ions resulted in nanoisland formation at 60° after fluences of 6E17 cm^{-2}, while near-normal angles of incidence created ripples on the surfaces. These ripples, however, only formed in the near proximity of visible contamination on the surface. Previous research suggests that ion beam-induced pattern formation on high-purity single-crystal silicon is not possible in the absence of metal impurities [81]. The formation of patterns on the surfaces of the Si(100) in this investigation may be induced by adsorbed impurities on the surface of the Si, impurities introduced during the manufacturing process, or the interaction of the ion beam with the metal platen supporting the sample in the vacuum chamber. The patterning at oblique incidence was most well-defined in the near-proximity of particles on the surface of the irradiated wafer, on only one side, suggesting a shadowing effect caused by the large particle blocking the shallow-angle ions. Irradiation at 70° with 150eV Ar^+ ions also produced nanodots on the surface.

Gold films were created on the surfaces of nickel thin films through electron-beam deposition, resulting in the formation of gold spheres nearly 1μm in diameter. The agglomeration of the gold particles on the surfaces of the nickel films is likely due to poor wetting of the gold on the nickel. No significant changes in the surface morphology were observed after ion beam irradiation on these surfaces. In order to induce preferential sputtering to drive nanopatterning, a thin layer of palladium was deposited on top of the gold. After high fluence ($2E17cm^{-2}$) irradiation with 500eV Ar^+ ions, the morphology of the Pd films deposited on Au changes significantly, while almost no change is perceptible at a fluence of $8E16cm^{-2}$. Prior to irradiation, the surface was covered in agglomerated spheres of palladium. After the highest fluence examined in this study, however, it appeared the surface had been melted. Gold and palladium are dense, soft metals. In targets with high density, the collisions from ion bombardment occur very close together, which melts the crystal, resulting in the surface observed in Figure 3.5d. Further experiments using a lower ion flux, but the same final fluence, could further elucidate the cause of the localized melting.

At a lower flux, the collisions would occur on a longer time scale, which might prevent melting of the surface.

3.5 Conclusions

Nanopatterning was induced on the surfaces of Si(100) wafers at various angles of incidence. This patterning was likely driven by the presence of impurities introduced by particulates present on the surface prior to irradiation or the interaction of the broad ion beam with the metal platen. These features ranged from nanoislands at oblique incidence to ripples at near-normal. It was not possible to induce nanopattern formation on gold thin films deposited on silicon wafers with magnetic films sandwiched in between. This is most likely due to the rough initial surface after electron beam deposition of the metal films. The deposited films were equally rough when the deposition was performed on a bare silicon wafer with no magnetic nickel film or chromium adhesion layer. The addition of thin layers of palladium did not induce any preferential sputtering-driven pattern formation, although localized melting was observed at high fluences.

CHAPTER 4 SURFACE MODIFICATION OF Fe35Mn THROUGH ION BEAM IRRADIATION

4.1 Introduction

Ion beam irradiation can be extended to resorbable metals in addition to thin films and semiconductors. in order to create nanostructures on the surface to influence cell behavior, and to preferentially sputter certain components of the alloy in order to create a specific surface composition. Preferential sputtering occurs in a system of multiple components where the sputtering yields of the components are different [82]. Generally, the component with the higher sputtering yield will preferentially sputter away from the material, leaving a surface rich in the component with the lower sputtering yield. The difference in sputter probabilities between two elements in an alloy can be attributed to differences in their surface binding energies, and differences in momentum transfer from collisions to these constituent atoms [83]. This effect is most pronounced at energies near the sputter threshold; virtually no sputtering will be observed from the component with the larger threshold, while the energy transferred to the other component(s) may yet be sufficient to induce sputtering [84]. In the case of FeMn irradiated with Ar^+ ions, the Mn has a higher sputtering rate, determined by Stopping Range of Ions in Matter (SRIM) calculations. The SRIM program assumes binary collisions only and does not take into account changes in composition due to sputtering or the formation of defect clusters, and assumes the material is amorphous. It was used in this case only to approximate the differences in sputtering yield between the two components under the same conditions. In contrast to the Si surface examined in the previous chapter, metals do not amorphize during ion beam irradiation due to the non-directionality of metallic bonding [46], but SRIM calculations do not account for crystallographic effects.

Previous work in our group has shown that rougher surfaces improve the adhesion and influence the orientation of bone marrow stromal cells grown on FeMn surfaces, as shown in Figure 4.1. After 20 hours in culture, the cells aligned themselves with the direction of the grooves induced by the grinding process, while the cells cultured on the smooth sample were randomly oriented and the coverage was less dense. The roughness and morphology induced by mechanical polishing is limited to scratches and grooves in the sample surface. Ion beam irradiation can be used in order to produce various feature geometries that may have varying effects on cell behavior.

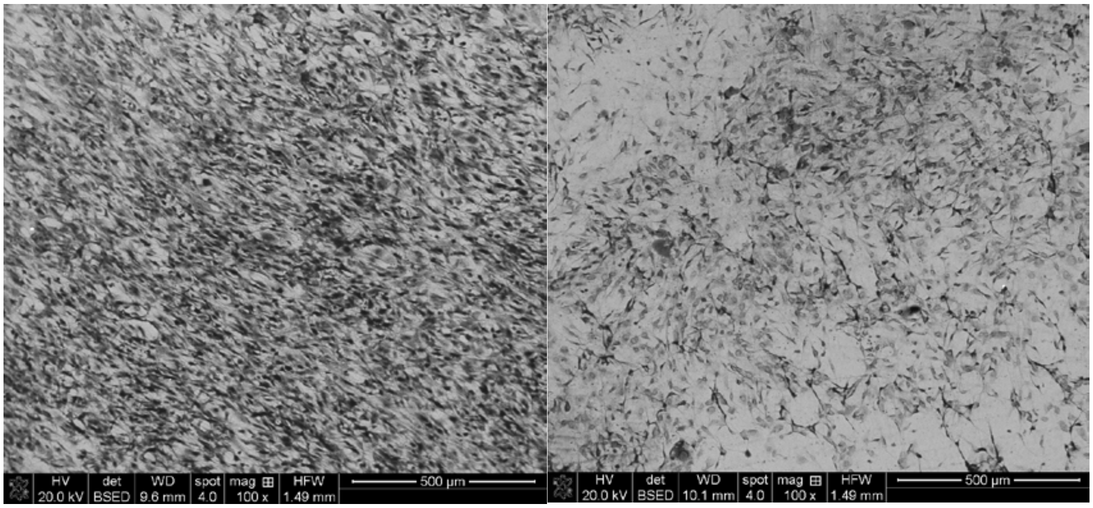

Figure 4.1 Backscattered electron images of bone marrow stromal cells cultured for 20 hours on FeMn surfaces ground to 600 grit (a) and polished to mirror finish with colloidal silica (b).

4.2 Materials and Methods

Small, irregular pieces of 99.9% pure Fe (Alfa Aesar, Ward Hill, MA) and 99.9% pure Mn (Alfa Aesar, Ward Hill, MA) were weighed out to 35% Mn, balance iron (Fe35Mn). This mixture was cast through arc melting under flowing argon (5%H_2) and re-melted three times to ensure homogeneity. Coupons 1 cm in diameter were machined from the resultant ingot. The coupons were then ground to a final grit of 600. Argon ion beam irradiation using a broad-beam ion source was carried out in an ultra-high vacuum environment. *In situ* x-ray photoelectron spectroscopy (XPS) was performed on the samples prior to irradiation, after a fluence of 2E16cm^{-2}, and after a fluence of 5E17cm^{-2}. The XPS data was used in order to determine the surface composition of the samples prior to and following irradiation. After irradiation, the surface morphology of the samples was examined through scanning electron microscopy. CasaXPS analysis software was used to find the area underneath the peaks in the XPS spectra, which was then used to calculate the proportions of iron, manganese, and oxygen at the surface. The wettability of the irradiated samples was measured through contact angle goniometry with deionized water.

4.3 Results

Prior to irradiation, a thin, non-uniform native oxide is present on the iron manganese surface. The O 1s peak and the O KLL Auger peak are apparent prior to irradiation and after a fluence as 2E16cm^{-2} in figures 4.2-4.4. The lower fluence of 2E16^{-2} was chosen as this low fluence results in sputter-cleaning of the topmost layer of the surface, prior to the onset of morphological changes and ion implantation and mixing. XPS analysis of the surface after this fluence provides better information on the composition of the material below the surface oxide compared with the as-polished sample.

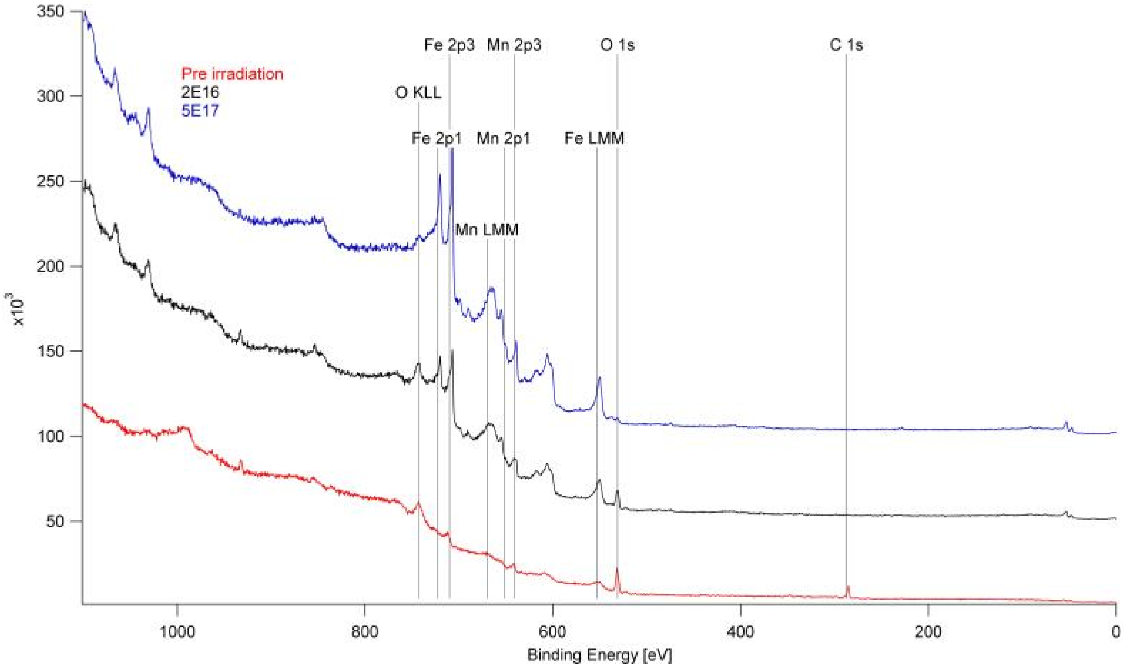

Figure 4.2 XPS results for Fe35Mn irradiated with 500eV Ar+ ions at 60° before irradiation (red), at a fluence of 2E16 cm^{-2} (black), and at a final fluence of 5E17 cm^{-2} (blue).

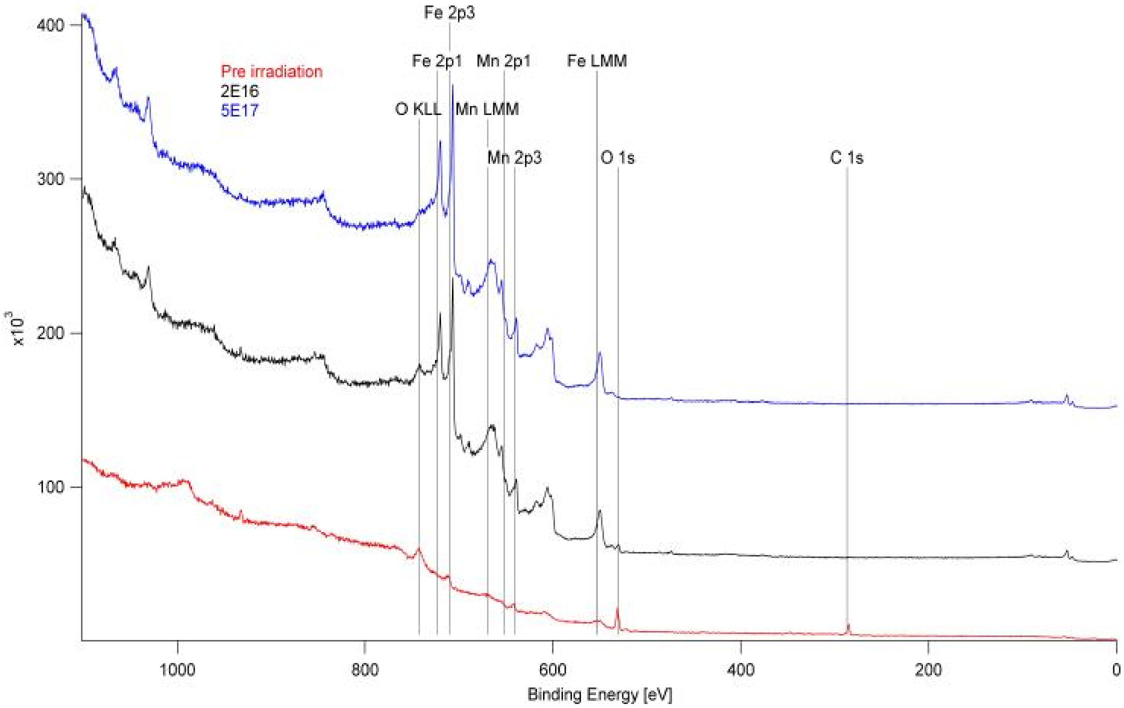

Figure 4.3 XPS results for Fe35Mn irradiated with 750eV Ar$^+$ ions at 60° before irradiation (red), at a fluence of 2E16 cm^{-2} (black), and at a final fluence of 5E17 cm^{-2} (blue).

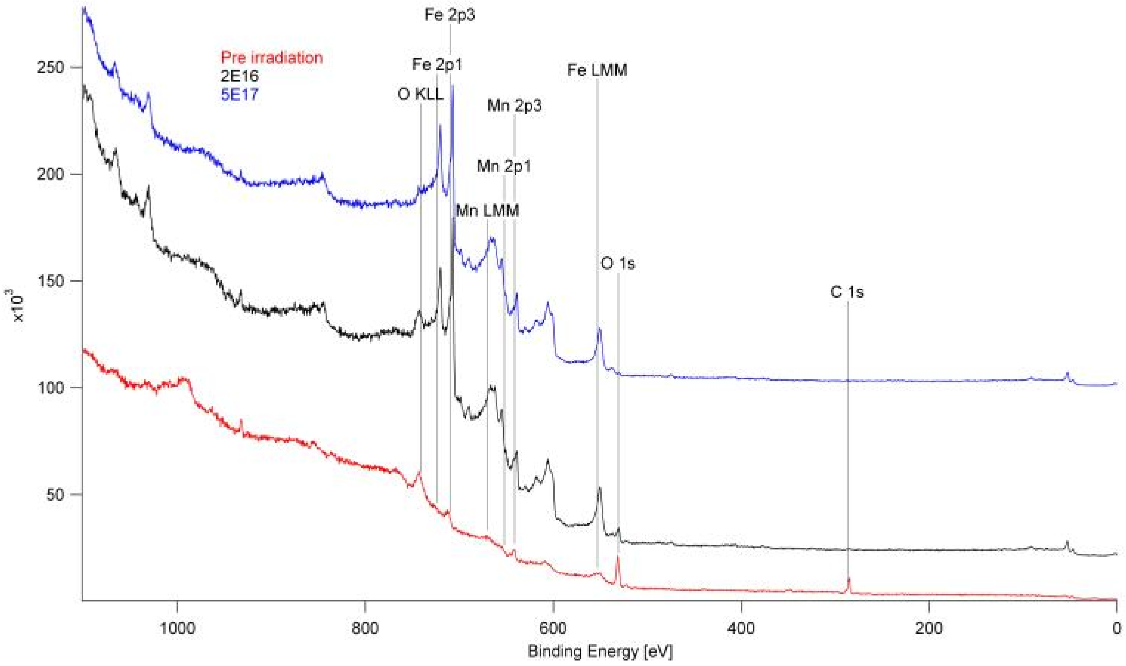

Figure 4.4 XPS results for Fe35Mn irradiated with 1000eV Ar$^+$ ions at 60° before irradiation (red), at a fluence of 2E16 cm^{-2} (black), and at a final fluence of 5E17 cm^{-2} (blue).

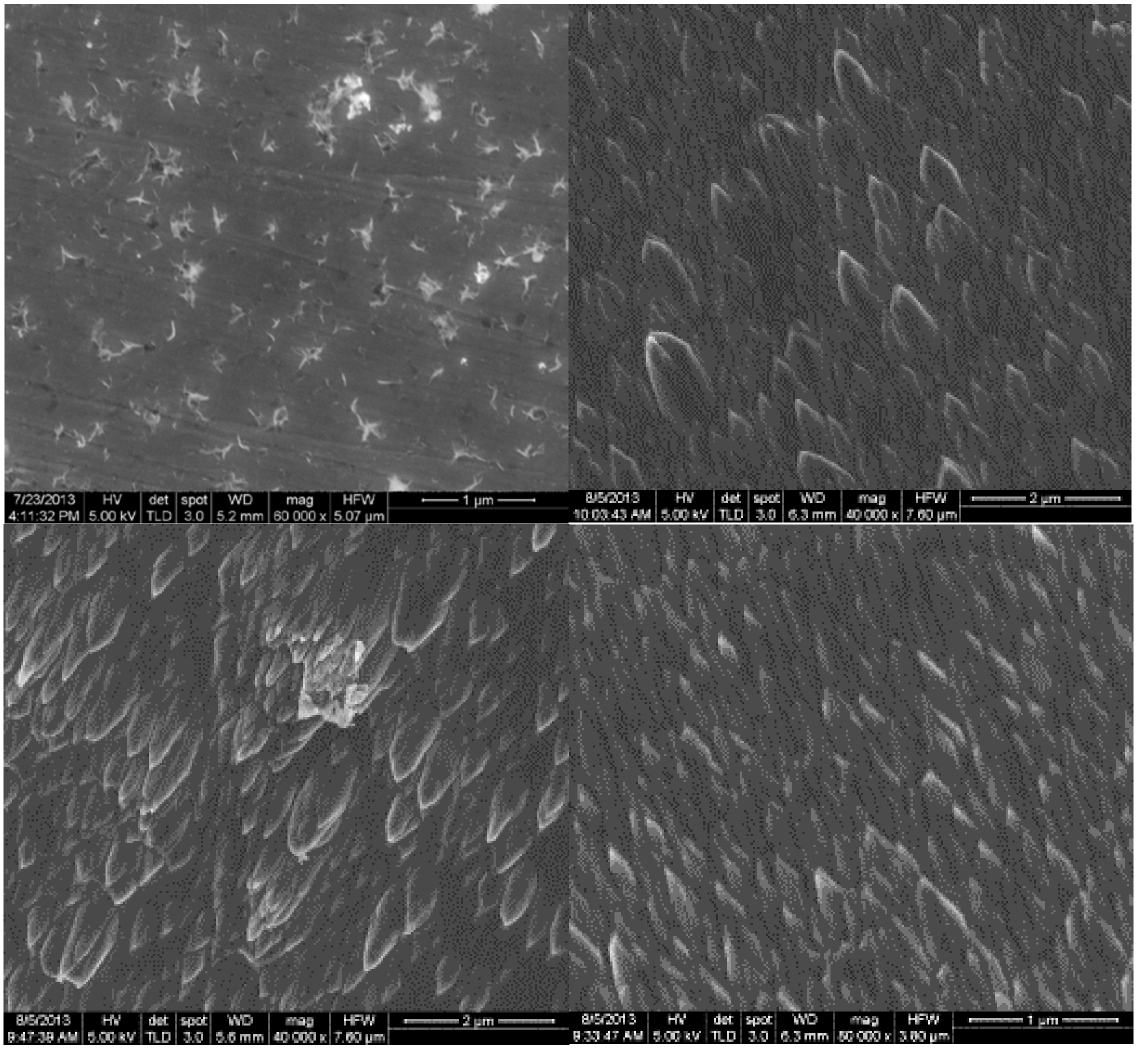

Figure 4.5 SEM images of Fe35Mn samples prior to irradiation (a) and irradiated with Ar^{+} ions at 60 degrees to fluences of 5E17 cm^{-2} at energies of 500eV (b), 750eV (c), and 1000eV (d). Note (a) is at 60,000x, (b) and (c) are at 40,000x, and (d) is at 80,000x.

Irradiation with 1keV Ar^{+} ions resulted in the most homogeneous morphologies, while the lower energies produced structures with large ranges of size.

Table 4.1 Iron content in Fe35Mn surfaces from XPS results in atomic percent. Pre-irradiation composition was 40.57% iron.

Energy	$2x10^{16}$ cm^{-2}	$5x10^{17}$ cm^{-2}
500eV	85.73%	90.42%
750eV	90.69%	91.74%
1000eV	90.17%	91.79%

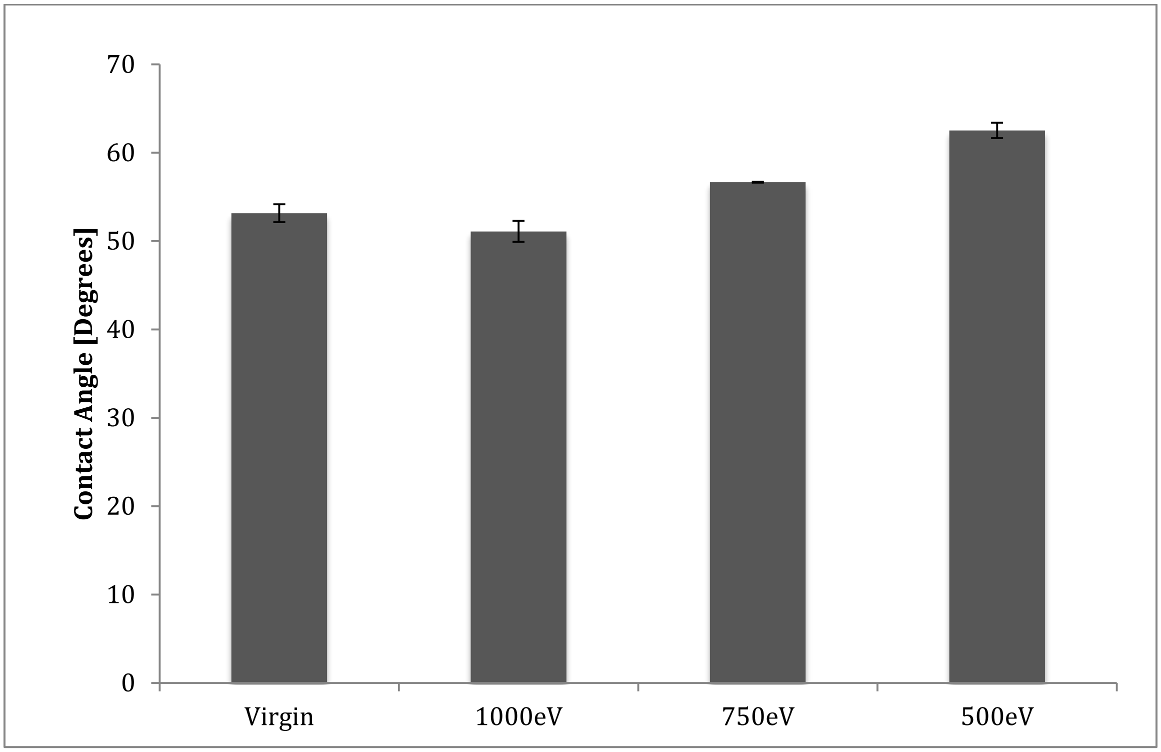

Figure 4.6 Contact angles of FeMn samples after irradiation compared to an unirradiated sample.

The contact angle of the virgin sample was about 52°. After irradiation with 1keV Ar+ ions, the contact angle decreased slightly. The irradiation with the lower energy ions, on the other hand, resulted in an increase in the contact angle, which indicates a decrease in the surface wettability. This is likely due to the increased surface area created by the nanoscale features after irradiation.

4.4 Discussion

Prior to irradiation, the samples were ground to a rough finish of 600 grit. The higher energies resulted in more rapid sputtering of the manganese and oxygen, although the final compositions are statistically the same. Irradiation at all three energies produced nanoscale features on the surfaces. These features vary in size between the different energies of irradiation, as well as across each sample. Irradiation with 1keV Ar^+ ions produced the least variation in feature size, with relatively uniform features about 500nm in length, while the 750eV Ar^+ ions produced the most well-defined structures, varying in length from about 500nm to 2μm. The SEM images reveal structures that appear to be pillar-like, with wide bases and narrow tips inclined at an oblique angle with respect to the surface normal. AFM is necessary in order to further characterize the shape and size of these structures. Irradiation with 1keV Ar^+ ions resulted in a slight increase in wettability of the surface, while the lower energy irradiations decreased the wettability. The larger contact angles observed on the samples irradiated at 500eV and 750eV can be attributed to the increase in surface area.

XPS was performed in situ, giving the compositions of the surfaces induced by irradiation without being exposed to atmosphere. The oxide layer was completely removed after irradiation, while the carbon was removed after a relatively low fluence of $2x10^{16}cm^{-2}$, suggesting the carbon was simply a contaminant on the surface, while the oxide layer was several nanometers thick. The samples were exposed to atmosphere prior to SEM imaging and goniometry analysis, however. Exposure to atmosphere would have resulted in formation of a new oxide layer on the iron surface, which may have affected the contact angle of the samples.

These microscale features have the potential to influence cell adhesion and proliferation, as well as differentiation of stem cells. Nanopits on the surfaces of polymethylmethacrylate surfaces have been shown to have a similar effect on bone mineral formation by mesenchymal stem cells compared with cells treated with osteogenic media [36]. Well-ordered structures had little effect on adhesion and differentiation, while the random structures differentiated into osteoblastic morphologies after 14 days [36]. The less well-ordered structures produced at the lower energies of irradiation may therefore have a positive impact on bone mineralization, although it is unclear how this particular morphology will influence cell behavior compared with the nanopits examined by Dalby et al. [36].The changes in surface wettability may also influence cell behavior on the surface. The wettability of a surface can affect protein adsorption[85-87], which is an important factor in cell adhesion [88].

4.5 Conclusions

Through the use of ion beam irradiation, nanoscale surface features can be created on bulk iron-manganese alloys. Using argon ions at oblique angles of incidence between 500eV and 1keV, blade-like features were produced. The size of the features induced by 500eV and 750eV Ar^+ ions was relatively non-uniform, with features up to 2μm in length and nearly 1μm wide interspersed with features of only about 500nm in length. The 1keV Ar^+ irradiation, by contrast, resulted in a relatively uniform surface, with features on average about 500 nm long and 200nm wide.

CHAPTER 5 EVOLUTION OF SURFACE OXIDE FORMATION ON Fe30Mn AND Ti6Al4V SURFACES THROUGH ACID-PEROXIDE TREATMENT

5.1 Introduction

One of the major concerns in the safety and efficacy of a metallic implant is the potential for stress corrosion cracking (SCC) [89]. Regardless of whether the implant is designed to be permanent or to degrade, SCC can lead to failure of the implant and damage to the surrounding tissue. The formation of corrosion pitting can contribute significantly to the problem of SCC. Pitting typically occurs when the passive film on the surface of a metal has a flaw or inhomogeneity, leading to the formation of a local anode at the site of the defect, as shown in Fig. 5.1a.. The surrounding passive film then becomes a cathode, resulting in localized galvanic corrosion. As the anode corrodes, ions dissolve from the site, forming a small pit filled with the dissolved metal cations (Fig. 5.1b.). Anions, e.g. Cl^-, are attracted by the metal cations into the cavity. This in turn accelerates the localized corrosion, and the pit continues to deepen (Fig. 5.1c.), as the pit acts as a closed corrosion zone [90]. The existence of a deep pit in the surface of a metal can create a large stress concentration, leading to cracking and ultimately fracture and failure [91]. The best way to fight pitting in the surface is therefore to create a homogeneous surface layer, in order to prevent formation of local anodes Human body fluid contains many corrosive ion species, including Cl^- [92]. Stress corrosion cracking therefore is a major factor in the useful lifetime of an implant.

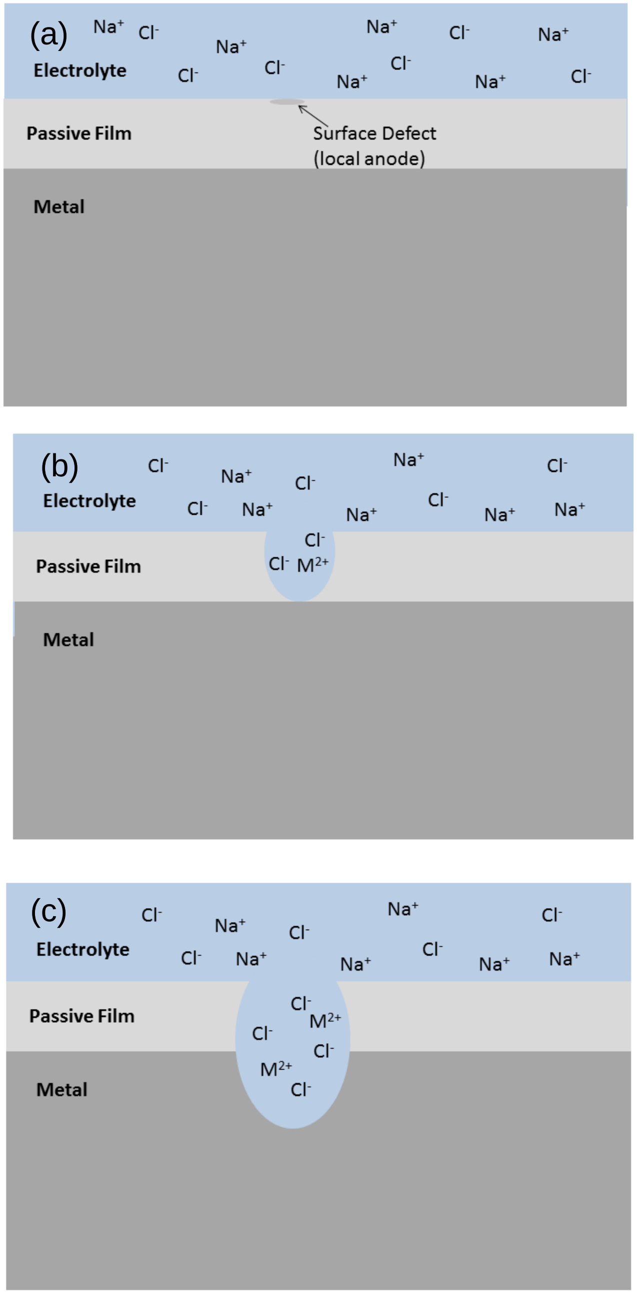

Figure 5.1 Figure 5.1: Formation of corrosion pit in salt solution from surface defect (a), localized breakdown of passive film (b), and propagation of crack (c).

Iron-manganese alloys are intriguing candidates for bioresorbable implant applications, and their degradation behavior must be carefully controlled in order to ensure uniform degradation at a rate that matches the healing of the affected tissue. Iron is low in the galvanic series, and is never found in nature in its metallic state. It is typically found as an oxide, oxhydroxide, or as a compound with elements such as carbon and sulfur [93]. The iron manganese surfaces, therefore, form a native oxide layer upon exposure to atmosphere after casting. This oxide layer provides a passive surface that prevents early degradation of the material upon exposure to corrosive fluids. Previous studies have shown that the early degradation of Fe20Mn surfaces is prevented by this iron-rich oxide layer, with little to no mass loss after 50 days of immersion in osteogenic medium [51].

The formation of a homogeneous surface layer can be formed through various methods, including chemical treatments, heat treatments, ion bombardment, and deposition of a passive film. Chemical treatment is an attractive method due to the availability of various acids and oxidizers, the ability to treat a large surface area in a short time period, and the relatively low cost of treatment. These chemical treatments can also be extended to Ti6Al4V surfaces in order to create rough surfaces that will improve cell adhesion and prevent micro-motion between the implant and the surrounding bone. The following chapter presents a study on the effects of acid-peroxide solutions on the surface chemistry and morphology of resorbable iron manganese surfaces and traditional Ti6Al4V alloy, and how these treatments affect the corrosion behavior of the metals.

5.2 Materials and Methods

5.2.1 Fe30Mn Casting and Machining

Fe30Mn was cast through vacuum induction melting (VIM). Small, irregular pieces of 99.9% pure Fe (Alfa Aesar, Ward Hill, MA) and 99.9% pure Mn (Alfa Aesar, Ward Hill, MA) were weighed out to 30% Mn, balance iron (Fe30Mn).The chamber was evacuated to a pressure of approximately 10^{-3} atm and purged three times with argon to reduce the oxygen content in the furnace. After the final purge, the chamber was back-filled with argon to minimize manganese vaporization. The alloy melted and poured into a cylindrical copper mold resting on a water-cooled copper plate to create an ingot 3.5 inches long with a diameter of 1 inch. The ingot was machined into 9.4 mm diameter discs with a thickness of 1.6 mm. Ti6Al4V rods were machined into the same geometry for comparison. After machining, the discs were ground to a rough finish of 600 grit, and cleaned in acetone. The Fe30Mn was stored in a desiccator to prevent oxidation of the surface.

5.2.2 Chemical Treatments

Prior to chemical treatment, the samples were ultrasonically cleaned with acetone and air dried. The samples were then exposed to 3:1 mixtures of acid:peroxide for time periods of 15 min, 1 hr, and 24hr for each of the three acids chosen. Hydrogen peroxide was chosen as a strong oxidizing agent. Treatment with hydrogen peroxide alone showed very little difference in the surface morphology of the Fe30Mn, so acid was chosen to increase the chemical activity of the solutions. All acids were diluted to 0.1M, and the hydrogen peroxide concentration was 30%. The three acids used were nitric (HNO_3), sulfuric (H_2SO_4), and phosphoric (H_3PO_4). The purpose behind using three different acids was to attempt to create different oxidation states on the metal surfaces. After exposure, the samples were triple rinsed in deionized water and air dried.

Sulfuric acid mixed with hydrogen peroxide creates a volatile solution that can "eat through" organic matter, giving it the colloquial name "piranha solution." The mixture undergoes the following reactions:

$$H_2SO_4 \rightarrow H_2SO_5 + H_2O$$ Equation 5-1

$$H_2SO_4 \rightarrow H_3O^+ + H_2SO_4^- + O$$ Equation 5-2

The first reaction results in the formation of Caro's Acid (H_2SO_5), one of the strongest oxidizers known. The second reaction results in the formation of reactive elemental oxygen. This oxygen can react with the sample being treated or combine to create oxygen gas, causing the solution to bubble as it reacts. One possible reaction product of iron immersed in this solution is ferrous sulfate, which is formed in the following reaction:

$$H_2SO_4 + Fe \rightarrow FeSO_4 + H_2$$ Equation 5-3

This reaction is commonly used to finish steels prior to plating.

Nitric acid and hydrogen peroxide solutions are commonly used in order to extract certain elements from soil. The addition of the nitric acid to the hydrogen peroxide increases the oxidation potential of the solution, accelerating the reaction:

$$2H_2O_2 \rightarrow 2H_2O + O_2 \qquad \text{Equation 5-4}$$

Phosphoric acid mixed with hydrogen peroxide is a common etchant for aluminum and certain semiconductors.

5.2.3 Characterization

Sample morphology was assessed with scanning electron microscopy (SEM). Surface composition was examined through energy dispersive x-ray spectroscopy (EDS). X-ray diffraction (XRD) was performed on a Bruker 8 with a GADDS area detector and a Cu Kα source in order to assess changes in the surface crystal structure and composition. The Ti6Al4V patterns were indexed based upon the literature [94]. The corrosion resistance of each treated sample was measured through linear polarization experiments in phosphate buffered saline (PBS) with a pH of 7.4 (to mimic the ion activity of blood), using a platinum counter electrode.

5.3 Results

As a preliminary test, the FeMn samples were immersed in 30% H_2O_2 solution for 15 minutes, 1 hour, and 24 hours. The hydrogen peroxide treatment resulted only in pitting of the FeMn surface, and the solution remained transparent and colorless. No oxide formation was visible.

Immersion of the Ti6Al4V in all cases resulted in a slightly yellow, translucent solution with no visible precipitation. In the case of the iron manganese immersion, a thick black precipitate formed in the the phosphoric acid-hydrogen peroxide solution after 24 hours. The sulfuric acid-hydrogen peroxide immersion likewise resulted in precipitate formation, in this case a light-reddish brown color. The nitric acid solution, on the other hand, remained transparent but turned a vibrant red.

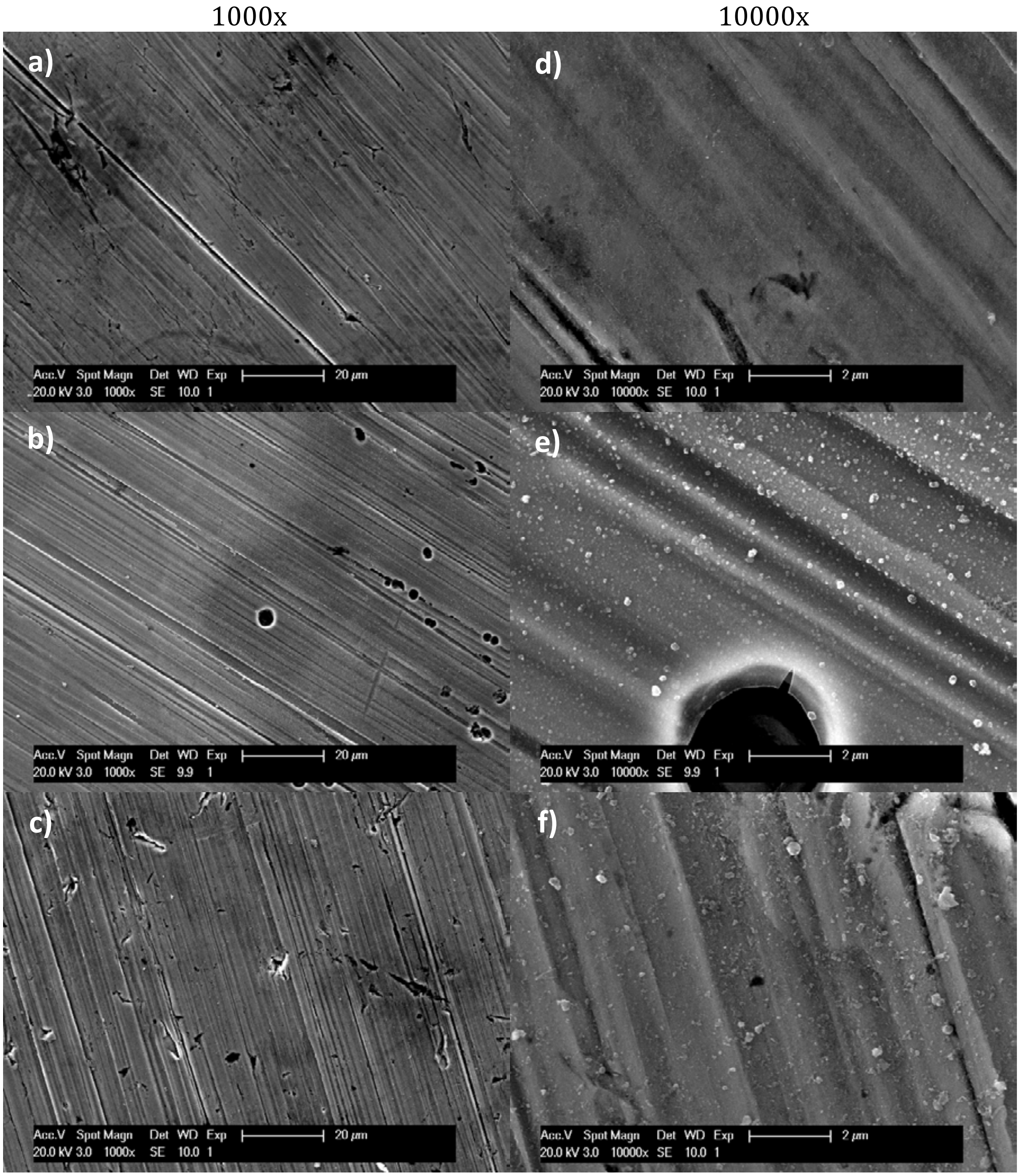

Figure 5.2 : Secondary electron images of hydrogen peroxide treated Fe30Mn after 15 min (a,b), 1 hour (c,d), and 24 hours (c,f). Pitting is visible after 1 hour.

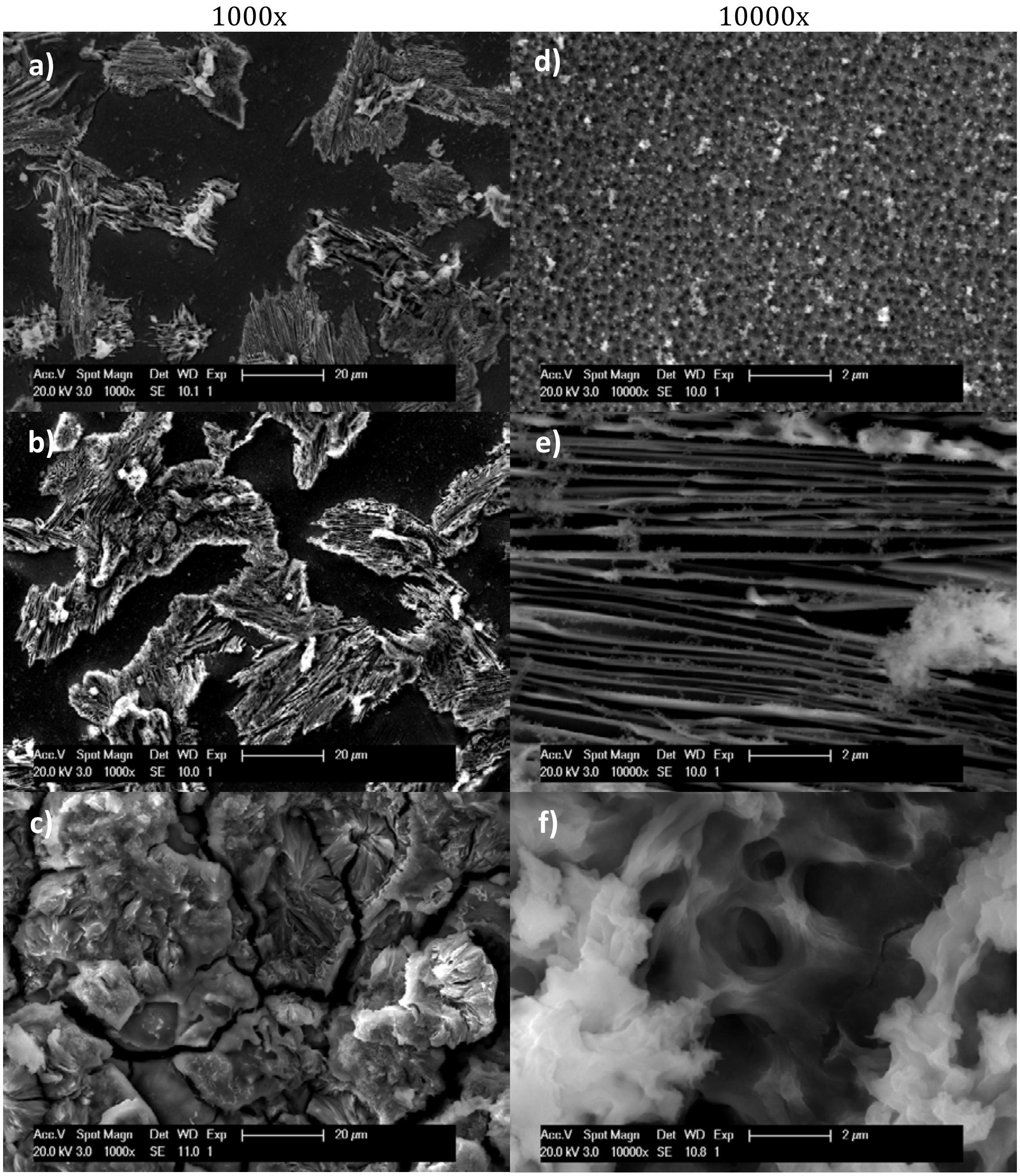

Figure 5.3 : Secondary electron images at 1000x (a-c) and 10000x (d-f) of phosphoric acid and hydrogen peroxide treated Fe30Mn after 15 min (a,b), 1 hour (c,d) and 24 hours (e,f).

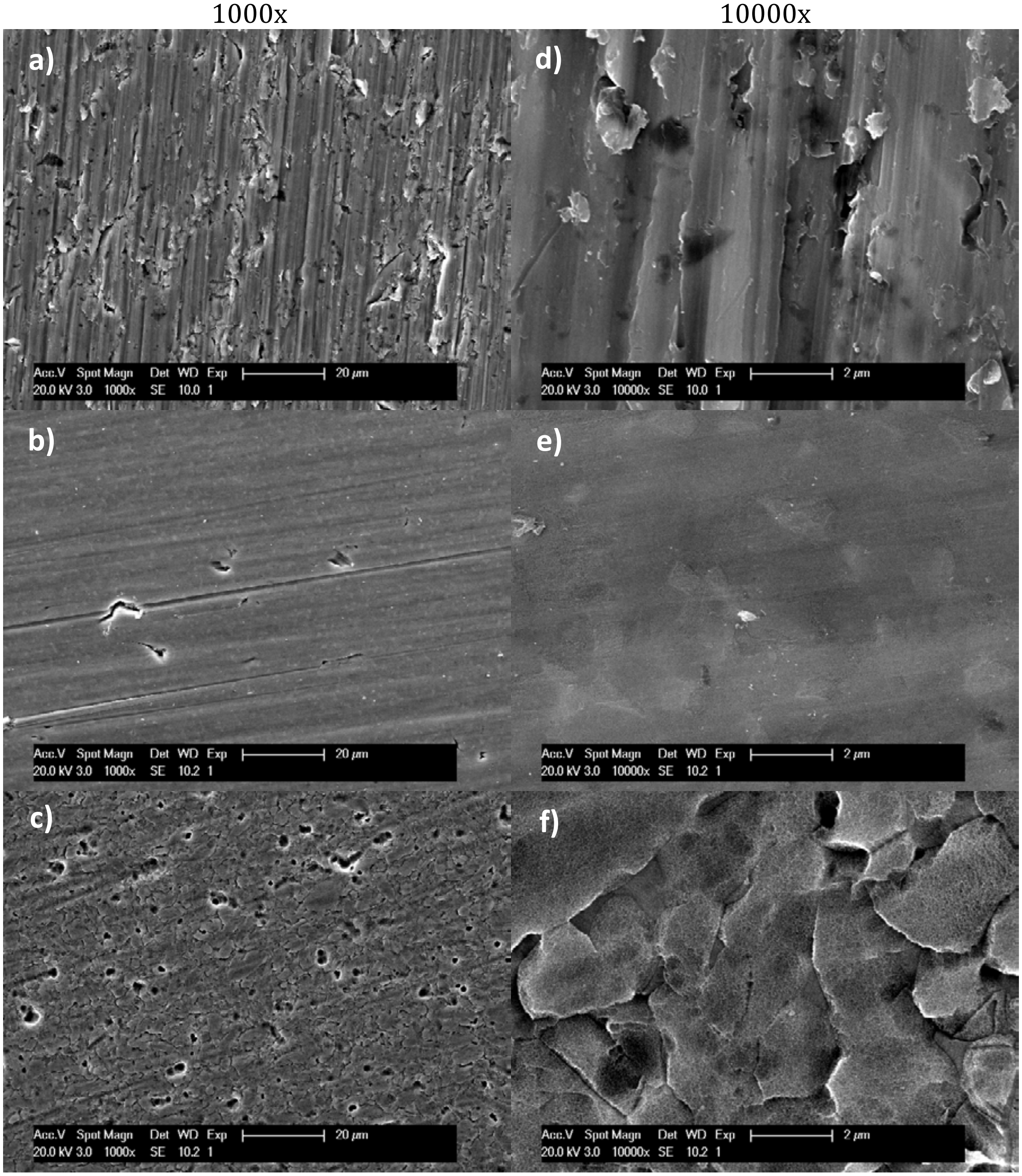

Figure 5.4 Secondary electron images at 1000x (a-c) and 10000x (d-f) of phosphoric acid and hydrogen peroxide treated Ti6Al4V after 15 min (a,d), 1 hour (b,e) and 24 hours (c,f).

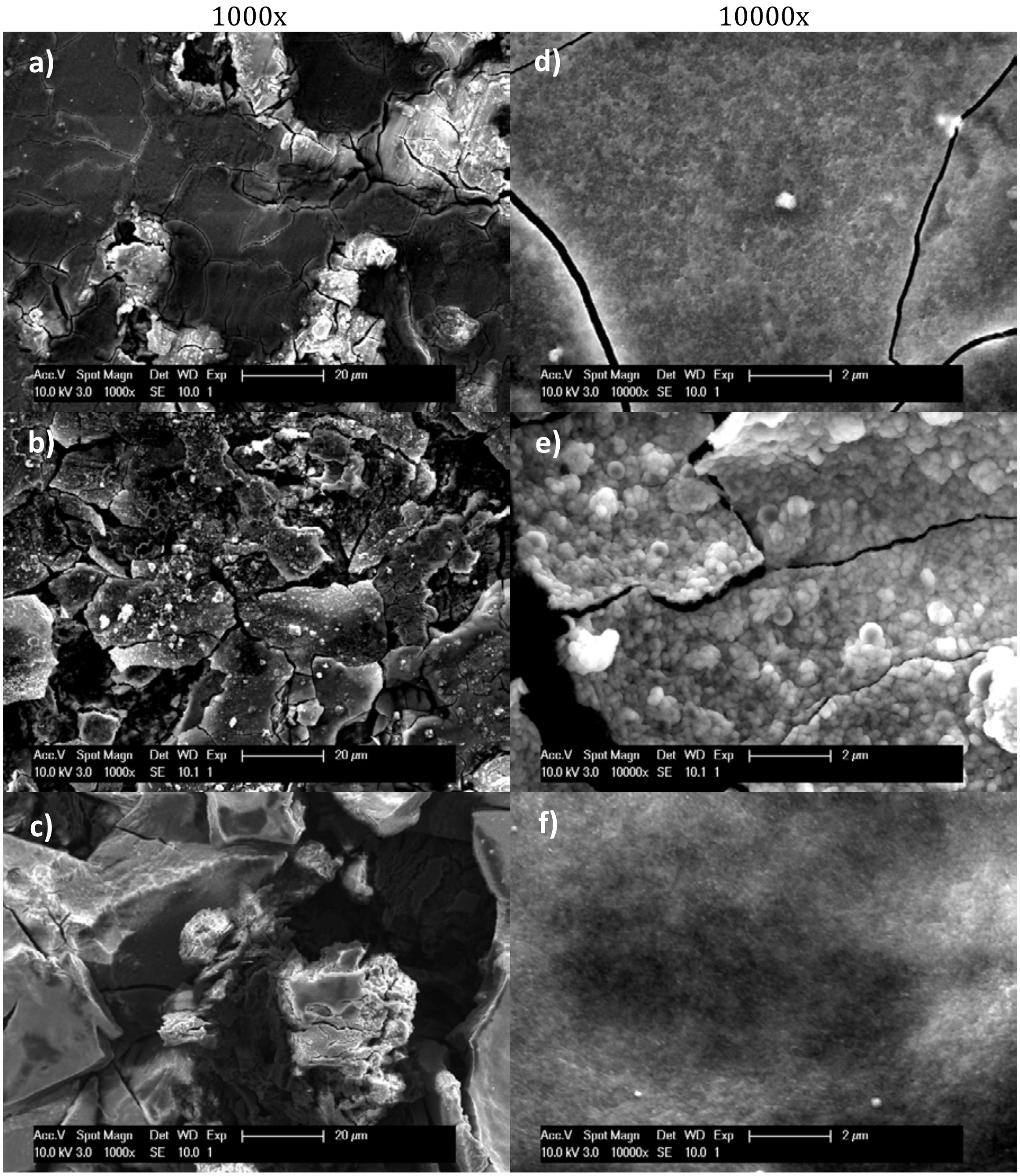

Figure 5.5 Secondary electron images at 1000x (a-c) and 10000x (d-f) of nitric acid and hydrogen peroxide treated Fe30Mn after 15 min (a,d), 1 hour (b, e), and 24 hours (c,f).

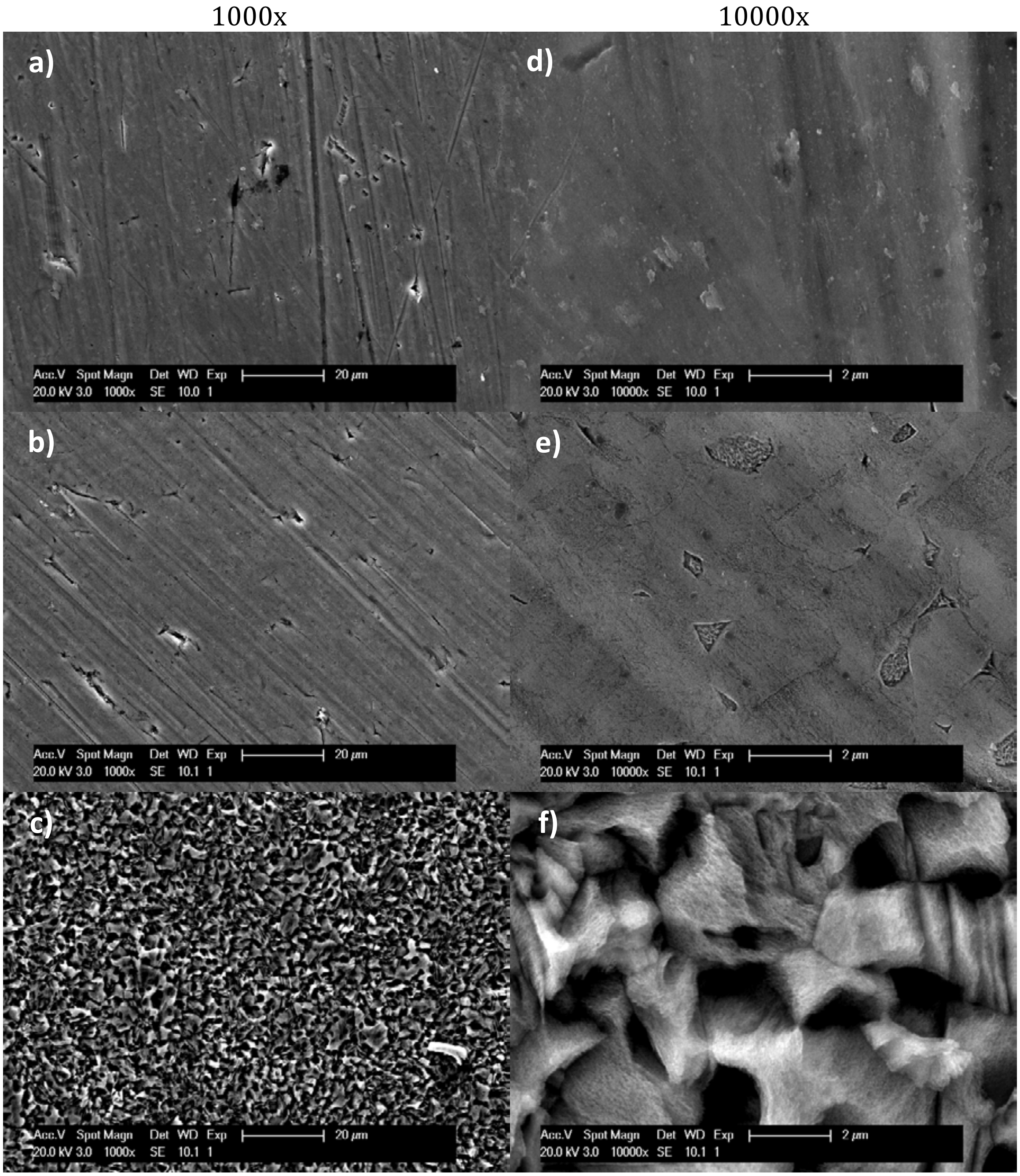

Figure 5.6 : Secondary electron images at 1000x (a-c) and 10000x (d-f) of nitric acid and hydrogen peroxide treated Ti6Al4V (d-f) after 15 min (a,d), 1 hour (b, e), and 24 hours (c,f).

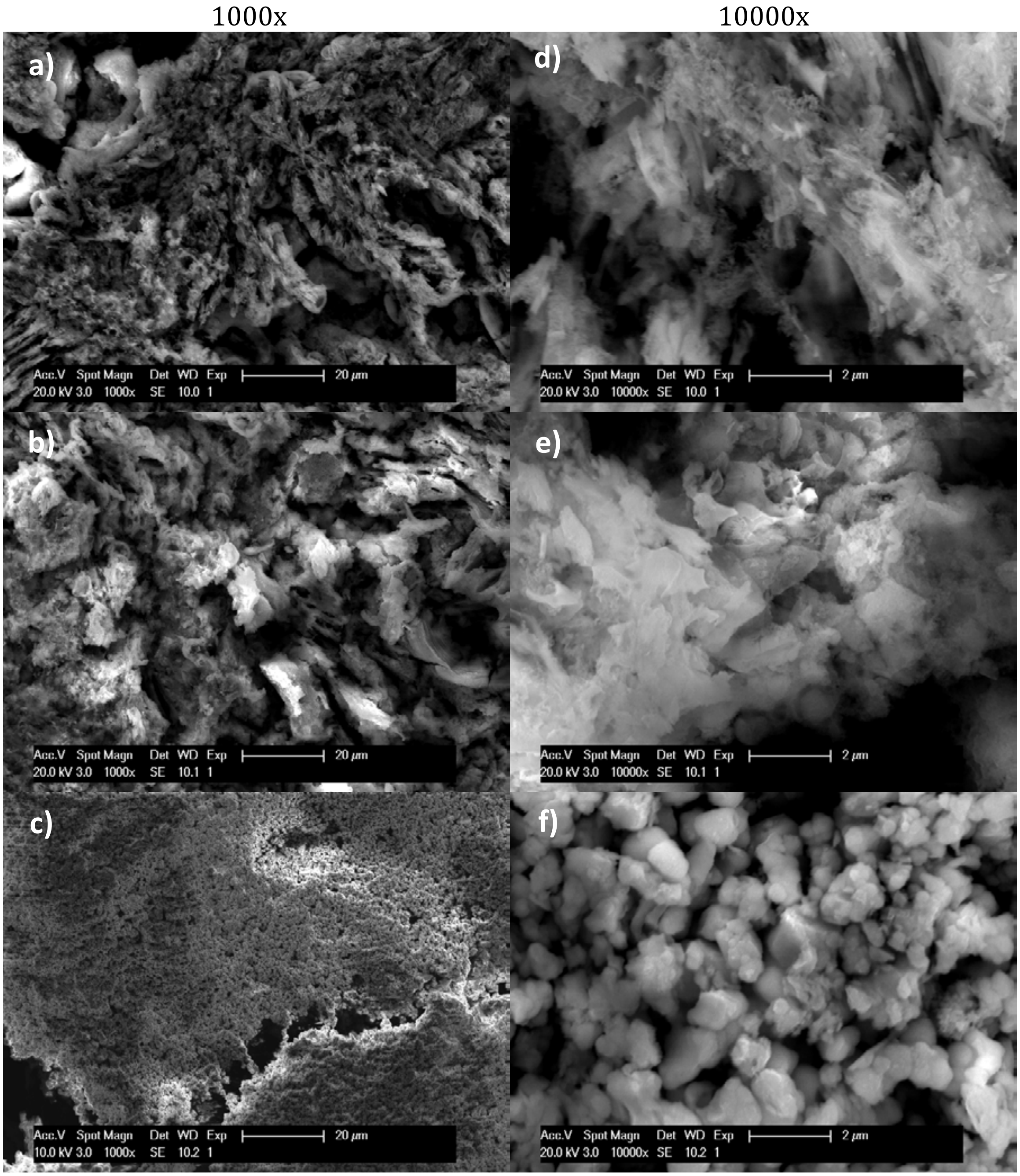

Figure 5.7 : Secondary electron images at 1000x (a-c) and 10000x (d-f) of sulfuric acid and hydrogen peroxide treated Fe30Mn after 15 min (a), 1 hour (b), and 24 hours (c).

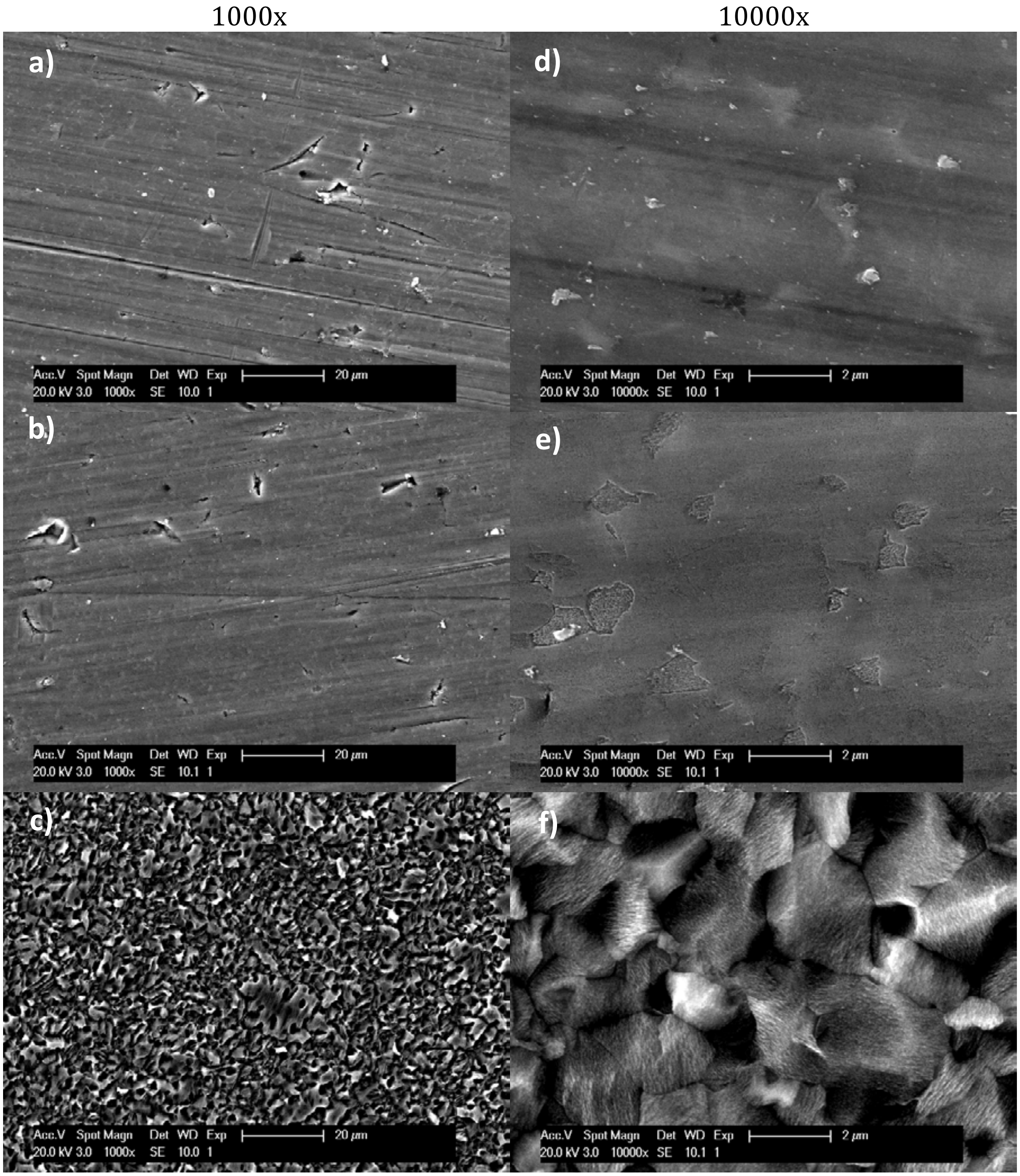

Figure 5.8 Secondary electron images at 1000x (a-c) and 10000x (d-f) of sulfuric acid and hydrogen peroxide treated Ti6Al4V after 15 min (a), 1 hour (b), and 24 hours (c).

Table 5.1 EDS Results for Sulfuric Acid and Hydrogen Peroxide Treatment of FeMn (atomic %)

Time	C	O	Si	Mn	Fe	S
15 min	0	27.31	4.14	14.04	49.53	4.98
1 hour	0	29.14	4.22	10.21	49.08	7.34
24 hours	30.49	32.38	0.72	1.93	28.17	6.31

Table 5.2 EDS Results for Nitric Acid and Hydrogen Peroxide Treatment of FeMn (atomic %)

Time	C	O	Si	Mn	Fe	F
15 min	0	20.97	6.74	18.69	53.60	0
1 hour	24.85	16.22	6.31	13.08	34.86	4.61
24 hours	0	31.65	5.42	3.08	59.84	0

Table 5.3 EDS Results for Phosphoric Acid and Hydrogen Peroxide Treatment of FeMn(atomic %)

Time	C	O	Si	Mn	Fe	P
15 min	33.01	4.56	1.45	18.34	41.43	1.20
1 hour	0	0	3.19	28.88	65.07	2.86
24 hours	28.62	25.10	0	4.71	21.19	20.38

Carbon is present on 4 of the 9 samples tested. However, the solutions used contained no more than trace amounts of carbon. Silicon was also detected in all but one of the iron manganese samples. The presence of these two components may be due to silicon carbide from the grinding paper becoming embedded in the surface. This explanation does not account for the fact that very high concentrations of carbon were found in the 4 samples where carbon was present (25% or greater), while none was found in others. The silicon concentrations, on the other hand, are relatively low, under 7% in all cases. It is therefore more likely that the samples were contaminated during handling prior to EDS quantification. Carbon tape was used to adhere the samples to the SEM stubs and may contribute to the carbon contamination.

Table 5.4 EDS Results for Sulfuric Acid and Hydrogen Peroxide Treatment of Ti6Al4V (atomic %)

Time	Ti	Al	V
15 min	85.81	12.51	1.68
1 hour	88.30	10.58	1.13
24 hours	87.38	11.11	1.51

Table 5.5 EDS Results for Nitric Acid and Hydrogen Peroxide Treatment of Ti6Al4V (atomic %)

Time	Ti	Al	V
15 min	86.04	11.79	2.17
1 hour	85.67	11.98	2.36
24 hours	86.33	11.56	2.11

Table 5.6 EDS Results for Phosphoric Acid and Hydrogen Peroxide Treatment of Ti6Al4V (atomic %)

Time	Ti	Al	V	Si
15 min	81.29	7.46	2.45	2.80
1 hour	85.25	12.29	2.46	0
24 hours	85.56	11.99	2.45	0

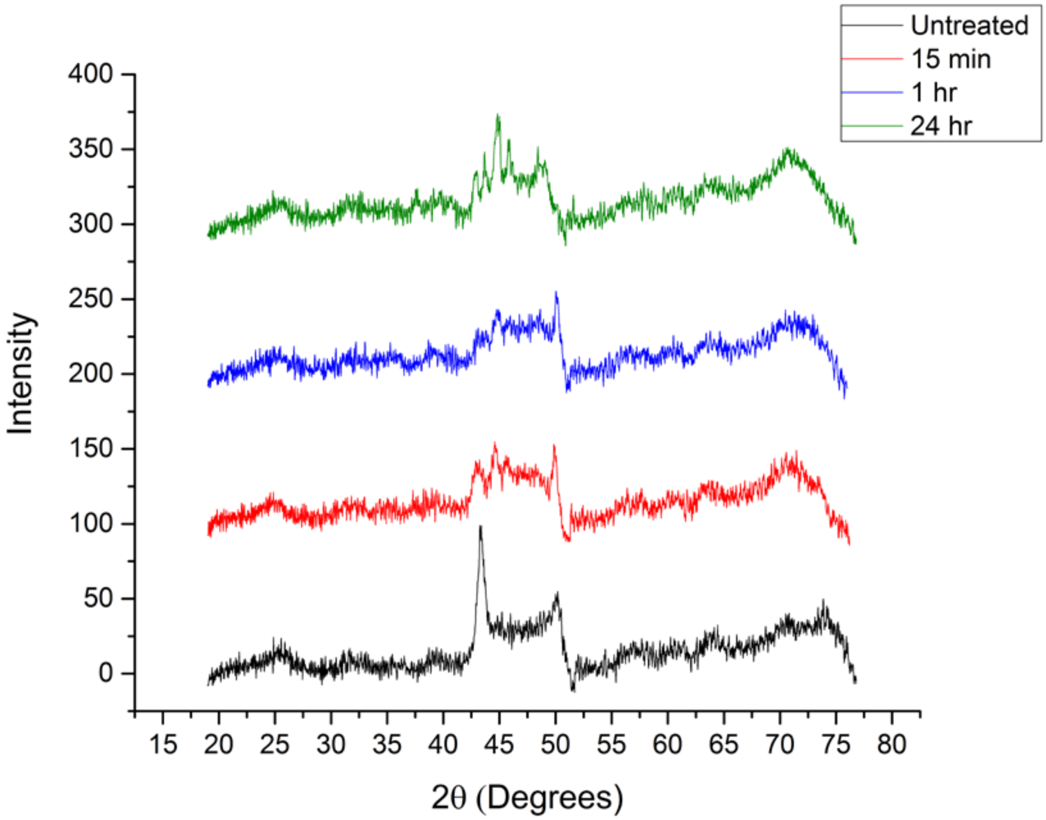

Figure 5.9 XRD patterns of FeMn surfaces treated with hydrogen peroxide and sulfuric acid after 15 min (red), 1 hour (blue), and 24 hours (green). The untreated surface is shown in black

Prior to treatment, the only peaks visible in the FeMn patterns are those corresponding to the austenite phase. The composition of the alloy was 30 wt % manganese, which is sufficient to stabilize the austenite. Peaks corresponding to other phases are not visible in the patterns, however the FeMn patterns have a relatively low signal-to-noise ratio compared with the Ti6Al4V patterns. Cu Kα x-rays induce fluorescence in iron atoms, hence the relatively low signal to noise ratio, compared with the titanium patterns shown in Figures 5.9-5.11. At the time of this experiment, access to a functioning Co source was not available and the XRD source used for this analysis was not outfitted with a filter to minimize the signal from the fluorescence. In the case of the FeMn samples treated with sulfuric acid, several new peaks are visible between 40° and 50° after 24 hours. These peaks correspond well with those of goethite, α-FeOOH.

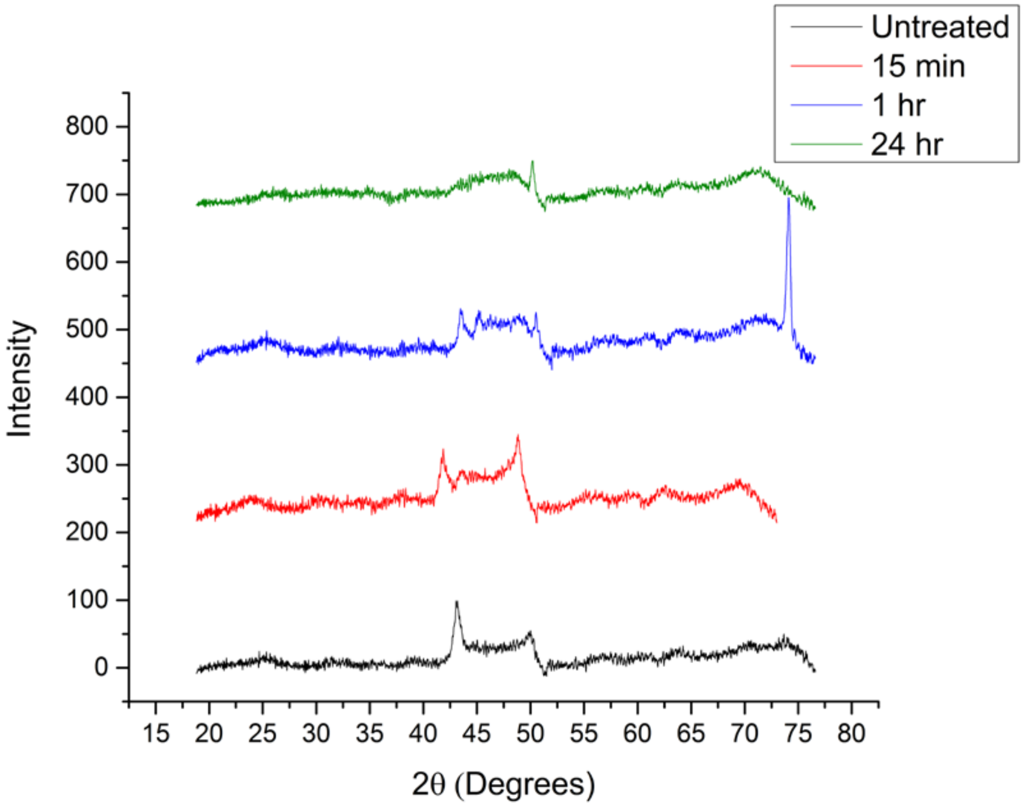

Figure 5.10 XRD patterns of FeMn surfaces treated with hydrogen peroxide and phosphoric acid after 15 min (red), 1 hour (blue), and 24 hours (green). The untreated surface is shown in black

After 15 minutes in phosphoric acid and peroxide, the relative intensities of the austenite peaks change slightly, with the peak at 49° increasing in intensity with respect to the peak at 43°. New peaks begin to emerge at 44° after 15 minutes, but disappear after 24 hours, leaving a broad, wide peak between 40° and 48°, suggesting an amorphous layer at the surface. A tall, sharp peak is visible at 74.5°, but is not present in any of the other patterns.

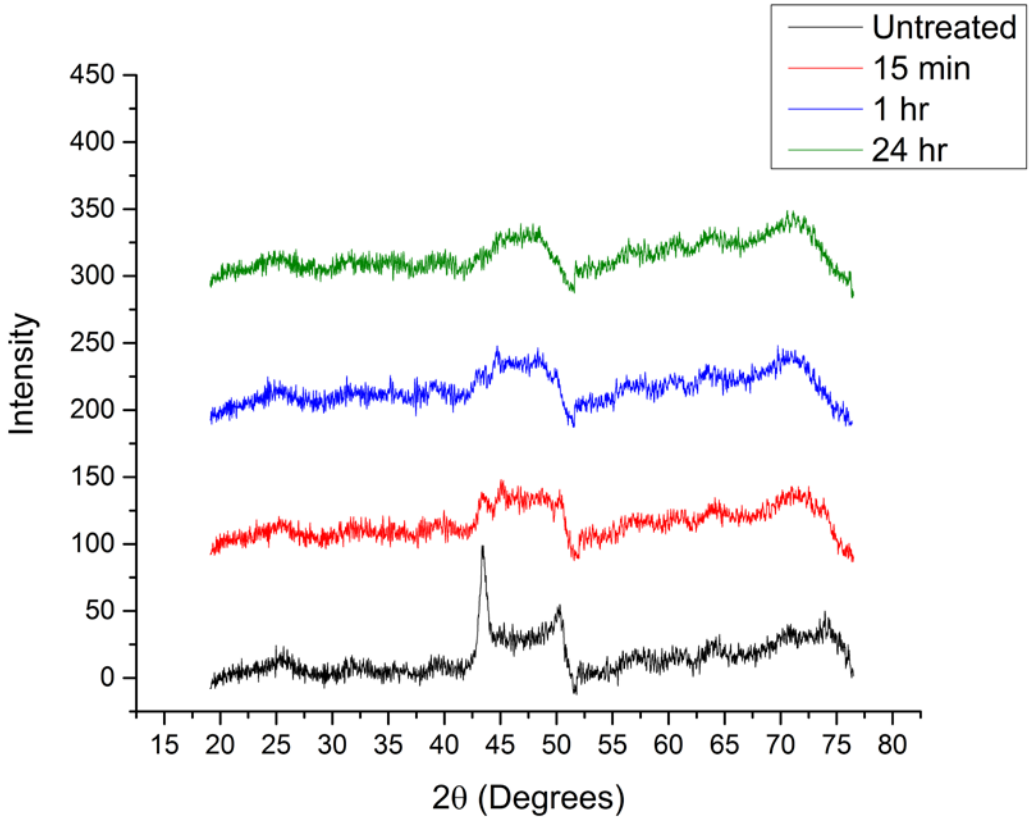

Figure 5.11 XRD patterns of FeMn surfaces treated with hydrogen peroxide and nitric acid after 15 min (red), 1 hour (blue), and 24 hours (green). The untreated surface is shown in black.

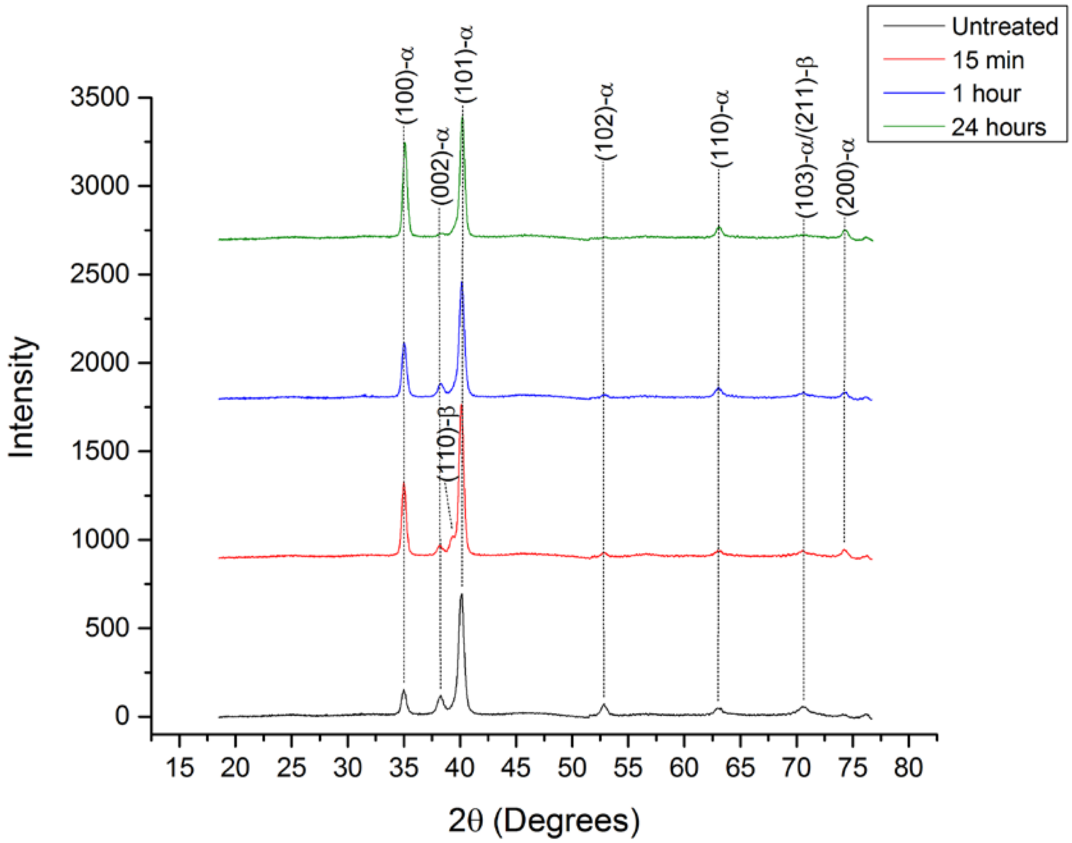

Figure 5.12 XRD patterns of Ti6Al4V surfaces treated with hydrogen peroxide and sulfuric acid after 15 min (red), 1 hour (blue) and 24 hours (green). The untreated surface is shown in black

In the case of Ti6Al4V, after treatment with sulfuric acid and hydrogen peroxide, the (002)-α, (102)-α, and (103)-α/(211)-β peaks become weaker until they are no longer visible in the pattern after 24 hours. The intensity of the first (100) peak, on the other hand, increases significantly. A new β-phase peak is visible after 15 minutes, but does not appear in any of the other patterns. It is possible that this particular specimen had significantly more β-phase present than the other samples.

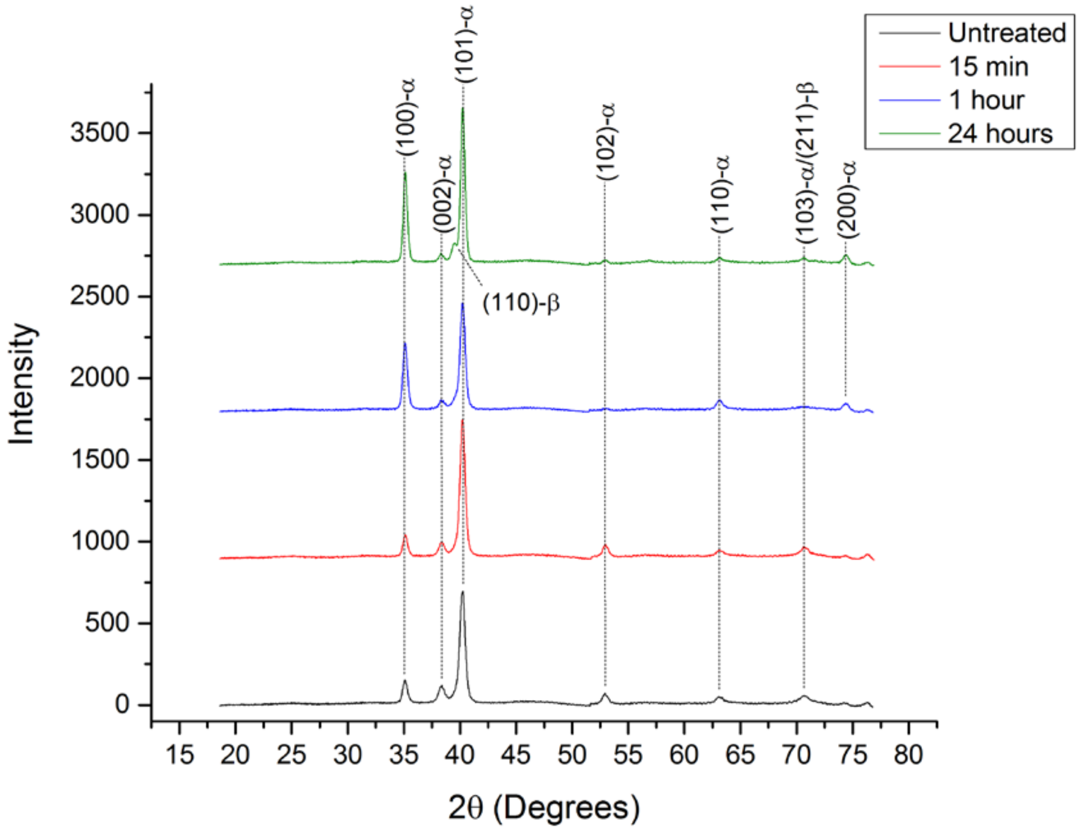

Figure 5.13 XRD patterns of Ti6Al4V surfaces treated with hydrogen peroxide and phosphoric acid after 15 min (red), 1 hour (blue) and 24 hours (green). The untreated surface is shown in black

The intensity of these same peaks in the phosphoric acid-treated Ti6Al4V samples likewise decreased after 24 hours, the intensity of the first (100) peak increased, and a new peak is visible at 39.45°, representing the (002) reflection of the β phase. Again, this peak is not visible in any of the other samples treated with phosphoric acid Similarly, the intensity of the (002), (102), and (110)-α peaks diminished after nitric acid-hydrogen peroxide treatment, but did not completely disappear after 24 hours.

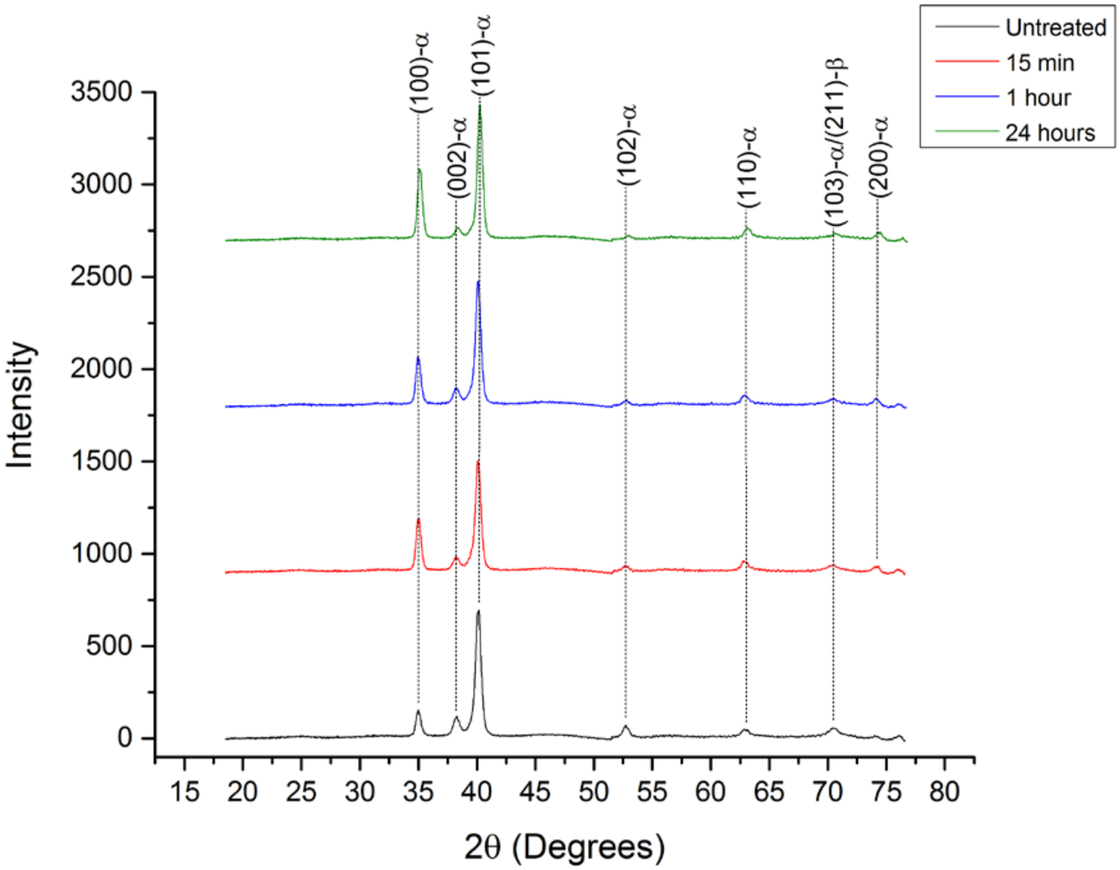

Figure 5.14 XRD patterns of Ti6Al4V surfaces treated with hydrogen peroxide and nitric acid after 15 min (red), 1 hour (blue) and 24 hours (green). The untreated surface is shown in black

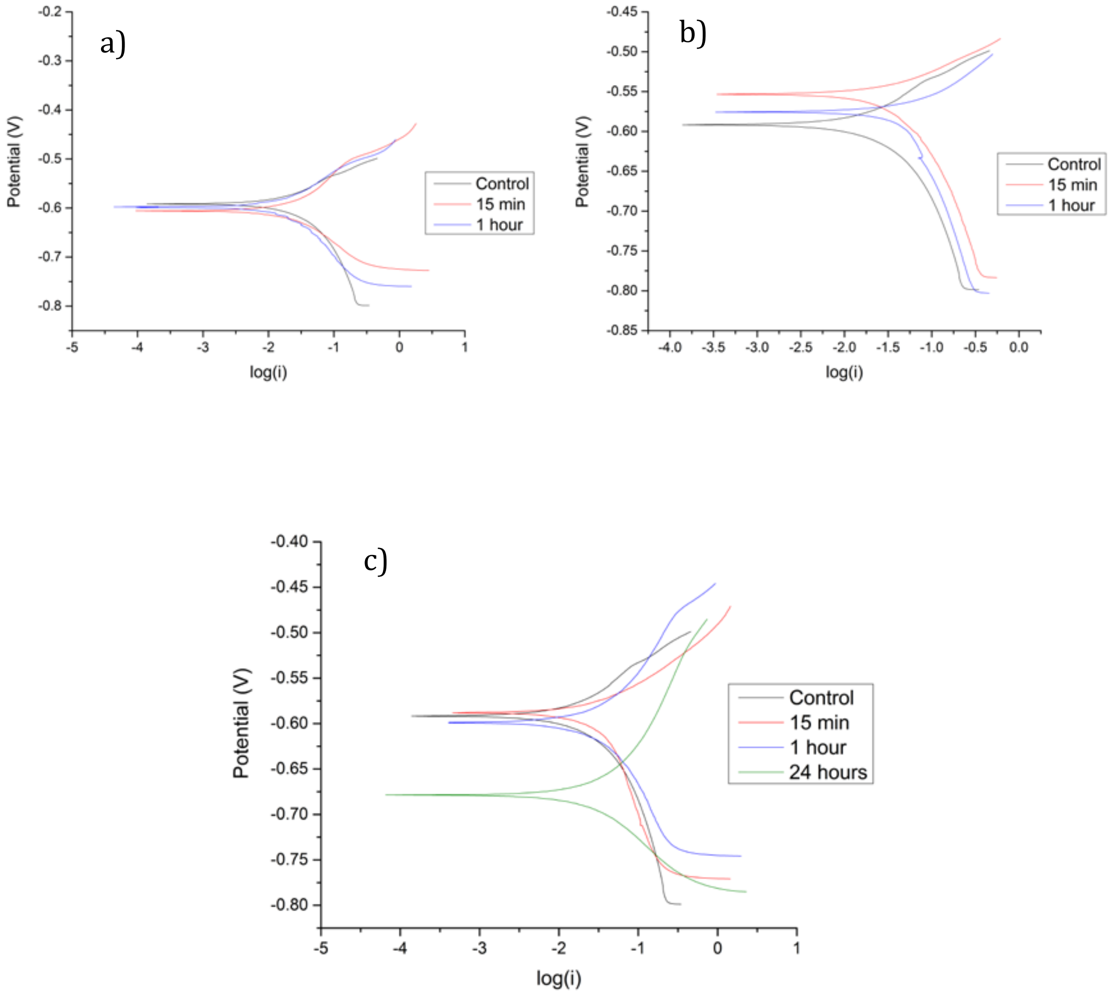

Figure 5.15 Linear polarization results for FeMn samples in phosphate buffered saline at 37°C after treatment with hydrogen peroxide and (a) nitric acid, (b) phosphoric acid, and (c) sulfuric acid. The unmodified sample is shown in each plot in black, and samples treated for 15 minutes, 1 hour, and 24 hours are shown in red, blue, and green, respectively.

Treatment in nitritc acid and hydrogen peroxide had very little effect on the open circuit potential of the FeMn surfaces after treatment for 15 min and 1 hour. Phosphoric acid and hydrogen peroxide treatment resulted in an increase in the open circuit potential, while treatment in sulfuric acid decreased the open circuit potential. This is particularly evident in the sample treated for 24 hours.

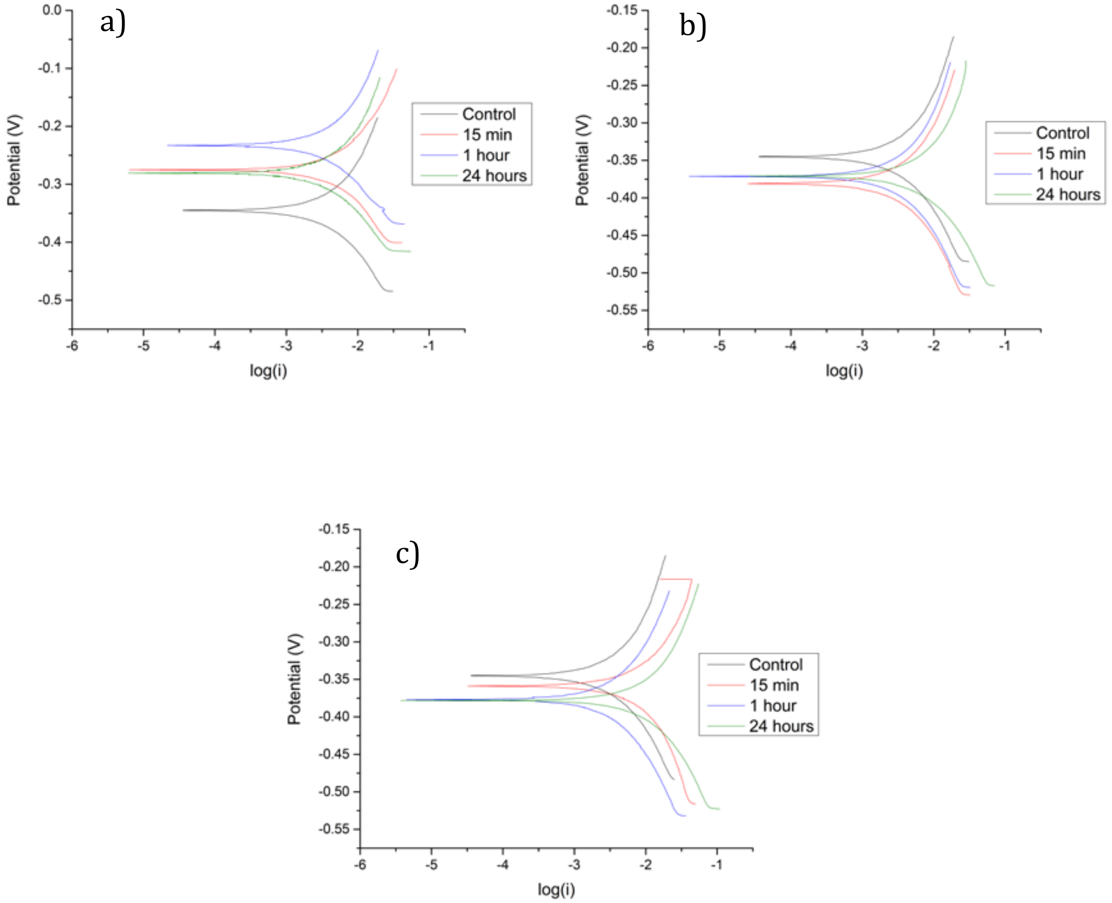

Figure 5.16 Linear polarization results for Ti6Al4V samples in phosphate buffered saline at 37°C after treatment with hydrogen peroxide and (a) nitric acid, (b) phosphoric acid, and (c) sulfuric acid. The unmodified sample is shown in each plot in black, and samples treated for 15 minutes, 1 hour, and 24 hours are shown in red, blue, and green, respectively.

Table 5.7 Corrosion rates of FeMn samples in phosphate buffered saline at 37°C.

Sample	E_{corr} (mV)	i_{corr} (A/cm^2)	Average CR (mm/yr)
Cast FeMn	-591.418	10.083	0.1285
15 min HNO_3	-605.813	20.53	0.2616
1 hr HNO_3	-597.84	8.815	0.1123
15 min H_3PO_4	-533.242	36.78	0.4687
1 hr H_3PO_4	-575.682	65.207	0.8309
15 min H_2SO_4	-587.932	34.671	0.4418
1 hr H_2SO_4	-598.973	42.478	0.5413
24 hrs H_2SO_4	-678.587	46.819	0.5966

The as-cast structure featured a corrosion rate of 0.1285 mm/yr. In all treated samples with the exception of nitric acid after 1 hour, this corrosion rate increased significantly. It was not possible to test the sample treated in phosphoric acid after 24 hours due to its significant mass loss and extremely brittle nature.

Table 5.8 Corrosion rates of Ti6Al4V samples in phosphate buffered saline at 37°C

Sample	E_{corr} (mV)	i_{corr} (A/cm^2)	Average CR (mm/yr)
As manufactured Ti6Al4V	-345.168	4.47	0.0305
15 min HNO_3	-275.046	4.701	0.0320
1 hr HNO_3	-233.279	2.967	0.0202
24 hrs HNO_3	-280.754	3.81	0.0260
15 min H_3PO_4	-380.746	4.618	0.0315
1 hr H_3PO_4	-371.235	4.386	0.0299
24 hrs H_3PO_4	-370.839	8.852	0.0603
15 min H_2SO_4	-358.877	11.191	0.0763
1 hr H_2SO_4	-376.933	4.701	0.0300
24 hrs H_2SO_4	-378.121	12.891	0.0878

5.4 Discussion

Hydrogen peroxide treatment without the aid of an acid results in very little change in the overall surface morphology, with the exception of pit formation, as shown in Figure 5.3. It was necessary to add acid to the solution in order to etch the surface, while simultaneously oxidizing with hydrogen peroxide in order to oxidize the FeMn surfaces.

5.4.1 Oxide Composition and Morphology

After immersion in the acid-hydrogen peroxide solutions, the iron manganese samples react immediately. As shown in Figure 5.4, the phosphoric acid solution begins to etch the surface after 15 minutes, preferentially attacking the inner dendritic liquid. The higher magnification images of the inner dendritic liquid reveal the formation of very small pores. The surface morphology is similar after 1 hour. However, after 24 hours, the entire surface suffers chemical attack. The pores have increased in diameter by an order of magnitude and become interconnected. After treatment with phosphoric acid and hydrogen peroxide, a black oxide forms on the surface of the Fe30Mn. After 24 hours, the phosphoric acid-hydrogen peroxide solution in which the FeMn sample was immersed became a thick black sludge. The black color and low solubility of the oxide suggests it is primarily composed of iron (II,III) oxide (Fe_3O_4) or iron(II) oxide (FeO). After 24 hours in the solution, the Fe30Mn disc experienced significant mass loss and became extremely brittle and difficult to handle. Further testing was not done on this sample. The Ti6Al4V sample, on the other hand, held up well to the phosphoric acid-hydrogen peroxide treatment. The phosphoric acid-hydrogen peroxide solution used to treat the Ti6Al4V samples turned slightly yellow, but remained transparent. No difference between the initial sample and the treated samples was visible with the eye, however, SEM images revealed significant etching of the grain boundaries and pitting after 24 hours in solution. Initial immersion resulted in significant attack of the surface, while the sample removed from solution after 1 hour shows a much smoother surface. Possible reasons for this difference could be a difference in the initial surface condition of the two samples (the 15 min sample may have been rougher initially), or a smoothing effect could take place beyond 15 minutes of immersion. It is most likely that this difference is caused by a rougher sample being used for the 15 minute time point. The roughness of this surface likely resulted in localized corrosion, thus resulting in the more degraded appearance of this sample.

The nitric acid-hydrogen peroxide solution treatment of the Fe30Mn resulted in a cracked oxide formation within 15 minutes of immersion. This oxide became flaky after 1 hour. After 24 hours, the solution in which the iron samples were immersed turned a bright red color, but remained clear. This color is indicative of iron (III) oxide (Fe_2O_3), which is soluble in dilute acid solutions.

After treatment with piranha solution, the iron manganese surface again begins to degrade after just 15 minutes. In contrast with the nitric acid-hydrogen peroxide solution, the surface appears relatively uniform, and no cracking of the oxides was observed until 24 hours. After 24 hours, a light brown precipitate forms in the piranha solution used to treat the iron manganese. This color is indicative of FeOOH. After 24 hours, the new peaks visible in the XRD pattern correspond with α-FeOOH, and the surface morphology is similar to natural goethite observed by Webster et al. [95]. The Ti6Al4V sample appears much the same after initial immersion, however it can be seen after 1 hour that certain grains have begun to degrade. After 24 hours, the surface appears rough and porous from chemical attack, although no difference was observed in the samples with the naked eye.

While the phosphoric acid-hydrogen peroxide solution appears to attack grain boundaries, it appears that the nitric acid and sulfuric acid mixed with hydrogen peroxide preferentially attack certain grains. The (211) peak due to the β-phase diminishes significantly after treatment in sulfuric acid and peroxide, almost completely disappearing after 24 hours, as shown in Figure 5.12. The (002) peak of the α-phase likewise nearly disappears after 24 hours. The (002) is a basal plane in hcp titanium, with a close-packed structure. The higher etching rate of the (002)-α orientation versus the (100)-α orientation, which represents a prismatic plane, is likely due to the higher electron transfer rate of the close-packed plane [96]. This preferential etching of the β-phase and close-packed orientations of the α-phase results in the formation of pores on the surface, as grains of specific orientations are removed. The pores are on the order of 1 μm in diameter. This has numerous implications for the treatment of titanium implants, with the potential to create rough surfaces that will prevent micromotion at the bone-metal interface and pores to encourage bone ingrowth into the implant surface. The SEM image in Figure 5.6 shows a similar morphology formed by the nitric acid-peroxide solution on the Ti6Al4V surface after 24 hours. Here again, the XRD patterns reveal the preferential etching of the basal and pyramidal planes over the more acid-resistant prismatic planes. The mixture of the nitric acid with the peroxide results in a much less volatile solution than sulfuric acid + hydrogen peroxide, which may be advantageous for future surface treatments of Ti6Al4V, as it would eliminate the need for the sulfuric acid-peroxide solution in order to obtain this morphology. The sulfuric acid treatment also resulted in more significant preferential etching of the vanadium rich β-phase, as evidenced by the XRD patterns and EDS data.

The differences in the behavior of the Fe30Mn versus the Ti6Al4V under treatment with acid and hydrogen peroxide solutions is a result both of the surface chemistry of the samples and the differences in their microstructures. It is unknown whether the Ti6Al4V was cold-worked and/or heat treated by the manufacturer. What is clear is that the grains of the Ti6Al4V were smaller and more uniform than the Fe30Mn. The Fe30Mn was used as-cast, with no further processing done on the samples. The chemical treatments on the Fe30Mn would almost certainly result in different morphologies had the alloy been processed prior to treatment.

5.4.2 Corrosion Behavior

The corrosion rate of the material can be calculated using the relation

$$\text{Corrosion Rate (mm/year)} = 3.27 \text{ X } 10^{3}\,\frac{i_{corr} \times EW}{D} \qquad \text{Equation 5-5}$$

where i_{corr} is the corrosion current density (A/cm^2), D is the sample standard density (g/cm^3), and EW is the equivalent weight based on the composition of the alloying elements. The corrosion current density can be approximated by performing a Tafel fit using EC-Lab software.

Treatment with the piranha solution increased the corrosion rate of the Ti6Al4V surfaces after 15 minutes and 24 hours of treatment. This could be due to a chemical change in the surface, coupled with the increased surface area created by the formation of the pores. However, the opposite was seen in the case of the nitric acid-hydrogen peroxide treatment, which exhibited a very similar morphology; after 1 hour and 24 hours, the corrosion rate of the Ti6Al4V decreased, in spite of the formation of the porous surface. The vanadium concentration decreased after treatment with sulfuric acid, which may contribute to the decreased corrosion resistance of the piranha treated surfaces, however the sample treated for 1 hour exhibited the lowest concentration of vanadium and the lowest corrosion rate of the sulfuric-acid treated samples. The phosphoric acid treatment had little effect on the Ti6Al4V corrosion rate after 15 minutes and 1 hour, however the corrosion rate of the sample treated for 24 hours was nearly double that of the control. The EDS showed very little compositional change between 1 hour and 24 hours. It is likely, therefore, that the increased corrosion rate is due to the increased surface area of the sample treated for 24 hours.

5.5 Conclusions

The advantages to chemical treatment as a means of surface modification of metal alloys are the relatively low expense and simplicity, as well as the short time-frames needed to alter the surface chemistry and morphology. The major disadvantages are the inherent dangers of the chemicals to the experimenter, and the generation of hazardous waste. These risks can be mitigated through proper safety protocols. If implants are treated with harsh chemicals, they must be thoroughly cleaned in order to remove all traces of the acids, or serious damage to local tissue could result.

While the phosphoric acid-hydrogen peroxide treatment was successful in creating a porous oxide layer on the surface of the Fe30Mn sample, this oxide layer was very flaky and unstable after 24 hours. The pores after 24 hours of treatment would be large enough for ingrowth of bone marrow stromal cells, however the sample was extremely delicate and would not be viable for implantation. The pores formed after 1 hour would not be large enough for cell ingrowth. Modification of the time of immersion or the chemical composition of the treatment might aid in the production of a stable porous oxide with phosphoric acid treatment. Treatment of the titanium samples with both the nitric acid solution and the sulfuric acid solution resulted in the formation of micron-scale pores on the surface after 24 hours. This is likely due to the preferential attack of the vanadium-rich bcc β-phase [52], and the more reactive basal and pyramidal orientations of the hcp α-phase of Ti6Al4V compared with the prismatic planes. In the case of the samples treated with sulfuric acid, this corresponded with a decrease in the corrosion resistance of the sample. The samples treated with nitric acid, on the other hand, showed no appreciable change in the corrosion rate, and the concentration of vanadium in the surface did not change within experimental uncertainty, while the concentration of vanadium in the sulfuric-acid treated samples decreased significantly.

As predicted, the treatment of the iron manganese samples with different acid-peroxide solutions resulted in the formation of various iron oxides and iron oxyhydroxides on their surfaces. These surface oxide layers, however, were very unstable, flaking off with even gentle handling. The sample treated with sulfuric acid appears to be covered in α-FeOOH, while the sample treated with nitric acid likely formed an amorphous Fe_2O_3 coating, and the sample treated with phosphoric acid is likely covered in FeO or Fe_3O_4.

CHAPTER 6 FINAL COMMENTS AND RECOMMENDATIONS FOR FUTURE WORK

6.1 Blood Compatibility of Resorbable Metals

The in vitro thrombogenicity assessment of the Fe35Mn showed relatively good blood compatibility compared with traditional 316L stainless steel, however there are many limitations to the *in vitro* model. Endothelialization, which typically takes place rapidly after insertion of an implant, does not take place in an *in vitro* model. *In vivo* tests are necessary in order to properly assess the full hemocompatibility of these materials. Further, these materials were only assessed for a short period of exposure. The *in vivo* studies should look at thrombogenic behavior over the lifetime of the implant in order to ensure continuing blood compatibility, especially during degradation of the materials. Due to the similarity of the vascular systems of humans and pigs, a porcine model would be an ideal preliminary test, with one or more Fe35Mn stents inserted into each animal in the test group, and with animals stented with traditional Nitinol or 316L stents as a control group. A sample of animals would be sacrificed at various time points, spanning from shortly after insertion to after complete degradation of the stent. This would also aid in assessing whether the radial strength of the stents is adequate to prevent early recoil of the vessel as it begins to degrade. The levels of iron and manganese in the animals' blood should be carefully monitored to ensure degradation does not lead to the build-up of toxic levels of metal ions. Post mortem examinations of the stented vessels will allow the surgeons to assess whether the stent caused appreciable tissue damage, restenosis, or thrombogenesis, and whether adequate endothelialization occurred after implantation.

6.2 Irradiation of Noble Metal Thin Films

Due to the initial rough nature of the deposited gold and palladium films on the surfaces of the silicon wafers, formation of nanoscale features through ion beam irradiation was not successful. In order to make this technique viable for creation of nanoscale features on the surfaces of inert biomaterials, a more reliable method for deposition of smooth films must be determined. The films were fabricated through electron beam deposition. Initially, the Si substrates were first coated in Ni in order to render them magnetic, and then capped with gold. This may have contributed to their overall roughness. After the nickel deposition was excluded, the films were still fairly rough. A more reliable technique is therefore necessary in order to create initially smooth gold surfaces.

During cell culture, the gold films delaminated from the Si substrate after immersion in cell culture media. It is therefore also necessary to ensure good adhesion of the gold films to the substrates prior to cell tests. An adhesion layer of chromium was employed, but chromium metal is cytotoxic and this adhesion layer proved inadequate in preventing delamination. Therefore, in order to make nanopatterned gold films a viable coating for bioactive stents, a reliable adhesion method must be found.

6.3 Irradiation of Silicon Wafers

Ion beam irradiation of Si(100) wafers with argon ions produced nanoscale features, including dots for near-normal incidence and ripples for oblique incidence. Based upon previous studies in the literature, it seems pattern formation on ultra-high purity silicon is not possible; the presence of a small concentration of metal impurities, such as iron, is necessary to produce patterns on pure silicon surfaces. The silicon used in this study had a sufficient concentration of metal impurities to induce pattern formation on the surface. This impurity-driven patterning is especially evident from the SEM images, where more regular, ordered structures are shown near adsorbed particles on the surfaces of the Si(100) wafers. Uniform patterning of silicon wafers is possible by deposition of an ultrathin thin film of gold prior to low-energy argon ion beam irradiation [97]. The gold mixes with the silicon at the surface during early bombardment and is eventually eliminated through preferential sputtering after fluences on the order of 4E17cm^{-2} [97]. This process has been shown to create islands of about 11-14nm in diameter [97]. Similarly, ultrathin films of Ni and Fe deposited on Si prior to irradiation also aid in the production of these nanoscale features, however complete smoothing of the samples were seen after elimination of all Cu deposited in a similar experiment [98].

6.4 Fe35Mn Irradiation

The ion beam irradiation of the Fe35Mn surfaces showed much promise in terms of nanostructure formation on the surface. Nanoscale features were created on the surfaces of FeMn irradiated with Ar^+ ions for energies between 500eV and 1keV. Further characterization of these surfaces with AFM is necessary in order to accurately determine the average size and three-dimensional shape of these features, as SEM is limited to two-dimensional information. A thorough analysis of the corrosion behavior of these irradiated materials is also necessary in order to determine whether the enrichment of iron at the surface will alter the early degradation rate of the alloy. It must also be determined whether the geometry of these features will contribute to localized corrosion, where the valleys between features may behave like crevices, leading to galvanic corrosion of the surface in these areas.

How these structures would affect cell behavior is still unknown. Cytotoxicity and cell metabolism studies with endothelial cells and bone marrow stromal cells are recommended in order to determine whether the structures will positively influence endothelialization, adhesion, and differentiation into osteoblasts. Previous work in our group has shown that bone marrow stromal cells adhere better to rougher surfaces induced by mechanical polishing and orient themselves along the direction of the grooves. It is necessary to perform similar studies with the irradiated surfaces in order to examine cell adhesion and morphology on these surfaces compared with both the ground surfaces and very smooth surfaces. The ions used in this study were inert Ar^+ ions. The influence of oxygen ions would be interesting to examine, as not only would the ions have the potential to alter the surface morphology and composition, they could also be used to form uniform oxides on the surface, in order to control the early degradation behavior of the implant.

6.5 Chemical Oxidation of FeMn and Ti6Al4V Surfaces

The chemical treatments showed some promise, especially with regard to the Ti6Al4V. Rough, porous surfaces were prepared using solutions of nitric acid-hydrogen peroxide and sulfuric acid-hydrogen peroxide. The chemistry and exposure times could be further tailored in order to develop specific surface characteristics. The iron manganese samples might have behaved differently after treatment if they initially had a more homogeneous microstructure; heat treatments and cold working processes might improve the microstructural characteristics, resulting in more uniform attack of the FeMn surfaces. While the phosphoric acid treatment was successful in inducing porosity on the surface of the FeMn alloy, the sample became extremely brittle after treatment and would not be a good candidate for implantation. This porosity also did not cover the entire surface of the sample. A more thorough study using more homogeneous samples, modified exposure times, and various chemical concentrations is necessary in order to produce pores of ideal size without compromising the mechanical integrity of the sample. A systematic study using varying concentrations of acid, different ratios of acid to peroxide, and multiple exposure times between 1 hour and 24 hours is recommended. The composition of the resultant surfaces can be determined using XRD, although it is recommended to use a Co source or a Cu source with a monochromator to eliminate fluorescence photons.

After chemical treatment with acid-peroxide solutions, the Ti6Al4V surfaces exhibited preferential etching of particular grain orientations, with the exception of phosphoric acid treatment. The phosphoric acid-hydrogen peroxide solution etched the grain boundaries only. The nitric acid and sulfuric acid treatments, on the other hand, etched away specific grain orientations. The basal and pyramidal orientations appear to have been etched more strongly than the prismatic orientations. This resulted in a porous surface on the Ti6Al4V. The porous surface created through nitric acid and peroxide treatment exhibited similar corrosion behavior to the as-manufactured sample, while the corrosion resistance decreased after sulfuric acid and peroxide treatment at the same time point. Previous work by Variola et al. showed that porous surfaces created through controlled chemical oxidation with H_2O_2 and H_2SO_4 inhibited fibroblast growth and stimulated osteoblast proliferation [52]. It is unclear whether the nitric acid-treated surface would have a similar effect on osteoblast growth, although it is likely given the similarity of their morphologies. Further, these surfaces may have an impact on the differentiation of bone-progenitor cells, although this has not yet been explored. A thorough study on bone marrow stromal cell growth, adhesion, and mineralization on the porous surfaces created through controlled chemical oxidation compared with ground and smooth-polished Ti6Al4V surfaces is recommended to determine the utility of these chemical treatments. This can be examined through fluorescence microscopy, using cytoskeletal, nucleic, and actin dyes and through scanning electron microscopy in order to compare cell coverage and mineralization.

LIST OF REFERENCES

LIST OF REFERENCES

[1] B. D. Ratner, A. S. Hoffman, F. J. Schoen, and J. E. Lemons, *Biomaterials Science: An Introduction to Materials in Medicine* vol. 3rd. Kidlington, Oxford, UK: Elsevier, 2012.

[2] T. Sridhar and S. Rajeswari, "Biomaterials Corrosion," *Corrosion Reviews,* pp. 287-332, 2009.

[3] L. L. Hench and J. M. Polak, "Third-Generation Biomedical Materials," *Science,* vol. 295, pp. 1014-1017, February 8, 2002 2002.

[4] T. Kokubo, "Bioactive glass ceramics: properties and applications," *Biomaterials* vol. 12, pp. 155-163, 1991.

[5] M. Navarro, A. Michiardi, O. Castano, and J. A. Planell, "Biomaterials in orthopaedics," *J R Soc Interface,* vol. 5, pp. 1137-58, Oct 6 2008.

[6] D. F. Williams, "On the mechanisms of biocompatibility," *Biomaterials,* vol. 29, pp. 2941-53, Jul 2008.

[7] R. Waksman and R. Pakala, "Biodegradable and Bioabsorbable Stents," *Current Pharmaceutical Design,* vol. 16, pp. 4041-4051, December 2010 2010.

[8] J. Ansell, J. Hirsh, E. Hylek, A. Jacobson, M. Crowther, G. Palareti*, et al.*, "Pharmacology and management of the vitamin K antagonists: American College of Chest Physicians Evidence-Based Clinical Practice Guidelines (8th Edition)," *Chest,* vol. 133, pp. 160S-198S, Jun 2008.

[9] J. Hong, A. Azens, K. N. Ekdahl, C. G. Granqvist, and B. Nilsson, "Material-specific thrombin generation following contact between metal surfaces and whole blood," *Biomaterials,* vol. 26, pp. 1397-403, Apr 2005.

[10] D. Stoeckel, A. Pelton, and T. Duerig, "Self-expanding nitinol stents: material and design considerations," *Eur Radiol,* vol. 14, pp. 292-301, Feb 2004.

[11] T. Duerig, A. Pelton, and D. Stoeckel, "An overview of nitinol medical applications," *Materials Science and Engineering: A,* vol. 273-275, pp. 149-160, 1999.

[12] W. D. Callister and D. G. Rethwisch, *Materials Science and Engineering: An Introduction*, 8th ed. United States of America: Wiley, 2010.

[13] R. J. Narayan, "The next generation of biomaterial development," *Philos Trans A Math Phys Eng Sci,* vol. 368, pp. 1831-7, Apr 28 2010.

[14] J. Y. Wong and J. D. Bronzion, *Biomaterials*. Boca Raton, FL: Taylor and Francis, 2007.

[15] R. Waksman, "Update on bioabsorbable stents: from bench to clinical," *Journal of Interventional Cardiology,* vol. 19, pp. 414-421, 2006.

[16] P. Peeters, M. Bosiers, J. Verbist, K. Deloose, and B. Hueblein, "Preliminary Results after Application of Absorbable Metal Stents in Patients With Critical Limb Ischemia," *Journal of Endovascular Therapy,* vol. 12, pp. 1-5, 2005.

[17] D. Schranz, P. Zartner, I. Michel-Behnke, and H. Akinturk, "Bioabsorbable metal stents for percutaneous treatment of critical recoarctation of the aorta in a newborn," *Catheter Cardiovasc Interv,* vol. 67, pp. 671-3, May 2006.

[18] J. A. Ormiston and P. W. S. Serruys, "Bioabsorbable coronary stents," *Circulation: Cardiovascular Interventions,* vol. 2, pp. 255-260, 2009.

[19] B. Heublein, R. Rhode, V. Kaese, M. Niemeyer, W. Hartung, and A. Haverich, "Biocorrosion of magnesium alloys: a new principle in cardiovascular implant technology?," *Heart,* vol. 89, pp. 651-656, 2003.

[20] R. Waksman, "Early- and long-term intravascular ultrasound and angiographic findings after bioabsorbable magnesium stent implantation in human coronary arteries " *JACC Cardiovascular Invervention,* vol. 2, pp. 312-320, 2009.

[21] P. Zartner, R. Cesnjevar, H. Singer, and M. Weyand, "First successful implantation of a biodegradable metal stent into the left pulmonary artery of a preterm baby," *Catheter Cardiovasc Interv,* vol. 66, pp. 590-4, Dec 2005.

[22] P. Zartner, M. Buettner, H. Singer, and M. Sigler, "First biodegradable metal stent in a child with congenital heart disease: evaluation of macro and histopathology," *Catheter Cardiovasc Interv,* vol. 69, pp. 443-446, 2005.

[23] R. Zeng, W. Dietzel, F. Witte, N. Hort, and C. Blawert, "Progress and Challenge for Magnesium Alloys as Biomaterials," *Advanced Engineering Materials,* vol. 10, pp. B3-B14, 2008.

[24] M. Peuster, P. Wohlsein, M. Brugmann, M. Ehlerding, K. Seidler, C. Fink*, et al.*, "A novel approach to temporary stenting: Degradable cardiovascular stents produced from corrodible metal--results 6-18 months after implantation into New Zealand white rabbits," *Heart,* vol. 86, pp. 563-569, 2001.

[25] H. Griffiths, P. Peeters, J. Verbist, M. Bosiers, K. Deloose, B. Heublein*, et al.*, "Future devices: bioabsorbable stents," *British Journal of Cardiology: Acute Interventional Cardiology,* vol. 11, pp. AIC 80- AIC-84, 2004.

[26] H. Hermawan, H. Alamdari, D. Mantovani, and D. Dubé, "Iron–manganese: new class of metallic degradable biomaterials prepared by powder metallurgy," *Powder Metallurgy,* vol. 51, pp. 38-45, 2008.

[27] P. K. Bowen, J. Drelich, and J. Goldman, "Zinc exhibits ideal physiological corrosion behavior for bioabsorbable stents," *Adv Mater,* vol. 25, pp. 2577-82, May 14 2013.

[28] B. Hennig, M. Toborek, and C. McClain, "Antiatherogenic properties of zinc: implications in endothelial cell metabolism," *Nutrition,* vol. 12, pp. 711-717, 1996.

[29] M. Ren, R. Rajendran, P. Ning, B. Tan Kwong Huat, O. Choon Nam, F. Watt*, et al.*, "Zinc supplementation decreases the development of atherosclerosis in rabbits," *Free Radic Biol Med,* vol. 41, pp. 222-5, Jul 15 2006.

[30] M. Berger, E. Rubinraut, I. Barshack, A. Roth, G. Keren, and J. George, "Zinc reduces intimal hyperplasia in the rat carotid injury model," *Atherosclerosis,* vol. 175, pp. 229-34, Aug 2004.

[31] H. Hermawan, A. Purnama, D. Dube, J. Couet, and D. Mantovani, "Fe-Mn alloys for metallic biodegradable stents: degradation and cell viability studies," *Acta Biomater,* vol. 6, pp. 1852-60, May 2010.

[32] J. E. Schaffer, E. A. Nauman, and L. A. Stanciu, "Cold-Drawn Bioabsorbable Ferrous and Ferrous Composite Wires: An Evaluation of Mechanical Strength and Fatigue Durability," *Metallurgical and Materials Transactions B,* vol. 43, pp. 984-994, 2012.

[33] A. Drynda, T. Hassel, F. W. Bach, and M. Peuster, "In vitro and in vivo corrosion properties of new iron-manganese alloys designed for cardiovascular applications," *J Biomed Mater Res B Appl Biomater,* Jun 28 2014.

[34] J. E. Schaffer, E. A. Nauman, and L. A. Stanciu, "Cold drawn bioabsorbable ferrous and ferrous composite wires: an evaluation of in vitro vascular cytocompatibility," *Acta Biomater,* vol. 9, pp. 8574-84, Nov 2013.

[35] N. Yahyapour, C. Eriksson, P. Malmberg, and H. Nygren, "Thrombin, kallikrein and complement C5b-9 adsorption on hydrophilic and hydrophobic titanium and glass after short time exposure to whole blood," *Biomaterials,* vol. 25, pp. 3171-6, Jul 2004.

[36] M. J. Dalby, N. Gadegaard, R. Tare, A. Andar, M. O. Riehle, P. Herzyk*, et al.*, "The control of human mesenchymal cell differentiation using nanoscale symmetry and disorder," *Nat Mater,* vol. 6, pp. 997-1003, Dec 2007.

[37] J. Lee, K. Lee, K. Sun, and Y. Park, "Morphological changes of human mesenchymal stem cells on a large area of nanopatterned surface," *Biomaterials Research,* vol. 17, pp. 1-6, 2013.

[38] R. G. Harrison, "On the stereotropism of embryonic cells," *Science,* pp. 279-281, 1911.

[39] A. S. G. Curtis, N. Gadegaard, M. J. Dalby, M. O. Riehle, C. D. Wilkinson, and G. Aitchinson, "Cells react to nanoscale order and symmetry in their surroundings," *IEEE Transactions on Nanobioscience* vol. 3, pp. 61-65, 2004.

[40] R. McMurray, M. J. Dalby, and N. Gadegaard, "Nanopatterned surfaces for biomedical applications," *INTECH Open Access Publisher,* 2011.

[41] J. M. Schmehl, C. Harder, H. P. Wendel, C. D. Claussen, and G. Tepe, "Silicon carbide coating of nitinol stents to increase antithrombogenic properties and reduce nickel release," *Cardiovasc Revasc Med,* vol. 9, pp. 255-62, Oct-Dec 2008.

[42] G. Tepe, J. Schmehl, H. P. Wendel, S. Schaffner, S. Heller, M. Gianotti*, et al.*, "Reduced thrombogenicity of nitinol stents--in vitro evaluation of different surface modifications and coatings," *Biomaterials,* vol. 27, pp. 643-50, Feb 2006.

[43] G. Tepe, H. P. Wendel, S. Khorchidi, J. Schmehl, J. Wiskirchen, B. Pusich*, et al.*, "Thrombogenicity of various endovascular stent types: an in vitro evaluation," *Journal of Vascular and Interventional Radiology,* vol. 13, pp. 1029-1035, 2002.

[44] K. Christensen, R. Larsson, H. Emanuelsson, G. Elgue, and A. Larsson, "Heparin coating of the stent graft--effects on platelets, coagulation and complement activation," *Biomaterials,* vol. 22, 2001.

[45] M. Castro, R. Cuerno, L. Vázquez, and R. Gago, "Self-Organized Ordering of Nanostructures Produced by Ion-Beam Sputtering," *Physical Review Letters,* vol. 94, 2005.

[46] J. Munoz-Garcia, L. Vasquez, R. Cuerno, J. A. Sanchez-Garcia, M. Castro, and R. Gago, "Self-Organized Surface Nanopatterning by Ion Beam Sputtering," *Nanoscale Science and Technology,* pp. 323-398, 2009.

[47] S. Habenict, W. Bolse, and K. P. Lieb, "Nanometer ripple formation and self-affine roughening of ion-beam-eroded graphite surfaces," *Physical Review B,* vol. 60, pp. R2200-R2203, 1999.

[48] K. H. Heinig, T. Muller, B. Schmidt, M. Strobel, and W. Muller, "Interfaces under ion irradiation: growth and taming of nanostructures," *Applied Physics A: Materials Science & Processing,* vol. 77, pp. 17-25, 2003.

[49] J. A. Sanchez-Garcia, L. Vazquez, R. Gago, A. Redondo-Cubero, J. M. Albella, and Z. Czigany, "Tuning the surface morphology in self-organized ion beam nanopatterning of Si(001) via metal incorporation: from holes to dots," *Nanotechnology,* vol. 19, p. 355306, Sep 3 2008.

[50] M. Aziz, "Nanoscale Morphology Control Using Ion Beams," *On Beam Science: Solved and Unsolved Problems: Invited Lectures Presented at a Symposium Arranged by the Royal Danish Academy of Science and Letters,* pp. 187-206, 2006.

[51] M. Heiden, E. Walker, E. Nauman, and L. Stanciu, "Evolution of novel bioresorbable iron-manganese implant surfaces and their degradation behaviors in vitro," *J Biomed Mater Res A,* vol. 103, pp. 185-93, Jan 2015.

[52] F. Variola, J. H. Yi, L. Richert, J. D. Wuest, F. Rosei, and A. Nanci, "Tailoring the surface properties of Ti6Al4V by controlled chemical oxidation," *Biomaterials,* vol. 29, pp. 1285-98, Apr 2008.

[53] K. Kieswetter, Z. Schwartz, D. D. Dean, and B. D. Boyan, "The role of implant surface characteristics in the healing of bone," *Crit Rev Oral Biol Med,* vol. 7, pp. 329-345, 1996.

[54] Y. Onuma and P. W. Serruys, "Bioresorbable scaffold: the advent of a new era in percutaneous coronary and peripheral revascularization?," *Circulation,* vol. 123, pp. 779-97, Feb 22 2011.

[55] P. Erne, M. Schier, and T. J. Resink, "The road to bioabsorbable stents: reaching clinical reality?," *Cardiovasc Intervent Radiol,* vol. 29, pp. 11-6, Jan-Feb 2006.

[56] B. Thierry, Y. Merhi, L. Bilodeau, C. Trepanier, and T. Tabrizian, "Nitinol versus stainless steel stents: acute thrombogenicity study in an ex vivo porcine model," *Biomaterials,* vol. 23, pp. 2997-3005, 2002.

[57] B. D. Ratner, "The catastrophe revisited: blood compatibility in the 21st Century," *Biomaterials,* vol. 28, pp. 5144-7, Dec 2007.

[58] K. Kolandaivelu, R. Swaminathan, W. J. Gibson, V. B. Kolachalama, K. L. Nguyen-Ehrenreich, V. L. Giddings*, et al.*, "Stent thrombogenicity early in high-risk interventional settings is driven by stent design and deployment and protected by polymer-drug coatings," *Circulation,* vol. 123, pp. 1400-9, Apr 5 2011.

[59] M. E. Kelly, A. J. Furlan, and D. Fiorella, "Recanalization of an acute middle cerebral artery occlusion using a self-expanding, reconstrainable, intracranial microstent as a temporary endovascular bypass," *Stroke,* vol. 39, pp. 1770-3, Jun 2008.

[60] J. P. Allain, T. Tigno, and R. A. Armonda, "Nanotechnology in support of novel neuroendovascular strategy," in *The Textbook of Nanoneuroscience and Nanoneurosurgery*, ed Boca Raton, FL: CRC Press, Taylor and Francis Group, 2004.

[61] R. Bonan and A. W. Asgar, "Biodegradable stents--where are we in 2009?," *Interventional Cardiology,* pp. 81-84, 2009.

[62] H. Hermawan, D. Dube, and D. Mantovani, "Developments in metallic biodegradable stents," *Acta Biomater,* vol. 6, pp. 1693-7, May 2010.

[63] N. Duraiswamy, J. Cesar, R. Shoephoerster, and J. Moore Jr., "Effects of stent geometry on local flow dynamics and resulting platelet deposition in an in vitro model," *Biorheology,* vol. 45, pp. 547-561, 2008.

[64] H. Hermawan, D. Dube, and D. Mantovani, "Degradable metallic biomaterials: design and development of Fe-Mn alloys for stents," *J Biomed Mater Res A,* vol. 93, pp. 1-11, Apr 2010.

[65] J. Crossgrove and W. Zheng, "Manganese toxicity upon overexposure," *NMR Biomed,* vol. 17, pp. 544-553, 2004.

[66] S. Sinn, T. Scheuermann, S. Deichelbohrer, G. Ziemer, and H. P. Wendel, "A novel in vitro model for preclinical testing of the hemocompatibility of intravascular stents according to ISO 10993-4," *J Mater Sci Mater Med,* vol. 22, pp. 1521-8, Jun 2011.

[67] K. K. Wu, "Platelet activation mechanisms and markers in arterial thrombosis," *Journal of Internal Medicine,* vol. 239, pp. 17-34, 1996.

[68] H. Nygren, C. Eriksson, and J. Lausmaa, "Adhesion and activation of platelets and polymorphonuclear granluocytes cells at TiO2 surfaces," *J Lab Clin Med,* pp. 35-46, 1997.

[69] R. S. Bell, R. D. Ecker, M. A. Severson, 3rd, J. E. Wanebo, B. Crandall, and R. A. Armonda, "The evolution of the treatment of traumatic cerebrovascular injury during wartime," *Neurosurg Focus,* vol. 28, p. E5, May 2010.

[70] M. Navez, D. Chaperot, and C. Sella, "Microscopie electronique-etude de l'attaque du verre par bombardement ionique," *Comptes Rendus Hebdomadaires Des Seances de L'Acadmie Des Sciences,* vol. 254, p. 240, 1962.

[71] R. E. McMahon, J. Ma, S. V. Verkhoturov, D. Munoz-Pinto, I. Karaman, F. Rubitschek*, et al.*, "A comparative study of the cytotoxicity and corrosion resistance of nickel-titanium and titanium-niobium shape memory alloys," *Acta Biomater,* vol. 8, pp. 2863-70, Jul 2012.

[72] F. Frost, B. Ziberi, A. Schindler, and B. Rauschenbach, "Surface engineering with ion beams: from self-organized nanostructures to ultra-smooth surfaces," *Applied Physics A,* vol. 91, pp. 551-559, 2008.

[73] P. Sigmund, "A mechanism of surface micro-roughening by ion bombardment," *Journal of Materials Science* vol. 8, pp. 1545-1553, 1973.

[74] P. Sigmund, "Mechnisms and theory of physical sputtering by particle impact," *Nuclear Instruments and Methods in Physics Research B,* vol. 27, pp. 1-20, 1987.

[75] R. M. Bradley, "Theory of ripple topography induced by ion bombardment," *Journal of Vacuum Science & Technology A: Vacuum, Surfaces, and Films,* vol. 6, p. 2390, 1988.

[76] L. T. Canham, "Bioactive Silicon Structure Fabrication Through Nanoetching Techniques," *Advanced Materials,* vol. 7, pp. 1033-1037, 1995.

[77] G. Ozaydin, K. F. Ludwig, H. Zhou, L. Zhou, and R. L. Headrick, "Transition behavior of surface morphology evolution of Si(100) during low-energy normal-incidence Ar[sup +] ion bombardment," *Journal of Applied Physics,* vol. 103, p. 033512, 2008.

[78] C. P. Bergmann and A. Stumpf, "Biomaterials," in *Dental Ceramics*, ed, 2013, pp. 9-13.

[79] G. Carter and V. Vishnyakov, "Roughening and Ripple Instabilities on Ion-Bombarded Si," *Physical Review B,* vol. 54, pp. 17647-17653, 1996.

[80] B. Ziberi, F. Frost, T. Höche, and B. Rauschenbach, "Ripple pattern formation on silicon surfaces by low-energy ion-beam erosion: Experiment and theory," *Physical Review B,* vol. 72, 2005.

[81] S. Macko, F. Frost, B. Ziberi, D. F. Forster, and T. Michely, "Is keV ion-induced pattern formation on Si(001) caused by metal impurities?," *Nanotechnology,* vol. 21, p. 85301, Feb 26 2010.

[82] R. Kelly, "An attempt to understand preferential sputtering," *Nuclear Instruments and Methods,* vol. 149, pp. 553-558, 1978.

[83] G. S. Was, "Ion beam modification of metals: compositional and microstructural changes," *Progress in Surface Science,* vol. 32, pp. 211-332, 1990.

[84] P. Sigmund, "Mechanisms and theory of physical sputtering by particle impact," *Nuclear Instruments and Methods in Physics Research Section B: Beam Interactions with Materials and Atoms,* 1987.

[85] M. Wahlgren, S. Welin-Klintstrom, T. Arnebrant, A. Askendal, and H. Elwing, "Competition between fibrinogen and a non-ionic surfactant in adsorption to a wettability gradient surface," *Colloids and Surfaces B: Biointerfaces,* vol. 4, pp. 23-31, 1995.

[86] S. Welin-Klintstrom, A. Askendal, and H. Elwing, "Surfactant and Protein Interactions on Wettability Gradient Surfaces," *Journal of Colloid and Interface Science,* vol. 158, pp. 188-194, 1993.

[87] H. Elwing, S. Welin, A. Askendal, U. Nilsson, and I. Lundstrom, "A wettability gradient method for studies of macromolecular interactions at the liquid/solid interface," *Journal of Colloid and Interface Science,* vol. 119, pp. 203-210, 1987.

[88] Y. Arima and H. Iwata, "Effect of wettability and surface functional groups on protein adsorption and cell adhesion using well-defined mixed self-assembled monolayers," *Biomaterials,* vol. 28, pp. 3074-82, Jul 2007.

[89] M. Sivakumar and S. Rajeswari, "Investigation of failures in stainless steel orthopaedic implant devices: pit-induced stress corrosion cracking," *Journal of Materials Science Letters,* vol. 11, pp. 1039-1042, 1992.

[90] I. L. Rosenfeld and I. S. Danilov, "Electrochemical Aspects of Pitting Corrosion," *Corrosion Science,* vol. 7, pp. 129-142, 1967.

[91] G. S. Frankel, "Pitting Corrosion of Metals: A Review of the Critical Factors," *Journal of the Electrochemical Society,* vol. 145, pp. 2186-2198, 1998.

[92] T. Kokubo and H. Takadama, "How useful is SBF in predicting in vivo bone bioactivity?," *Biomaterials,* vol. 27, pp. 2907-15, May 2006.

[93] M. Ilbert and V. Bonnefoy, "Insight into the evolution of the iron oxidation pathways," *Biochim Biophys Acta,* vol. 1827, pp. 161-75, Feb 2013.

[94] S. L. R. da Silva, L. O. Kerber, L. Amaral, and C. A. dos Santos, "X-ray diffraction measurements of plasma nitrided Ti-6Al-4V," *Surface and Coatings Technology,* vol. 116-119, pp. 342-346, 1999.

[95] J. G. Webster, P. J. Swedlund, and K. S. Webster, "Trace metal adsorption onto an acid mine drainage iron(III) oxy hydroxy sulfate," *Environmental Science & Technology,* vol. 32, pp. 1361-1368, 1998.

[96] B. Davepon, J. W. Schultze, U. König, and C. Rosenkranz, "Crystallographic orientation of single grains of polycrystalline titanium and their influence on electrochemical processes," *Surface and Coatings Technology,* vol. 169-170, pp. 85-90, 2003.

[97] O. El-Atwani, S. Ortoleva, A. Cimaroli, and J. P. Allain, "Formation of silicon nanodots via ion beam sputtering of ultrathin gold thin film coatings on Si," *Nanoscale Research Letters,* vol. 6, 2011.

[98] O. El-Atwani, S. Gonderman, A. DeMasi, A. Suslova, J. Fowler, M. El-Atwani*, et al.*, "Nanopatterning of metal-coated silicon surfaces via ion beam irradiation: Real time x-ray studies reveal the effect of silicide bonding," *Journal of Applied Physics,* vol. 113, p. 124305, 2013.

VITA

VITA

Emily Walker was born in 1988 in Madison, Wisconsin. She attended high school in White Bear Lake, Minnesota and performed research at the University of Minnesota in the Department of Physics on a NASA-funded project during her senior year. She attended Rose-Hulman Institute of Technology in Terre Haute, Indiana from 2006 to 2010, where she earned a B.S. in physics with a minor in optical engineering. As an undergraduate, Emily conducted research at Rose-Hulman on a DARPA-sponsored project, and at Kansas State University through the NSF's summer REU program. After graduating with her bachelor's degree, she attended Purdue University in West Lafayette, Indiana where she conducted her PhD research in materials engineering. During the summer of 2014, Emily served as a graduate assistant to the Summer Undergraduate Research Fellowship (SURF) program. Emily began a graduate internship at Los Alamos National Laboratory in October, 2014 and plans to join the Laboratory after graduation.